Cell Systems

Article

Maternal smoking in early pregnancy disrupts placental function through syncytiotrophoblast and macrophage dysregulation

Highlights

- Multi-omic profiling reveals early placental dysregulation from maternal smoking
- Syncytiotrophoblast and Hofbauer macrophages are most affected by maternal smoking
- Smoking drives barrier mitochondrial accumulation and impairs placental cell communication

Authors

Daniela S. Valdes, Jose Nimo, Olivia Nonn, ..., Martin Gauster, Fabian Coscia, Florian Herse

Correspondence

fabian.coscia@mdc-berlin.de (F.C.), florian.herse@charite.de (F.H.)

In brief

Maternal smoking impairs placental function and is linked to fetal growth restriction, yet its cell-specific effects in early pregnancy have remained unclear. Valdes et al. use single-nucleus transcriptomics and spatial proteomics of first-trimester human placenta to show that smoking mostly disrupts syncytiotrophoblasts and Hofbauer macrophages, thereby altering trophoblast differentiation, mitochondrial content, and hemostasis at the maternal-fetal interface.

Valdes et al., 2026, Cell Systems *17*, 101785
December 16, 2026 © 2026 The Author(s). Published by Elsevier Inc.
https://doi.org/10.1016/j.cels.2026.101785

CellPress

Please cite this article in press as: Valdes et al., Maternal smoking in early pregnancy disrupts placental function through syncytiotrophoblast and macrophage dysregulation, Cell Systems (2026), https://doi.org/10.1016/j.cels.2026.101785

Cell Systems

CellPress
OPEN ACCESS

Article

Maternal smoking in early pregnancy disrupts placental function through syncytiotrophoblast and macrophage dysregulation

Daniela S. Valdes,[1,3,4,5,13] Jose Nimo,[2,4] Olivia Nonn,[1,3,4,5,6] Juliane Ulrich,[1,3,4] Désirée Forstner,[7] Sandra Haider,[8] Miriam Ressler,[9] Marc Pignitter,[10] Barbara Obermayer-Pietsch,[11] Dominik N. Müller,[1,3,4,5] Ralf Dechend,[1,3,4,5,12] Martin Gauster,[7] Fabian Coscia,[2,*] and Florian Herse[1,3,4,5,14,*]

[1]Max-Delbrück-Center for Molecular Medicine in the Helmholtz Association (MDC), Hypertension-Mediated End Organ Damage Group, Berlin, Germany
[2]Max-Delbrück-Center for Molecular Medicine in the Helmholtz Association (MDC), Spatial Proteomics Group, Berlin, Germany
[3]Experimental and Clinical Research Center, Max-Delbrück-Center for Molecular Medicine in the Helmholtz Association and Charité – Universitätsmedizin Berlin, Berlin, Germany
[4]Charité – Universitätsmedizin Berlin, Freie Universität Berlin and Humboldt-Universität zu Berlin, Berlin, Germany
[5]DZHK (German Center for Cardiovascular Research), Partner Site Berlin, Berlin, Germany
[6]Berlin Institute of Health at Charité – Universitätsmedizin Berlin, BIH Biomedical Innovation Academy, BIH Charité Junior Clinician Scientist Program, Charitéplatz 1, 10117 Berlin, Germany
[7]Division of Cell Biology, Histology and Embryology, Gottfried Schatz Research Center, Medical University of Graz, Graz, Austria
[8]Department of Obstetrics and Gynaecology, Reproductive Biology Unit, Medical University of Vienna, Vienna, Austria
[9]Institute of Biomedical Science, Department of Health Studies, FH Joanneum University of Applied Sciences, Graz, Austria
[10]Department of Physiological Chemistry, Faculty of Chemistry, University of Vienna, 1090 Vienna, Austria
[11]Department of Internal Medicine, Division of Endocrinology and Diabetology and Department of Obstetrics and Gynaecology, Endocrinology Lab Platform, Medical University of Graz, Graz, Austria
[12]HELIOS Clinic, Department of Cardiology and Nephrology, Berlin, Germany
[13]Freie Universität Berlin, Berlin, Germany
[14]Lead contact
*Correspondence: fabian.coscia@mdc-berlin.de (F.C.), florian.herse@charite.de (F.H.)
https://doi.org/10.1016/j.cels.2026.101785

SUMMARY

Smoking in pregnancy is a leading avoidable cause of adverse pregnancy and perinatal outcomes that is causally linked to fetal growth restriction (FGR), partly through impaired placental function. The placenta, the functional interface between mother and fetus, is essential for fetal development. We studied cell type-resolved smoking effects on human placental development using single-nucleus RNA sequencing and deep visual proteomics of matched tissues, validated in an independent cohort and *in vitro* cigarette smoke exposure to primary human trophoblast cells. The syncytiotrophoblast (STB) barrier and Hofbauer cells (placental macrophages) are most affected, with dysregulated cell-cell adhesion, extracellular matrix organization, and stress phenotypes. The trophoblast shows *in silico* preferential differentiation toward the STB, upregulated pro-angiogenic effectors, increased xenobiotic detoxification, reduced mitochondrial function, and altered transmembrane transport, all of which contribute to abnormal placental development. We provide insight into placental dysfunction linked to pregnancy complications early in pregnancy in order to inform diagnostics and therapies for fetal and maternal health.
A record of this paper's transparent peer review process is included in the supplemental information.

INTRODUCTION

The placenta constitutes the interface between mother and fetus. It modulates maternal metabolism in pregnancy by regulating nutrient, metabolite, and gas exchange and has endocrine activity in maternal blood.[1] Healthy development and function of the placenta are essential for a successful pregnancy and fetal health. Developmental abnormalities modulate various disorders of pregnancy with lifelong consequences such as cardiovascular disease.[2,3]

Placental development occurs primarily in the first half of pregnancy. The most abundant cell type in the placenta is trophoblast cells. Mononucleated cytotrophoblasts (CTBs) form tree-like villi structures covered by a multinuclear syncytiotrophoblast (STB) layer.[4] The transcriptionally active STB establishes the functional interface between maternal blood and placental villi. Due to its

This is an open access article under the CC BY license (http://creativecommons.org/licenses/by/4.0/).
Open access funding enabled and organized by Projekt DEAL.

Please cite this article in press as: Valdes et al., Maternal smoking in early pregnancy disrupts placental function through syncytiotrophoblast and macrophage dysregulation, Cell Systems (2026), https://doi.org/10.1016/j.cels.2026.101785

direct contact with maternal blood, the STB is involved in most functions of the placenta, as reflected by its high metabolic rate of up to 40% of the total feto-placental oxygen consumption.[5] Placental-derived circulating factors are primarily secreted by the STB syncytium and have profound effects both on placental development and on maternal physiology.[6] Placental growth factor (PlGF), a member of the vascular endothelial growth factor (VEGF) family, is an important pro-angiogenic marker, and its imbalance is closely linked to hypertension in pregnancy.[7] In early pregnancy, it plays critical roles in placental development, in the context of vasculogenesis, angiogenesis, and trophoblast lineage development.[8]

Adequate fetal development and growth are limited by the rate at which the placenta can deliver nutrients, oxygen, and remove waste. Placental dysfunction has been associated with the pathophysiology of fetal growth restriction (FGR), preterm labor, preeclampsia (PE), and miscarriage.[9,10] FGR is a leading cause of fetal morbidity and mortality worldwide,[11] which arises as a result of inadequate nutrient or oxygen supply at the maternal-fetal interface. Suboptimal fetal development, due to nutrient or oxygen deprivation, placental insufficiency, or exposure to toxic substances, is a contributing factor for cardiovascular disease.[12] Detrimental effects extend well beyond pregnancy and affect the lifelong health of both mother and offspring related to cardiovascular and metabolic disorders.[3,13]

Maternal smoking in pregnancy has a self-reported global prevalence of 1.7%, with a much higher European region estimate of 8.1%.[14] Of note, self-reporting underestimates true smoking status by up to 25% in Europe.[15] Smoking during pregnancy is associated with various pregnancy complications including placental abruption, placenta previa, ectopic pregnancy, preterm birth, FGR, and low birthweight. FGR and low birthweight are causally linked to maternal smoking.[16,17] Fetal birth defects in multiple organ systems are positively associated with maternal smoking.[18] At term, morphological effects of maternal smoking are well characterized. These include an altered placental weight[19,20]; increased calcifications and stiffened matrix,[21] reduced volume of intervillous space,[22] and a profound adaptive angiogenesis in placental blood vessels.[23,24] Functional effects encompass altered amino acid and glucose transport,[25] progesterone synthesis,[26] and estrogen metabolism.[27]

The placenta suffers oxidative stress and damage after sustained exposure to toxic smoke components in the circulation of maternal smokers. Reactive oxygen species (ROS) are associated with increased lipid peroxidation in the placenta later in pregnancy, with effects on cell membrane integrity and transport function. Gene expression of *CYP1A1* and *CYP1B1,* phase I xenobiotic metabolizing enzymes of the cytochrome P450 system, is sharply upregulated in placentas from maternal smokers at term,[28,29] contributing to intracellular ROS formation. These are downstream of the activation of the aryl hydrocarbon receptor (AhR) pathway, well known for its modulation of the xenobiotic response.[30]

Maternal smoking in pregnancy is deleterious for placental health in every trimester of pregnancy. Reports have largely focused on global tissue dysregulation in the third trimester with limited cell phenotype specificity. However, we currently lack a detailed understanding of the transcriptional and proteomic consequences of maternal smoking in first-trimester placental tissue. Herein, we profiled the transcriptomic and proteomic landscape of the early human placenta. We characterize the profound impact of smoking at the single-phenotype level during the developing phase of the placenta. We describe molecular origins of aberrant interface capacity that mechanistically underpin abnormal placental development and function, likely leading to adverse obstetric outcomes in pregnancy.

RESULTS

Maternal smoking effects in early pregnancy are driven by placental barrier and immune capacity dysregulation

To understand phenotype-specific molecular effects of maternal smoking on the developing human placenta, we analyzed first trimester tissues from elective terminations (5–11 weeks of gestation) (Figure 1A; Table S1). We applied 10× Genomics single-nucleus RNA sequencing (snRNA-seq) to high-quality nuclei isolated from 11 placentas (n = 5 smokers and n = 6 non-smokers) and conducted spatially resolved deep visual proteomics (DVP)[31] of formalin-fixed paraffin-embedded (FFPE) villi from a subset of the same tissues (n = 3 smokers and n = 3 non-smokers). These methods allowed for the unique and extensive molecular profiling of the STB, seldom performed since this syncytium is impossible to derive into a single-cell suspension. Samples were matched for gestational age, maternal age, and maternal body mass index (BMI) (Figure S1; STAR Methods). In addition, we validated findings in an independent cohort (n = 23 smokers and n = 15 non-smokers) and through *in vitro* functional assays using primary derived human trophoblast stem cells (TSCs).

Maternal smoking status was stratified by concordance between self-reporting and circulating cotinine levels, a stable metabolite from nicotine and clinical gold standard for assessing smoking status.[32] In the cohort used for snRNA-seq and DVP techniques, cotinine cut-offs of >50 ng/mL (heavy smokers, range 88–183 ng/mL) and <1 ng/mL (non-smokers) were used to stratify samples, to capture effects of heavy smoking. For the independent validation cohort, cotinine cut-offs of >9 ng/mL (smokers, range 9–536 ng/mL) and <1 ng/mL (non-smokers) were used to include moderate-to-heavy smokers and test whether core findings generalize to the broader smoking population (Figure S1). After ambient RNA correction, doublet detection, and stringent quality-control filtering, we retained 88,808 high-quality nuclei (n = 38,756 smokers and n = 50,052 non-smokers) for subsequent analyses (STAR Methods). Sample normalization, batch correction, and integration methods were applied to gain a harmonized dataset unconfounded by technical or biological sources of variance (Figure S1).

Nine highly specific cellular phenotypes encompassing three functional cellular states were resolved and annotated using a combination of canonical marker specificity, differential, and conserved gene expression between communities (Figures 1B and 1C; STAR Methods). Six describe the trophoblast lineage: the cytotrophoblast (CTB), its proliferating (CTBp) and pre-fusion (CTBpf) states; the STB and its recently described immature state (STBim);[33] the cell column trophoblast (CCT). Three described the placental immune repertoire: placental

Please cite this article in press as: Valdes et al., Maternal smoking in early pregnancy disrupts placental function through syncytiotrophoblast and macrophage dysregulation, Cell Systems (2026), https://doi.org/10.1016/j.cels.2026.101785

CellPress
OPEN ACCESS

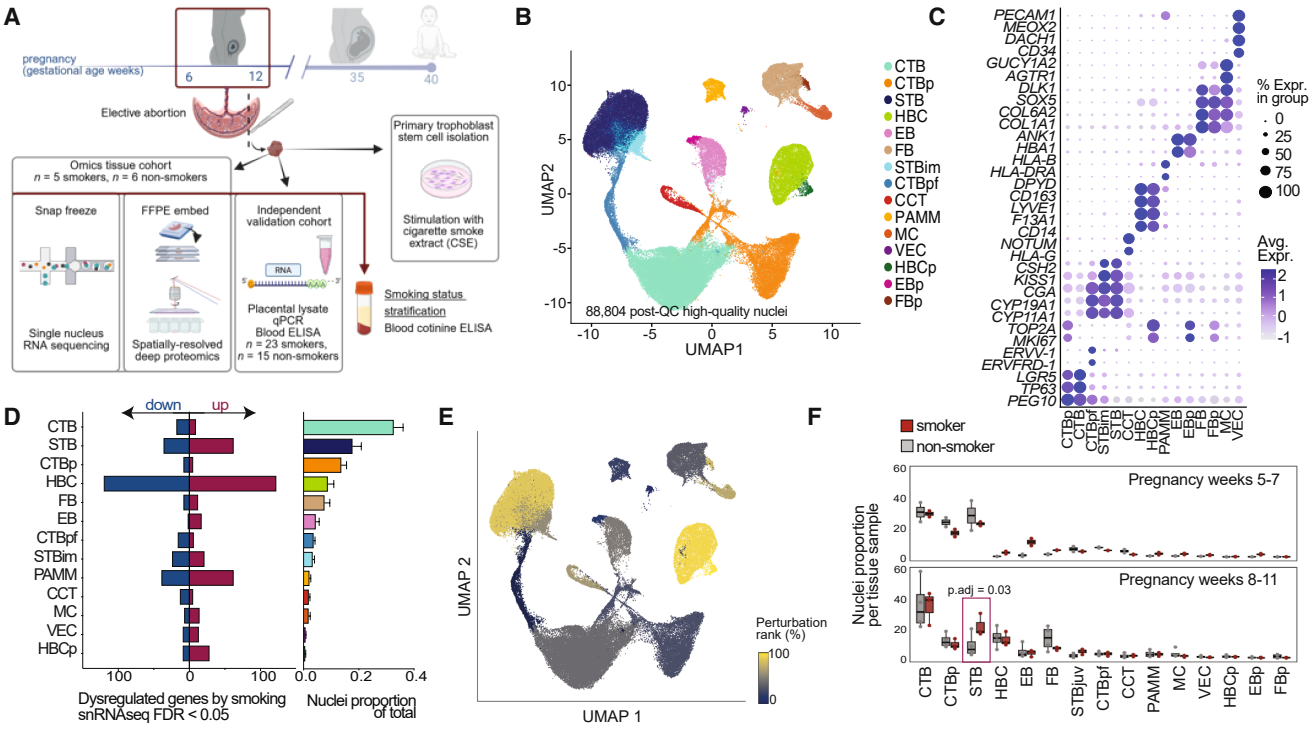

Figure 1. Maternal smoking induces phenotype-specific gene expression dysregulation patterns, with the STB and HBCs being most affected

(A) Schematic representation of study design and samples used. Two main cohorts were included: the "omics cohort" and an "independent validation cohort," both of which stratified maternal smoking status based on serum cotinine levels and self-reporting. In addition, primary trophoblast cells isolated from self-reported non-smokers were used for functional *in vitro* validations. FFPE, formalin-fixed paraffin-embedded; ELISA, enzyme-linked immunosorbent assay; qPCR, quantitative polymerase chain reaction. Created with BioRender.com.

(B) Uniform manifold approximation and projection (UMAP) visualization of harmonized dataset colored by the fifteen resolved and annotated cell types and states (n = 88,808 nuclei). CTB, cytotrophoblast; STB, syncytiotrophoblast; CCT, cell column trophoblast; HBC, Hofbauer cell; PAMM, placental-associated maternal macrophage; EB, erythroblast; FB, fibroblast; MC, myocyte; VEC, vascular endothelial cell; p, proliferating; pf, pre-fusion; and im, immature.

(C) Dotplot visualizing mean gene expression of the canonical literature-based markers in the annotated groups.

(D) Left: number of differentially expressed genes by maternal smoking at a 10% FDR cutoff (upregulated genes [purple] and downregulated genes [blue]). Dysregulation profiles are plotted in descending order based on the cell type or state's contribution to the total tissue nuclei. Right: bar plot of nuclei proportions of the total per annotated cell type and state as an average of all included tissues, irrespective of maternal smoking status. Mean plotted with error bars representing the standard error of the mean (SEM).

(E) UMAP embedding of harmonized dataset colored by perturbation between maternal smoking status calculated using a machine learning classifier model. Color indicates perturbation rank percentage (%) based on area under the curve measurements, where higher values (yellow) indicate higher transcriptomic perturbation.

(F) Box-and-whisker plots of nuclei tissue proportions between smokers (red) and non-smokers (gray) per annotated cell type or state group in the early (top) and late (bottom) stages of the first trimester. Each dot represents a placental tissue replicate. The box extends from the 25th to the 75th percentiles with a line at the median; whiskers extend from the minimum to maximum distribution values. Differences were calculated per gestational age by two-way ANOVA with a single pooled variance and using Sidak's multiple comparisons correction.

macrophages (Hofbauer cells, HBCs) and their proliferating state (HBCp); placental-associated maternal macrophages (PAMMs).[34] Mesenchymal populations included fibroblasts (FBs) and their proliferating state (FBp) and placental myocytes (MCs). Vascular endothelial cells (VECs), erythroblasts (EBs), and their proliferating state (EBp) were identified. Cell-cycle phase analysis showed clear and distinct separation between annotated non-proliferating and proliferating populations, with the latter mapping to the G2M and S phase-related genes (Figure S2). The most correlated transcriptional profiles were found among cell states of the same phenotype (Figure S2).

We evaluated the transcriptomic dysregulation of populations (>500 nuclei) using a pseudo-bulk approach (edgeR) via a likelihood ratio test generalized linear model framework that accounted for fetal sex and sequencing batch as covariates and corrected for multiple comparisons (Figure 1D left). Fetal sex was inferred using sex-associated genes[35,36] (Figure S1). With a 5% false discovery rate (FDR) threshold, macrophages in the dataset showed the largest magnitude of dysregulation, led by the HBC (7.6% of nuclei, 242 differentially expressed genes [DEGs] [122 up, 120 down]), PAMM (2.0% of nuclei, 101 DEGs [62 up, 39 down]), and HBCp (0.5% of nuclei, 37 DEGs [28 up, 9 down]) (Figure 1D). Within non-immune groups, the STB (19.1% of nuclei, 98 DEGs [62 up, 36 down]) and its immature state (STBim, 3.6% of nuclei, 45 DEGs [21 up, 24 down]) exhibited the largest dysregulation, despite the much higher tissue

Please cite this article in press as: Valdes et al., Maternal smoking in early pregnancy disrupts placental function through syncytiotrophoblast and macrophage dysregulation, Cell Systems (2026), https://doi.org/10.1016/j.cels.2026.101785

abundance of CTB (32.8% of nuclei, 27 DEGs [9 up, 18 down]) and its proliferating (CTBp, 14.6% of nuclei, 13 DEGs [5 up, 8 down]) and pre-fusion (CTBpf, 4.0% of nuclei, 22 DEGs [6 up, 16 down]) states. Transcriptomic dysregulation in other cell types and states include: VEC (0.7% of nuclei, 22 DEGs [13 up, 9 down]); MC (1.6% of nuclei, 21 DEGs [14 up, 7 down]); FB (6.6% of nuclei, 20 DEGs [12 up, 8 down]); EB (4.0% of nuclei, 19 DEGs [17 up, 2 down]) and CCT (2.1% of nuclei, 18 DEGs [5 up, 13 down]) (Figure 1D; Table S2). The high-magnitude dysregulation of the STB and HBC groups was validated using a machine-learning classifier framework that prioritizes and ranks cell types based on predicted biological perturbations in a high-dimensional space[37] (Figure 1E). A higher percentage rank value (calculated based on predicted areas under the curve) indicates an increased biological perturbation. Dysregulation proved to be phenotype specific (i.e., within a cell type and its associated state[s]), without evident distinct global patterns (Figure S2). ADP ribosylation factor like GTPase 17A (*ARL17A*), associated with protein trafficking and transport, was the only protein-coding gene concomitantly upregulated in trophoblast (STB, STBim, and CTBpf), immune (HBC), and mesenchymal (VEC and FB) groups (Figure S2). We found increased STB nuclei proportions in placentas from smokers (mean difference = 12.8%, $p = 0.025$, Figure 1F) and no differences for any other cell type. This was restricted specifically to the late first trimester (weeks 8–11) and was not observed in the earlier period (weeks 5–7, mean difference = −0.05%, $p = 0.9$). There was no evident depletion of a specific region of the STB cluster between smoking groups, indicating no enrichment of a specific transcriptomic profile for the higher STB nuclei numbers in smokers (Figure S2).

Together, we found widespread gene expression changes induced by maternal smoking in early pregnancy and identified the STB syncytium and HBC resident macrophages as most affected.

To shed light on the regulatory mechanisms governing trophoblast and immune response to maternal smoking in early pregnancy, we further investigated differential expression patterns of the STB and HBC, the most dysregulated cell types (Figures 2A and 2D). Of dysregulated STB genes, 9.5% map to Human Protein Atlas (HPA) annotated secreted markers, while 22.2% map to HPA-annotated membrane markers (Figure S3). Similarly, for the HBC, 8.3% of dysregulated genes map to secreted proteins, while 19% map to membrane proteins. The high proportion of dysregulated membrane and secreted genes points to compromised intercellular placental barrier communication and fetal-maternal exchange.

The AhR xenobiotic detoxification response characterized by *CYP1B1* in the placenta[29,38] was restricted to the STB phenotype, highlighting the importance of cell type-resolved analyses (Figure 2A). Dysregulated STB genes suggested an impairment in placental barrier integrity. In addition to dysregulation of important membrane components (*PHLDB2*, *ITGA6*, *SGCD*, *DSC3*, *SDK1*, and *F11R*) there was a myriad of dysregulated transporters for glutamate (*SLC1A2*), ions (*KCNA7* and *LRRC8B*), amino acids (*SLC1A4*), fatty acids (*SLC27A2*), sugars (*SLC45A4*), hormones (*SLC16A2, ESR2*), low-density lipoproteins (*LRP2*), prostaglandins (*SLCO2A1*) nucleosides (*SLC28A1*), and nucleotide sugars (*SLC35B4*) (Table S2). In addition, there was a marked upregulation of pro-angiogenic placental growth factor (*PGF*) and pro-vasculogenic adrenomedullin (*ADM*) that play critical roles in placental vascular and trophoblast development.[8,39] Functional pathway analysis described impaired fibrillar collagen remodeling of the STB barrier, with a concomitant induction of oxidation and extracellular signaling response in smokers (Figure 2B). To better understand the complex interactions between dysregulated genes, we performed network analysis and identified hub genes, defined as those with the highest connectivity across DEGs. These hub genes represent central players in the network, acting as potential regulators or bottlenecks in biological pathways (Figures 2C and 2F; STAR Methods). Identified markers clustered into functionally coherent communities (Figure 2C). Upregulated STB hub genes formed three distinct communities: metabolic regulation and redox response; immune regulation and cytoskeletal structure; angiogenesis and signal transduction. Downregulated STB hub genes also formed three distinct communities: cell adhesion and metabolism, regulation of cytoskeletal organization and cell proliferation, extracellular matrix (ECM) remodeling, and cell signaling. We predicted transcription factors (TFs) modulating hub gene dysregulation networks and found major players of trophoblast development (*EP300*, *GATA3*, *TEAD4*, and *JUND*) (Figure S3).

In the HBC, transcriptomic dysregulation is consistent with hallmarks of macrophage activation and a pro-inflammatory state, highlighted by increases in phagocytic (*CD14*, *CD63*, and *CD68*) and stress response (*S100A11*, *BCL2A1*, and *MDM2*) markers (Figure 2D). Functional pathway enrichment showed reduced signaling in Wnt/ERBB pathways and TFAP2C growth factor regulation, important players in physiological placental morphogenesis and development[40–42] (Figure 2E). In addition, a multitude of pathways associated with ribosomal biogenesis and translational capacity were upregulated in HBCs of smokers, consistent with heightened biosynthetic demands of activated macrophages. Upregulated hub gene communities in the HBC delineate main modulators of this pro-inflammatory and stress-adapted transcriptional state associated with metabolic activation and increased protein synthesis. Downregulated hub genes clustered into communities representative of tight junction and cytoskeletal regulation, ECM remodeling, and growth factor signaling. In line with these findings, TFs predicted to coordinate this dysregulation are linked to basal and stress-inducible transcriptional regulation (*TAF1*, *TAF7*, *POLR2A*, and *TP53*) (Figure S3).

These results demonstrate a striking cell type-specific transcriptional reprogramming of the STB and HBC in response to maternal smoking. Both cell types feature coordinated alterations in metabolic and structural programs capable of impairing organ development and function.[1]

Trophoblast cell types differentiate in the first trimester of pregnancy to enact specialized functions that allow for nutrient and gas exchange between mother and fetus. We used primary-derived TSCs[41,43,44] to model human trophoblast function and investigated molecular effects of cigarette smoke components on the STB phenotype after *in vitro* directed TSC fusion (Figure 3). We additionally characterized the proteomic landscape of this model by high-sensitivity mass spectrometry (n = 8,837 protein IDs) (Figure S4), where we observed clear proteomic shifts between undifferentiated and differentiated states, encompassing phenotypic and functional protein markers.

Please cite this article in press as: Valdes et al., Maternal smoking in early pregnancy disrupts placental function through syncytiotrophoblast and macrophage dysregulation, Cell Systems (2026), https://doi.org/10.1016/j.cels.2026.101785

CellPress
OPEN ACCESS

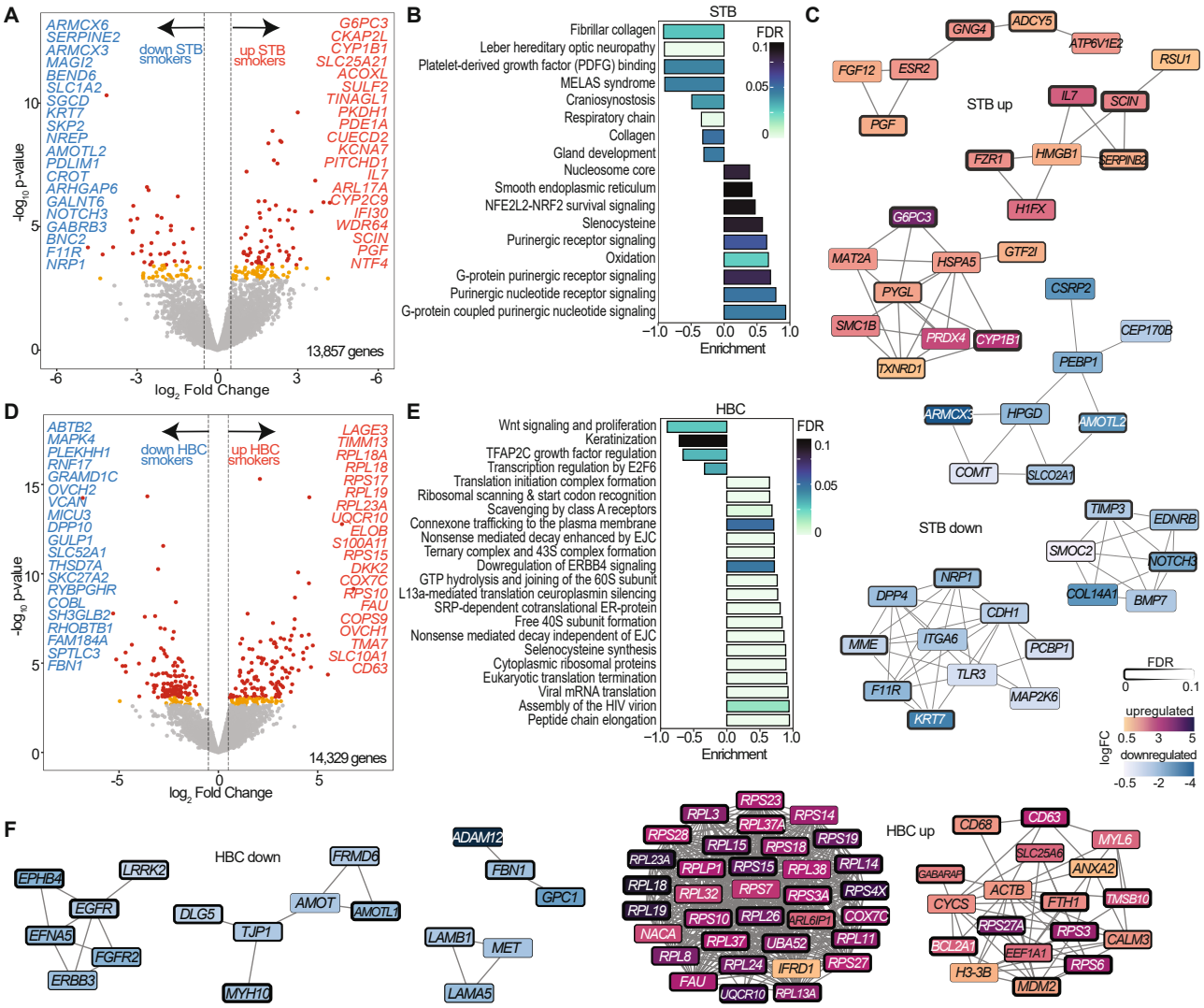

Figure 2. STB and HBC transcriptomic dysregulation and associated functionally enriched pathways and master modulators

(A and D) Volcano plot of differentially expressed genes (DEGs) analyzed by snRNA-seq from STB (A) and HBCs (D). The top 20 most dysregulated genes are shown. DEGs were calculated using semi-bulk counts per cell type via a generalized linear model and Benjamini-Hochberg correction in the edgeR package.

(B and E) Pathway enrichment analysis of dysregulated STB (B) and HBC (E) genes (absolute FC > 0.25, FDR < 0.1). Enrichment was done based on ranked log fold changes spanning the gene set enrichment analysis (GSEA), Reactome, and the WikiPathways databases. Positive enrichment values represent pathways enriched in smokers; negative values represent those enriched in non-smokers. Bar color is mapped to dysregulation FDR.

(C and F) Hub genes of upregulated (log2FC > 0.25, FDR < 0.1) and downregulated (log2FC < −0.25, FDR < 0.1) tissue STB (C) and HBC (F) genes by maternal smoking in early pregnancy, based on the protein-protein interaction background stringDB network followed by topological analysis. Color represents log2FC; node border thickness corresponds to differential expression analysis FDR.

Because tobacco smoke has over 7,000 constituents, cigarette smoke extract (CSE) containing nicotine, cotinine, and other soluble constituents acts as a better model than nicotine alone to study the biological effects of smoking.[46] We generated standardized CSE using 1R6F reference small batch research cigarettes[47] as previously described in the literature,[48] where cigarette smoke is bubbled through cell culture medium at a controlled rate (Figure 3A). We confirmed expected nicotine and cotinine concentrations in the CSE by mass spectrometry (Figure 3B). Additionally, we characterized volatile and semi-volatile constituents by gas chromatography-mass spectrometry (GC-MS), as these act as potential ligands for smoke-related cellular responses (Figure S5).

At first, we validated the dysregulation of specific marker genes of STB physiology previously described by snRNA-seq. After validating the time course (Figure S5), we stimulated STBs derived from TSCs with CSE for 6 h. By qPCR, we revealed the induced expression of xenobiotic enzymes *CYP1A1* and *CYP1B1*, heme oxygenase-1 (*HMOX1*), and important pro-angiogenic *PGF* and *ADM* (Figure 3C). We further confirmed these findings in our independent validation cohort. Despite the STB only consisting of 19.1% of total placental nuclei, the upregulation of *CYP1B1*, *PGF*, and *ADM* in the smoking group is still captured in the whole placental tissue lysate (Figure 3D). We found the induction of *PGF* expression to have systemic implications, as circulating PlGF

Please cite this article in press as: Valdes et al., Maternal smoking in early pregnancy disrupts placental function through syncytiotrophoblast and macrophage dysregulation, Cell Systems (2026), https://doi.org/10.1016/j.cels.2026.101785

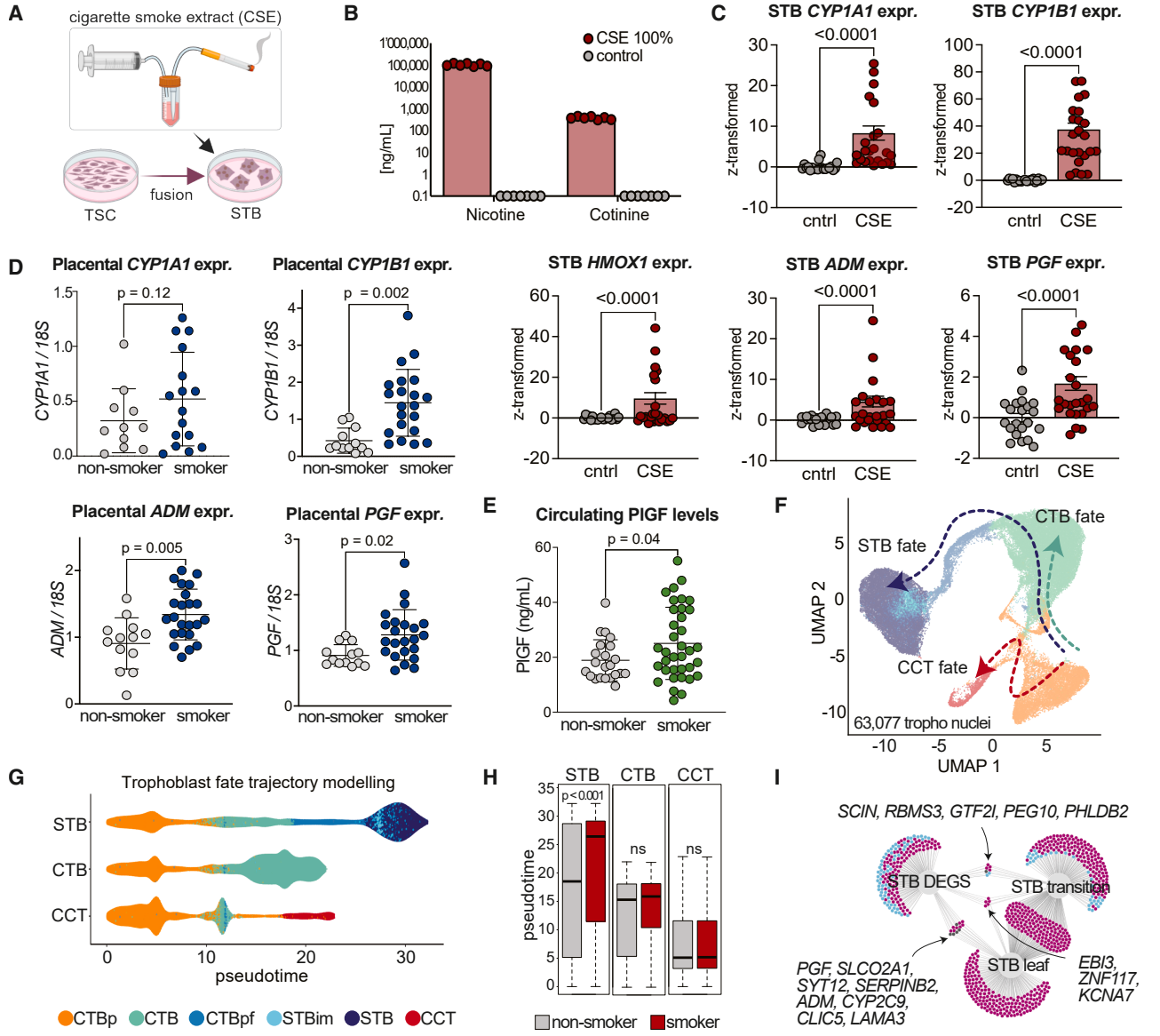

Figure 3. Validation of smoking effects on STB xenobiotic stress and pro-angiogenic signature

(A) Schematic representation of cigarette smoke extract (CSE) preparation used for *in vitro* stimulations as reported in Gellner et al.[45] Reference research cigarettes are bubbled through cell culture medium at a fixed rate. The resulting medium is acidic, so the pH is adjusted and sterile filtered. For reproducibility, 100% CSE generated from 10 experiments were pooled into batches (n = 4 total batches). Created with BioRender.com.

(B) CSE media were validated by nicotine and cotinine levels analyzed by mass spectrometry.

(C) Gene expression measured by qPCR in STB-fused primary cells after 6 h of CSE stimulation (n = 3 independent experiments with technical sextuplicates each). Data were normalized with a z transformation per experiment, as qPCR was measured in different plates. Significance was assessed with unpaired two-tailed Mann-Whitney tests. Data presented as mean ± SEM.

(D) Gene expression measured via quantitative PCR of whole placenta lysate of an independent cotinine-validated maternal smoking in early pregnancy cohort (n = 23 smokers and n = 15 non-smokers). Differences were assessed using a multiple linear regression model with maternal age, maternal BMI, and gestational age as covariates. Data presented as mean ± SEM.

(E) Serum levels of placental growth factor in maternal serum measured via enzyme-linked immunosorbent assay (ELISA) in an independent cotinine-validated pregnancy cohort (n = 36 smokers and n = 22 non-smokers). Differences were assessed using a multiple linear regression model with maternal age, maternal BMI, and gestational age as covariates. Data presented as mean ± SEM.

(F) Uniform manifold approximation and projection (UMAP) embedding of trophoblast types and states used for trajectory modeling (n = 63,077 total nuclei; n = 27,055 nuclei from smokers and n = 36,022 nuclei from non-smokers).

(G) Scatter plot of modeled pseudotime values separated by inferred lineage. Each dot represents a nucleus, colored by its annotated cell type or state membership.

(legend continued on next page)

Please cite this article in press as: Valdes et al., Maternal smoking in early pregnancy disrupts placental function through syncytiotrophoblast and macrophage dysregulation, Cell Systems (2026), https://doi.org/10.1016/j.cels.2026.101785

protein levels are elevated in the plasma of smoking mothers (mean difference 6.2 ± 2.7 ng/mL, $p = 0.03$) (Figure 3E).

In light of our findings of elevated STB nuclei proportions in smokers (Figure 1F) and the upregulation of pro-angiogenic PGF and ADM, with known roles in trophoblast development, we further investigated whether maternal smoking may impact healthy trophoblast development using pseudotime analysis *in silico*. Here, cell differentiation dynamics are reconstructed based on individual nuclei gene expression fingerprints in combination with the high-dimensional uniform manifold approximation and projection (UMAP) space to identify global lineage structures (Figures 3F–3H). Transcriptomic data from the nuclei of the six trophoblast cell types and states (CTBp, CTB, CTBpf, STB, STBim, and CCT) were used for trajectory inference (n = 63,077 nuclei, n = 27,055 smokers, and n = 36,022 non-smokers) (Figures 3F and S6). To avoid cell annotation label bias, data were re-clustered (resolution 0.3 yielding 10 clusters), and clusters were used for trajectory modeling (Figure S6). As a result, three biologically relevant lineages were inferred, starting from one of the two proliferating CTB (CTBp) subclusters, toward the multinucleated STB (STB fate), toward the invasive CCT (CCT fate), and between the proliferating and non-proliferating CTB (CTB fate) (Figures 3F, 3G, and S6; STAR Methods).

To better understand trophoblast differentiation, key regulatory intermediates (transition) and terminal effector (leaf) genes were inferred using the non-smoker nuclei exclusively (n = 36,022 nuclei) (Figure 3C; STAR Methods; Tables S3 and S4). Transition genes represent temporally expressed genes that change dynamically across pseudotime and are likely modulators of the differentiation process. Leaf genes demarcate the bifurcation and differentiated states.

When comparing trajectories between smokers and non-smokers, we found highly differential pseudotime distributions exclusively in the STB lineage (Figure 3H). This suggests a preferential differentiation toward the modeled STB lineage with a small effect size (odds ratio 1.02; i.e., 2% preference for the STB lineage per unit of pseudotime) in smokers compared with non-smokers. Albeit small, this increase appears to be functionally relevant, as transition and leaf genes closely linked to placental health are dysregulated in the STB (Figure 3I). Three genes dysregulated by smoking were identified as both leaf and transition markers, including *KCNA7*, *ZNF117*, and *EBI3*, involved in ion transport, transcriptional regulation, and immune modulation, respectively. Dysregulated transition genes were associated with cytoskeletal remodeling, trophoblast lineage specification, and gene expression control, highlighting their putative role in skewed differentiation toward the STB in smokers. Leaf genes overlapping with STB DEGs reflected disruptions in angiogenesis, cell adhesion, prostaglandin transport, and ECM organization, all of importance for barrier function homeostasis.

Trophoblast differentiation modeling and *in vitro* validation revealed a subtle yet preferential shift toward the STB lineage in smokers. Smoking-associated dysregulation was linked to regulatory and effector genes governing cell signaling and cytoskeletal remodeling. These data support the notion that smoking disrupts molecular programs of placental function and may influence trophoblast fate decisions.

DVP reveals mitochondrial STB accumulation and hemostatic involvement

As the next step to understand the early pregnancy molecular dysregulation by maternal smoking, we applied a modified DVP,[31] workflow, where cell-type-specific regions of interest were annotated in QuPath via the openDVP framework,[49] and subjected to automated laser microdissection and ultra-high sensitivity label-free mass-spectrometry-based proteomics (Figure 4A). The main cell types of interest based on snRNA-seq findings included HBCs that constitutively express cluster of differentiation CD163 (filled arrow), CTBs characterized by epithelial cadherin (E-cadherin, coded by the *CDH1*; empty arrow), and the STB layer that is E-cadherin negative and on the apical side of CDH1-positive villous structures, where maternal blood circulates (dotted arrow) (Figures 4B and 4C). To exclude potential contamination from the cell column trophoblast, we used serial section histocompatibility antigen class I, G (HLA-G) immunostaining and selected only HLA-G negative regions. We annotated and collected STB regions (apical surface, CDH1neg/HLAGneg) as well as single HBC (CD163pos) and CTB (CDH1pos) cells for proteomics measurement. This technique allowed for the deep proteomic profiling of the multinucleated STB layer, which has been historically impossible due to the inability to derive this syncytium into a single-cell suspension.

We microdissected and collected approximately 200 cells (or their equivalent area) across the whole tissue section per phenotype technical replicate from six placental tissues (n = 3 smokers and n = 3 non-smokers, all female fetuses) also included in the snRNA-seq cohort. While this design increases power to detect smoking-associated changes, it precludes elucidation of sex-specific effects of maternal smoking, for which further studies are needed. We characterized phenotype-specific signatures at a detection range of 3,100 (HBC) to 4,370 (CTB) proteins (Figure 4D). We observed cell-type specificity of quantified samples and excellent concordance between the microdissected phenotypes of interest and their proteomic profile of canonical markers (Figures 4E and 4F). This alone constitutes the most comprehensive cell type-resolved proteomic characterization of the developing human placenta to date, as this has only been previously performed at the whole-tissue lysate level at a comparable depth (4, 239 proteins).[50]

We found vast proteomic differences in the STB and HBC between smokers and non-smokers, with a similar amount of

(H) Box plots of pseudotime distributions per lineage inferred (spanning from progenitor to endpoint) separated by maternal smoking status. Boxes represent interquartile range (IQR) from first to third quartile; median is indicated by the line inside the box. Whiskers extend to 1.5 times the IQR from each quartile. Significance between smokers and non-smokers for all three lineages was tested through permutation, Kolmogorov-Smirnov, and generalized linear model tests. (I) Overlap between dysregulated genes in the STB phenotype and trajectory-modeled STB leaf and transition genes. For the overlap, STB DEGs included those with an FDR < 0.1 and log2FC ± 0.25; transition genes included those with an FDR < 0.05 and absolute Spearman correlation of >0.4; leaf genes included those with an FDR < 0.05, logFC > 3, and log counts per million of > 4. Colors indicate agreement between upregulated (magenta) and downregulated (blue) markers. TSC, trophoblast stem cell; STB, syncytiotrophoblast; CTB, cytotrophoblast; CCT, cell column trophoblast; p, proliferating; pf, pre-fusion; im, immature.

Please cite this article in press as: Valdes et al., Maternal smoking in early pregnancy disrupts placental function through syncytiotrophoblast and macrophage dysregulation, Cell Systems (2026), https://doi.org/10.1016/j.cels.2026.101785

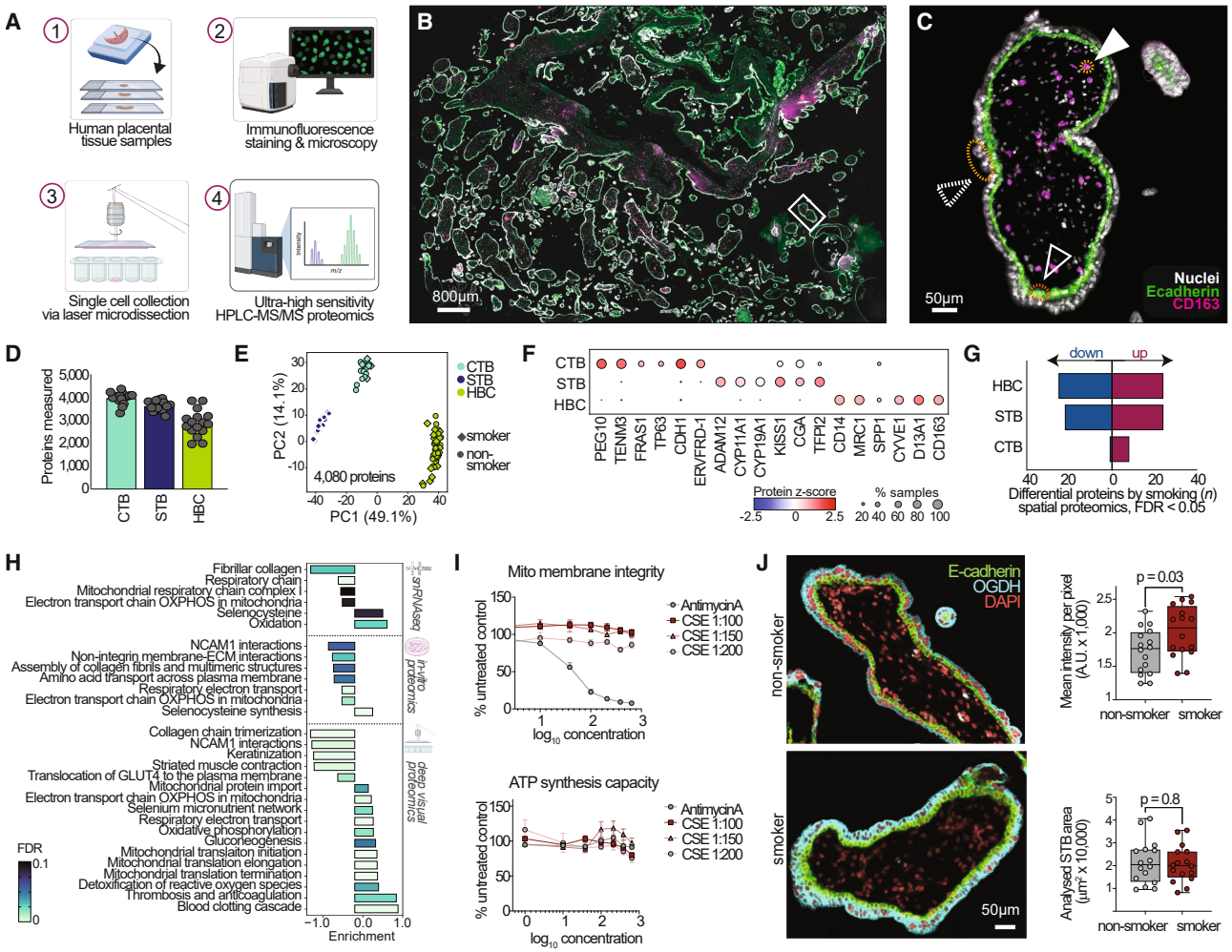

Figure 4. DVP reveals that maternal smoking contributes to STB mitochondrial accumulation

(A) Schematic representation of the DVP workflow indicating four key steps. Created with BioRender.com.

(B) Representative immunofluorescence staining of first-trimester control sample used for the spatial proteomics, indicating cytotrophoblasts (CTB, green, E-cadherin), Hofbauer cells (HBC, magenta, CD163), and nuclei (gray, Hoechst staining of nuclear DNA). White square is indicating view field of (C).

(C) Representative area of whole tissue immunofluorescence staining shown in (B). Specific annotated regions are indicated: White arrowhead, $CD163^{+}$ HBC; dashed arrowhead, multinucleated STB; and white outlined arrowhead, E-cadherin+ CTB.

(D) Numbers of proteins in microdissected CTB, STB, and HBC detected by mass spectrometry.

(E) Principal component analysis (PCA) of proteomic profiles of microdissected CTB, STB, and HBC. Each point represents a technical replicate measured ($n = 3$ smokers and 3 non-smokers with technical quadruplicates per cell phenotype group).

(F) Dotplot visualizing abundance of the canonical literature-based markers in the microdissected placental cell types. Colors represent Z scores of protein abundances across groups.

(G) Number of differentially abundant tissue proteins by maternal smoking at a 5% FDR threshold. Upregulated proteins are in magenta and downregulated in blue. Differential abundance was calculated on pseudo-bulk counts per cell type or state using a generalized linear model with a Benjamini-Hochberg FDR correction.

(H) Summary of pathway enrichment analysis of dysregulated STB from results of snRNA-seq (upper), *in vitro* proteomics (middle), and spatial proteomics (lower) as indicated by scheme (absolute FC > 0.25, FDR < 0.1). Enrichment was done based on ranked log fold changes spanning the gene set enrichment analysis (GSEA), Reactome, and the WikiPathways databases. Positive enrichment values represent pathways enriched in smokers, and negative values represent those enriched in non-smokers. Bar color is mapped to dysregulation FDR.

(I) Mitochondrial toxicity analysis of *in vitro* STB (differentiated primary TSCs) induced by the indicated concentration of cigarette smoke extract (CSE) in cell culture media as a percentage of untreated control media. The upper panel presents mitochondrial membrane integrity and the lower panel, the corresponding adenosine triphosphate (ATP)-synthesis capacity. Antimycin A represents a positive mitochondrial toxicity by inducing reduced membrane integrity with unchanged ATP synthesis capacity.

(J) Left: representative immunofluorescence staining of first-trimester villi of non-smoker (upper) and smoker (lower) indicating E-cadherine (CTB, green), the mitochondrial marker 2-oxoglutarate dehydrogenase (OGDH, blue), and nuclei (red, Hoechst staining of nuclear DNA). Upper right: quantification of mean intensity per pixel in the STB regions analyzed using quantitative pathology (QuPath) software. Each dot represents a measured villi area. Significance tested by two-tailed unpaired *t* test with Welch's correction. AU, arbitrary units. Lower right: mean STB areas analyzed (mm2) used for the quantification of OGDH intensity per group. Significance tested by two-tailed unpaired *t* test with Welch's correction. Data presented as mean ± SEM. ($n = 4$ smokers and $n = 4$ non-smokers in quadruplicate villi areas per tissue.) STB, syncytiotrophoblast; CTB, cytotrophoblast; HBC, Hofbauer cell.

Please cite this article in press as: Valdes et al., Maternal smoking in early pregnancy disrupts placental function through syncytiotrophoblast and macrophage dysregulation, Cell Systems (2026), https://doi.org/10.1016/j.cels.2026.101785

CellPress
OPEN ACCESS

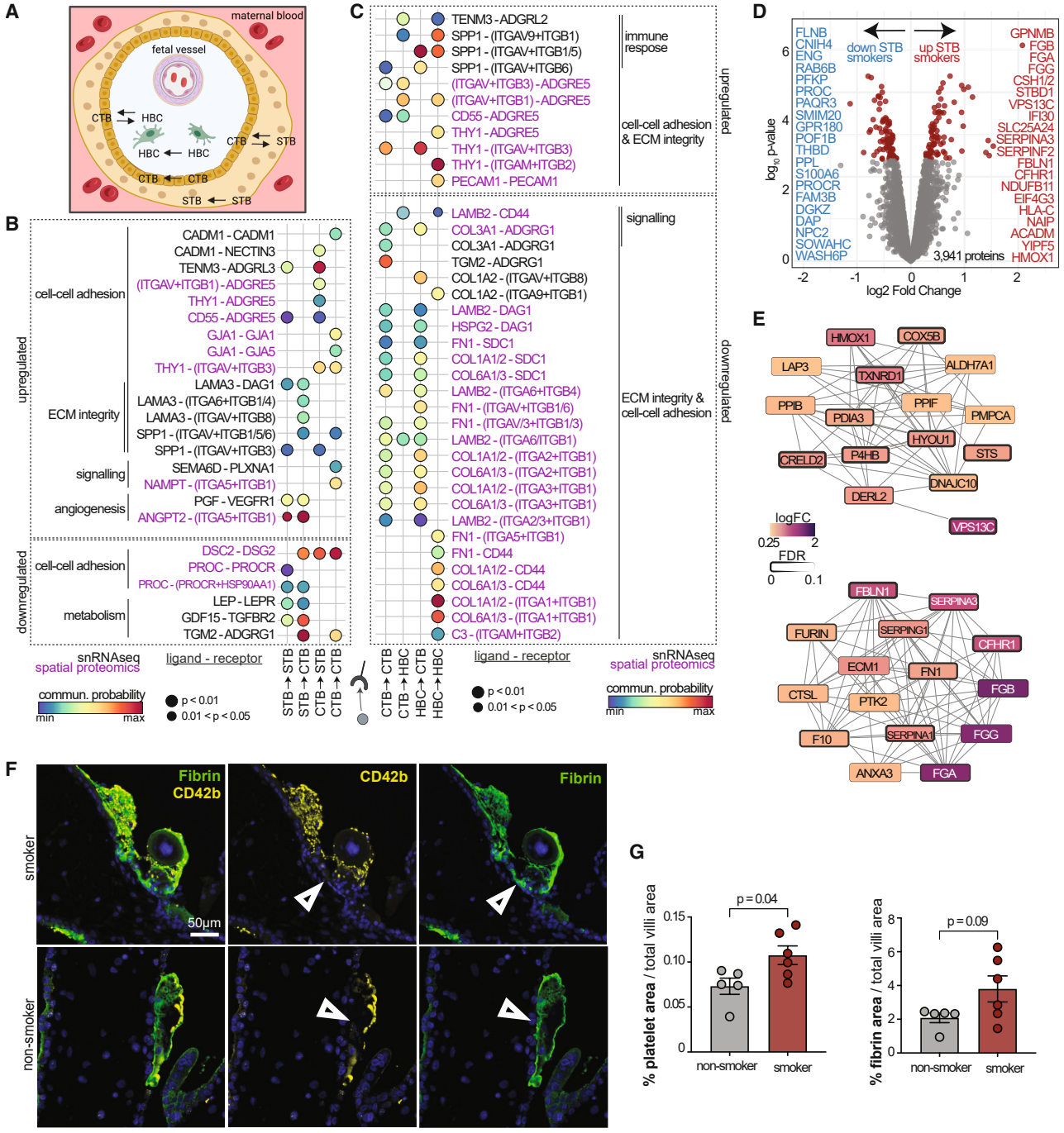

Figure 5. Maternal smoking impairs intra-organ communication

(A) Schematic representation of a placental villus cross-section bathed in maternal blood within the intervillous space. Cell-cell interactions of interest and their dysregulation are noted. Created with BioRender.com.(B and C) Significantly dysregulated cell-cell communication in the trophoblast layer (B) and tissue-resident immune (C) compartments by smoking. Ligand-receptor pair communication was systematically inferred per omics modality (snRNA-seq and DVP) as well as per condition separately using CellChat.[51] Inferences per modality were integrated between conditions, and interaction strength and flow were compared by Welch's *t* test. Dot color indicates communication probability of ligand-receptor pairs; dot size represents the *p* value, text color indicates modality of origin for significant hit.

(D) Volcano plot of differentially expressed proteins (DEGs) analyzed by DVP from STB. The top 20 most dysregulated genes are shown. DEGs were calculated using semi-bulk counts per cell type via a generalized linear model and Benjamini-Hochberg correction in the edgeR package.

(E) Hub genes of upregulated (log2FC > 0.25, FDR < 0.1) and downregulated (log2FC < −0.25, FDR < 0.1) tissue STB (C) and HBC (F) proteins by maternal smoking in early pregnancy, based on the protein-protein interaction background stringDB network followed by topological analysis. Color represents log2FC; node border thickness corresponds to differential expression analysis FDR.

(legend continued on next page)

Please cite this article in press as: Valdes et al., Maternal smoking in early pregnancy disrupts placental function through syncytiotrophoblast and macrophage dysregulation, Cell Systems (2026), https://doi.org/10.1016/j.cels.2026.101785

differentially abundant (DA) proteins (FDR < 0.05; HBC, *n* = 49 DA [24 up, 25 down]; STB, *n* = 46 DA [24 up, 22 down]). The CTB displayed a low number of DA proteins, in line with snRNA-seq findings (*n* = 9 DA; 8 up, 1 down) (Figure 4G; Table S5). STB dysregulated proteins were involved in oxidative stress response, protein folding, metabolic processes, extracellular matrix organization, immune response, and pro-coagulation dynamics. Thus, we not only validated snRNA-seq-based main molecular mechanisms by proteomics, but we also identified an additional role of hemostasis at the maternal-fetal interface unable to be elucidated by transcriptomics alone. In addition, we performed a deep proteomic analysis of the *in vitro* model we introduced in Figure 3 (*n* = 8,837 protein IDs). After *in vitro* TSC differentiation toward the multinucleated endocrine STB phenotype, exposure to CSE for 48 hours led to the dysregulation of 282 proteins (FDR < 0.05) (Table S6).

In the STB, we found functional pathway enrichment for selenocysteine synthesis across the three modalities (snRNA-seq, DVP, and *in vitro*). Markers involved in cell adhesion, ECM integrity, and cellular transport were downregulated (Figure 4H). Both the snRNA-seq and *in vitro* proteomics identified mitochondrial function pathways, primarily oxidative phosphorylation (OXPHOS), to be impaired in the STB of smokers. However, in the DVP results, we instead found a stark upregulation of mitochondrial machinery and function-related pathways (Figure 4H). Thus, we hypothesized that cigarette components may act as a mitochondrial toxin to the STB, inducing dysfunction and leading to accumulation in the tissue. To evaluate this, we used a cell-based multiplexed assay method that predicts mitochondrial dysfunction specifically as a result of xenobiotic insult (Figure 4I). We found that CSE treatment of *in vitro* differentiated STBs had no impact on mitochondrial membrane integrity (upper panel) or ATP synthesis capacity (lower panel), as curves deviated from our positive control mitochondrial toxin antimycin A (Figure 4I). This phenomenon was consistent when cells were exposed to the same CSE concentration used for previous mRNA and proteomic experiments (1:200 dilution of 100% stock) or to higher non-lethal amounts (1:150 and 1:100 dilutions). To further reconcile these findings, we performed immunofluorescence staining of the citric acid cycle oxoglutarate dehydrogenase (OGDH) enzyme, localized to the mitochondrial membrane, on the same tissues profiled by snRNA-seq and DVP (Figure 4J, left). We confirmed an accumulation of mitochondria in the STB of smokers compared with that of non-smokers based on STB area intensities, with comparable areas analyzed per tissue (Figure 4J, right; *n* = 4 areas per tissue).

Our findings indicate that soluble components of cigarette smoke do not directly act as mitochondrial toxins to the STB. Rather, an adaptive accumulation of mitochondria in the STB of smokers may represent an adaptive response to intracellular stress and increased energy demands.

To better understand specific cell-cell interactions between the most altered cell types (STB and HBC), we used CellChat to predict dysregulated communication, integrating the results of snRNA-seq and DVP proteomics results (Figures 5A–5C; STAR Methods; Table S7). We included the CTB in these comparisons as the CTB monolayer is in direct contact with the STB and physically separates the syncytium from the HBC and stroma. To this end, we calculated paracrine interactions between the STB-CTB and the CTB-HBC as well as autocrine signaling within each cell type.

We identified a global, widespread dysregulation involving integrins, cell-adhesion transmembrane receptors acting as ECM-cytoskeletal linkers and transducers. Within the trophoblast comparison (STB-CTB), upregulated pro-angiogenic signaling was restricted to STB PGF and ANGPT2 ligands acting on the STB itself and on the CTB (Figure 5B). Tissue transglutaminase (TGM2) was downregulated in trophoblast communication. The *in vitro* inhibition of this protein impairs human trophoblast intercellular fusion and disrupts stabilization of particulate material physiologically shed into the maternal circulation throughout pregnancy.[52] Further, our results suggest that dysregulated mechanical strength and stability of the trophoblast basal membrane by smoking is underpinned by the activation of the G-protein coupled receptors, ADGRE5 and ADGRL3; adhesion molecules, CADM1 and NECTIN3; and gap-junction proteins, GJA1 and GJA5; concomitant with impaired desmosome interactions (DSC2-DSG2) (Figure 5B). The desmosome connects CTBs to each other laterally and contributes to the attachment of the CTB to the overlying STB.[53] Within the tropho-immune comparison (CTB-HBC), we identified osteopontin (SPP1)-integrin signaling as a driver of the HBC immune response (Figure 5C). This secreted glycoprotein, an important component of the ECM,[54] promotes an *in vitro* immune response in murine macrophages and human trophoblast cells (Figure S8). Further functional studies are essential to establish a causal role for predicted interactions.

Within the HBC only, ECM integrity was mainly impaired by fibronectin, laminin, and collagen integrin signaling. In addition, we found PECAM1 signaling, a marker associated with HBC-mediated angiogenesis, upregulated in within-HBC interactions (Figure 5C). In both STB-CTB and CTB-HBC analyses, we observed an upregulation in THY1 ligand signaling, a marker and putative modulator of placental vascular development (Figures 5B and 5C).

Another interesting finding from the DVP dysregulation of the STB was a tissue proteome enrichment of the thrombo-hemostatic network (thrombosis and anticoagulation, blood clotting cascade) (Figure 4H). Strongly upregulated proteins in this cell type include fibrinogen alpha (FGA), beta (FGB), and gamma (FGG) chains, as well as members of the SERPINE family (Figure 5D; Table S5). To reveal modulators behind the upregulated proteins, we performed network analysis and calculated hub genes that identified two distinct communities representing proteins associated with oxidative stress response, protein folding, and metabolic processes (upper cluster) and proteins involved in coagulation and immune response (bottom cluster)

(F) Human first-trimester placental tissue of non-smokers (*n* = 5) and smokers (*n* = 6) from the omics cohort subjected to double immunofluorescence for fibrin and the platelet marker CD42b showed perivillous fibrin deposition and adherence of platelets in smokers (upper) and non-smokers (lower).
(G) A software-based approach identified the total villi area, total fibrin area, and adherent platelet area. Normalization to the total villi area revealed a significant increase in adherent platelets in smokers (left) and a trend toward increased fibrin deposition in villi (right). Significance was tested using a two-tailed unpaired *t* test. Data presented as mean ± SEM.

Please cite this article in press as: Valdes et al., Maternal smoking in early pregnancy disrupts placental function through syncytiotrophoblast and macrophage dysregulation, Cell Systems (2026), https://doi.org/10.1016/j.cels.2026.101785

(Figure 5E). Platelet activation at the maternal-fetal interface has been previously described to directly underpin or propagate placenta-associated pregnancy pathology,[55] so we further validated this finding by immunofluorescence staining of the omics tissue cohort (Figure 5F). Upon normalization to the entire villous area, we found significant increases in platelet adhesion to the trophoblast barrier, concomitant with a trend toward higher fibrin deposition in maternal smokers (Figures 5G and S8).

Through these analyses, we introduce how maternal smoking disrupts placental cell communication and unveil maternal platelet activation and adhesion with enhanced fibrin deposition as a potential novel modulator of deleterious smoking-induced effects in the early human placenta.

DISCUSSION

This work unveils the phenotype-resolved profound impact that maternal smoking has on the transcriptomic and proteomic tissue profiles of the developing human placenta. We reveal effects of maternal smoking on all cell types and states of this organ, with the strongest dysregulation in the multinucleated and endocrine STB layer and tissue-resident macrophages (HBC). Although not the most abundant cell types in early pregnancy, they play important roles in mediating placental function. The STB is in direct contact with maternal blood and plays a pivotal role as a barrier interface with a unique endocrine capacity.[6,56] The HBC are of fetal origin and play a fundamental role in placental development and maternal-fetal nutrient exchange.[57] We describe orchestrated alterations in detoxification, metabolism, and structural pathways in the STB and HBC that may compromise organ development and function and could affect fetal growth. Our findings highlight the importance of phenotype-resolved molecular profiling in discerning processes underpinned by low-abundance yet highly physiologically relevant cell types.

Maternal smoking has been associated with sharp increases in third-trimester whole-tissue oxidative stress. Hoch et al. reported decreases in ROS-mediated DNA damage (41%) in whole tissue lysates, suggesting a compensatory response to smoking-induced intracellular stress,[58] while studies that directly investigate the impact of smoking on HBCs are sparse. Sbrana et al. described by immunostaining that at term, HBCs in placentas from smokers exhibit significantly increased oxidative DNA damage, suggesting that maternal smoking induces oxidative stress directly within fetal macrophages.[59] In our work, we were able to deeply phenotype the effects of smoking on the HBCs specifically. We found a smoking-induced upregulation of CD14, CD63, and CD83 that indicates an activation of phagocytosis and response to placental inflammation, which is also observed in chorioamnionitis.[60] A further indicator of placental inflammation was the CD68 upregulation in HBC from smoking women that we found. In a mouse model for FGR, an induction by uric acid leads to an upregulation of placental inflammation and $CD68^{+}$ macrophages.[61] Bezemer et al. proposed a putative vicious cycle in FGR where failed maternal-fetal tolerance, placental maldevelopment, oxidative stress, and a placental inflammatory immune response promote maladaptive processes.[62] Our data support that high transcript and protein turnover in the HBC, coupled with its pro-inflammatory profile in maternal smoking, conforms to this auto-amplifying vicious cycle that may contribute to placental insufficiency at term. Further smoking-induced regulated genes we identified in the HBC are CCL4, CCL3L1, and PBX1, all of which have been previously implicated in the pro-inflammatory induction of FGR.[63–65]

We provide pathway- and network-level evidence that intracellular oxidative stress in the trophoblast is restricted to the STB, and already begins in the first trimester of pregnancy, persisting until birth.[59,66] We found no significant dysregulation in gene expression or protein abundance of hallmark markers for hypoxia, ferroptosis, or apoptosis, suggesting these processes do not modulate smoke-induced STB stress. Moreover, we found no dysregulation in superoxide dismutase or glutathione peroxidase activity, the primary free radical detoxification modulators in the human placenta at term.[67] Instead, we discovered three main mechanisms explaining maternal smoking-induced STB stress.

First, the sharp activation of downstream effectors CYP1B1 and CYP1A1 of the xenobiotic response aryl-AhR pathway. The absence of free radical scavengers in maternal smokers found by us and others[68] indicates an accumulation of active phase I enzyme metabolites, unable to be adequately inactivated by phase II enzymes, which contribute to oxidative stress and impaired cell function at a critical stage of placental development. In the intestinal epithelium, CYP1A1 and CYP1B1 activity is protective against chemical-induced damage of cell-cell tight junctions.[69] Thus, AhR activation may be protective to the CTB monolayer and explain the lower dysregulation in this cell type. Second, our findings reveal an adaptive mitochondrial accumulation within the STB of smokers, representing an early-stage energy metabolism adaptation. While this may preserve cellular function in the acute state, chronic effects could pose long-term risks to placental efficiency and fetal development. We indicated that soluble cigarette smoke components did not exhibit mitochondrial toxicity *in vitro*, despite tissue snRNA-seq and *in vitro* CSE-stimulated STB consistently indicating impaired OXPHOS capacity by cigarette smoke components. Physiological levels of accumulated mitochondrial-generated ROS likely compound increases in intracellular stress. Third, fibrinogen deposits on the STB surface as a response to the maternal coagulation cascade likely contribute to increased stress, since platelet activation strongly triggers oxidative stress and ROS production.[70] In the healthy human placenta, STB degeneration is routinely filled by fibrin spots as a result of clotting, with up to 7% of the syncytium containing fibrin spots in the healthy placenta at term.[71] Activation of maternal platelets in placenta-associated pregnancy pathologies directly underpins or propagates the underlying pathophysiology,[55] while increased fibrin deposition in the perivillous space is strongly associated with FGR.[72,73]

In addition, we describe widespread dysregulation of key ion, nutrient, and hormone transporters in the STB, coupled with higher metabolic needs and glucose consumption. Increases in fibrin plaques can additionally alter the diffusion transport capacity of the placenta.[9] Therefore, effects of maternal smoking on the functional syncytial feto-maternal barrier can be interpreted as directly impairing transport to and from the fetal

Please cite this article in press as: Valdes et al., Maternal smoking in early pregnancy disrupts placental function through syncytiotrophoblast and macrophage dysregulation, Cell Systems (2026), https://doi.org/10.1016/j.cels.2026.101785

compartment, adversely impacting fetal development and growth, causally linked to this behavior.[16]

Furthermore, our results support a moderate preferential fusion and differentiation toward the STB phenotype in smokers. In the human placenta, CTB fusion is mechanistically governed by increases in intracellular cyclic adenosine 3′/5′-monophosphate (cAMP) and protein kinase A (PKA) activity induced by the autocrine-paracrine loop binding of human chorionic gonadotropin (hCG) (coded by *CGA* and *CGB* genes) to the luteinizing hormone/choriogonadotropin transmembrane receptor (LHCGR).[74–77] The primary modulators of this process include P300 and GCM1. While we found no differences in hCG and luteinizing hormone (LH) levels between groups, we revealed that kisspeptin (KISS1), an snRNA-seq STB transition gene that directly activates cAMP pathway activity,[78] is highly upregulated in the tissue STB proteome by smoking. Additionally, in primary cells stimulated with CSE, the vasoactive intestinal peptide receptor 1 protein was markedly increased. This protein directly activates adenylate cyclase (AC), the only enzyme known to generate cAMP from ATP.[79] Our molecular findings suggest that STB fusion is indirectly affected by biochemical activator dysregulation, not directly via aberrances in morphological fusion drivers.

The inducible isoform of heme oxygenase (HO-1 encoded by *HMOX1*) is increased at the tissue protein, and *in vitro* CSE stimulated STB gene expression and protein levels. Network analysis identified HMOX1 as a master modulator of the upregulated STB protein response to maternal smoking. HO-1 is induced in response to ROS-associated cellular stress in many tissues with protective effects.[80] The heme oxygenase (HO) system also represents the main source of endogenously produced carbon monoxide (CO) in the body.[81] CO exposure is pro-angiogenic at the murine maternal-fetal interface, without detrimental effects on pregnancy or fetal outcomes.[82,83] In human endothelial cells, iron-mediated-HO-1 activity directly regulates PGF expression and secretion.[84] Thus, we propose HO-1 induction to have a dual effect in the placental response to maternal smoking, both by contributing to oxidative stress detoxification mechanisms and by modulating increased STB pro-angiogenic *PGF* gene expression and PlGF protein secretion. *PGF* is a hub gene in the pro-angiogenesis-associated cluster of upregulated STB tissue genes. This early onset phenomenon could very well modulate adaptive placental angiogenesis seen in smokers later in pregnancy[23] that translates to decreases in placental villous blood flow and increases in blood flow resistance of the umbilical cord. This might lead to impaired oxygen and nutrient transport.

The relevance of CO and PlGF is further supported by the epidemiology of smoking in hypertensive disorders of pregnancy. Maternal smoking constitutes the sole environmental exposure known to reduce the risk of gestational hypertension and PE by up to 50%.[85] PE and gestational hypertension are also associated with abnormally low levels of circulating PlGF compared with those of a healthy pregnancy,[86] while we revealed an upregulation of PlGF expression and protein levels by smoking. Studies have also shown decreased HO gene expression in early pregnancy among women destined to develop PE[87] and decreased exhaled CO among those with gestational hypertension and PE.[88] CO also induces vasorelaxation of placental vessels that decreases perfusion pressure in pregnancy,[89] which may lead to placental insufficiency by decreasing diffusion rates. We further identified several factors that play an important role in the development of PE and were inversely regulated by smoking. The already mentioned STB transition gene KISS1 (upregulated by smoking) shows lower second-trimester circulating levels in women who later developed PE.[90] Endoglin, a transmembrane co-receptor of transforming growth factor β, was downregulated at the protein level by smoking in the STB and is described as an elevated anti-angiogenic factor involved in the development of PE.[91]

Additionally, while we detected elevated ADM expression by smoking, circulating and placental ADM mRNA were reported to be significantly reduced in women 10–12 weeks prior to PE onset.[92] A recent mouse model confirmed this finding by rescuing the PE-like phenotype with nanoparticle-based forced ADM expression, and suggested this as a possible intervention for PE.[39] Altogether, this supports a future focus on the CO-HO-mediated trophoblast effects in the placenta to further understand PE and its largely unknown etiology to identify new therapeutic targets.

Smoking is known to exhibit dose-dependent effects across multiple organs.[93] In this study, dose-response analyses were precluded by procedure-mandated smoking abstinence and self-reported compliance variability, both of which may bias cotinine measurements. Additional prospective studies with pre-procedure biomarker collection are needed to establish quantitative exposure-response relationships between maternal smoking and findings described herein.

Overall, our work describes how the *in vivo* tissue molecular landscape of the developing human placenta responds to heavy smoking in pregnancy. Smoking primarily affects the STB trophoblast syncytium and HBC, tissue-resident placental macrophages, at the transcriptomic and proteomic levels. Dysregulation at the transcriptomic and proteomic levels in STB includes increases in oxidative stress, activation of the xenobiotic detoxification aryl-AhR pathway, and disturbed mitochondrial energy metabolism capacity. The blood clotting cascade and HO system emerged as crucial players in oxidative stress response and angiogenesis. Similar findings were observed for the HBC. Oxidative stress led to an induction of inflammation and protein translation machinery. These early molecular dysregulations have the potential to be used as a model for the manifestation of placental insufficiency that could underpin FGR. In turn, giving way to explore diagnostic and therapeutic strategies to identify and mitigate identified mechanisms early in pregnancy to protect fetal and maternal health in pregnancy and thereby cardiovascular health later in life.

RESOURCE AVAILABILITY

Lead contact

Further information and requests for resources and reagents should be directed to and will be fulfilled by the lead contact, Florian Herse (florian.herse@charite.de).

Materials availability

This study did not generate new materials.

Data and code availability

- Anonymized raw transcriptomic and proteomic data have been uploaded to GEO and PRIDE, under accession numbers GEO: GSE304028 and PRIDE: PXD066340, respectively. They are publicly available as of the

Please cite this article in press as: Valdes et al., Maternal smoking in early pregnancy disrupts placental function through syncytiotrophoblast and macrophage dysregulation, Cell Systems (2026), https://doi.org/10.1016/j.cels.2026.101785

date of publication. The accession numbers are also listed in the key resources table.

- All original code used in this work and needed to reproduce analyses and visualizations has been deposited at Zenodo and is publicly available as of the date of publication under https://doi.org/10.5281/zenodo.23043199. DOIs are also listed in the key resources table.
- Any additional information required to reanalyze the data reported in this paper is available from the lead contact upon request.

ACKNOWLEDGMENTS

We gratefully appreciate the excellent technical assistance of May-Britt Köhler, Gabriele N'Diaye, Jana Czychi, Kornelia Buttke, Aylina Deter (ECRC, MDC, Charité, Berlin), and Lena Neuper (Med. Uni. Graz). We also thank Dr. Andreas Glasner (Femina-Med) for the patient recruitment of first-trimester placental material. F.H., D.S.V., and D.N.M. were supported by Deutsche Forschungsgemeinschaft (HE6249/5-1, HE6249/7-1, HE6249/7-2, HE6249/5-3, and project ID 437531118—SFB 1470) and BIH Omics platform. F.H. was funded by VolkswagenStiftung (9D289). D.N.M. was supported by grants from the German Centre for Cardiovascular Research (DZHK; 81X2100189 and 81Z0100114). M.G. was supported by the Austrian Science Fund (FWF): 10.55776/P35118, 10.55776/I6907, and 10.55776/PAT4258724. O.N. is a participant in the BIH Charité Junior Clinician Scientist Program, funded by the Charité—Universitätsmedizin Berlin, and the Berlin Institute of Health at Charité (BIH). O.N. was supported through the PhD program Inflammatory Disorders in Pregnancy (DP-IDP) by the Austrian Science Fund (FWF): Doc 31-B26, through the PhD program Molecular Medicine at the Medical University of Graz, and by the Marietta Blau Grant (OeAD and BMBWF), EASI Genomics (PID 15215), DGPGM Forschungsstipendium 202, Junior Clinician Scientist of the Berlin Institute of Health (BIH), and with grants from the MeFo Graz (PS-Stipendium 2019/2020). J.N. and F.C. acknowledge funding support from the Federal Ministry of Education and Research (BMBF), as part of the National Research Initiatives for Mass Spectrometry in Systems Medicine, under grant agreement no. 161L0222. F.C. received funding from the European Research Council (ERC) under the European Union's Horizon 2020 research and innovation program (grant agreement no. 101115681) and support from the ERC (ERC starting grant). Schematic drawings were created with BioRender.com.

AUTHOR CONTRIBUTIONS

Conceptualization, D.S.V., F.H., M.G., and O.N.; resources, M.G., S.H., B.O.-P., and D.S.V.; experiments, D.S.V., J.U., D.F., M.R., J.N., F.H., and D.F.; data analysis, D.S.V., M.R., J.N. M.P., F.C., and F.H.; figures, D.S.V. and F.H.; supervision, F.H., D.N.M., R.D., M.G., F.C., M.P., and D.S.V.; funding acquisition, F. H., M.G., O.N., F.C., and D.N.M.; writing of the original draft, D.S.V. and F.H. All authors reviewed and edited the manuscript.

DECLARATION OF INTERESTS

The authors declare no competing interests.

STAR★METHODS

Detailed methods are provided in the online version of this paper and include the following:

- KEY RESOURCES TABLE
- EXPERIMENTAL MODEL AND STUDY PARTICIPANT DETAILS
  - First trimester placenta tissue sourcing
- METHOD DETAILS
  - Sample processing
- QUANTIFICATION AND STATISTICAL ANALYSIS
  - snRNAseq
  - Proteomics
  - Visualizations

SUPPLEMENTAL INFORMATION

Supplemental information can be found online at https://doi.org/10.1016/j.cels.2026.101785.

Received: August 29, 2025
Revised: April 24, 2026
Accepted: November 3, 2026

REFERENCES

1. Aplin, J.D., Myers, J.E., Timms, K., and Westwood, M. (2020). Tracking placental development in health and disease. Nat. Rev. Endocrinol. *16*, 479–494. https://doi.org/10.1038/s41574-020-0372-6.
2. Ballasy, N., Apantaku, I., Dean, W., and Hemberger, M. (2025). Off to a good start: The importance of the placental exchange surface - Lessons from the mouse. Dev. Biol. *517*, 248–264. https://doi.org/10.1016/j.ydbio.2024.10.009.
3. Arima, Y., and Fukuoka, H. (2020). Developmental origins of health and disease theory in cardiology. J. Cardiol. *76*, 14–17. https://doi.org/10.1016/j.jjcc.2020.02.003.
4. Turco, M.Y., and Moffett, A. (2019). Development of the human placenta. Development *146*, dev163428. https://doi.org/10.1242/dev.163428.
5. Carter, A.M. (2000). Placental Oxygen Consumption. Part I: In Vivo Studies—A Review. Placenta *21*, S31–S37. https://doi.org/10.1053/plac.1999.0513.
6. Costa, M.A. (2016). The endocrine function of human placenta: an overview. Reprod. Biomed. Online *32*, 14–43. https://doi.org/10.1016/j.rbmo.2015.10.005.
7. Rana, S., Powe, C.E., Salahuddin, S., Verlohren, S., Perschel, F.H., Levine, R.J., Lim, K.-H., Wenger, J.B., Thadhani, R., and Karumanchi, S.A. (2012). Angiogenic factors and the risk of adverse outcomes in women with suspected preeclampsia. Circulation *125*, 911–919. https://doi.org/10.1161/CIRCULATIONAHA.111.054361.
8. Demir, R., Seval, Y., and Huppertz, B. (2007). Vasculogenesis and angiogenesis in the early human placenta. Acta Histochem. *109*, 257–265. https://doi.org/10.1016/j.acthis.2007.02.008.
9. Burton, G.J., and Jauniaux, E. (2018). Pathophysiology of placental-derived fetal growth restriction. Am. J. Obstet. Gynecol. *218*, S745–S761. https://doi.org/10.1016/j.ajog.2017.11.577.
10. Brosens, I., Pijnenborg, R., Vercruysse, L., and Romero, R. (2011). The "Great Obstetrical Syndromes" are associated with disorders of deep placentation. Am. J. Obstet. Gynecol. *204*, 193–201. https://doi.org/10.1016/j.ajog.2010.08.009.
11. Pels, A., Beune, I.M., van Wassenaer-Leemhuis, A.G., Limpens, J., and Ganzevoort, W. (2020). Early-onset fetal growth restriction: A systematic review on mortality and morbidity. Acta Obstet. Gynecol. Scand. *99*, 153–166. https://doi.org/10.1111/aogs.13702.
12. Rodríguez-Rodríguez, P., Ramiro-Cortijo, D., Reyes-Hernández, C.G., López De Pablo, A.L., González, M.C., and Arribas, S.M. (2018). Implication of Oxidative Stress in Fetal Programming of Cardiovascular Disease. Front. Physiol. *9*, 602. https://doi.org/10.3389/fphys.2018.00602.
13. Burton, G.J., Fowden, A.L., and Thornburg, K.L. (2016). Placental Origins of Chronic Disease. Physiol. Rev. *96*, 1509–1565. https://doi.org/10.1152/physrev.00029.2015.
14. Lange, S., Probst, C., Rehm, J., and Popova, S. (2018). National, regional, and global prevalence of smoking during pregnancy in the general population: a systematic review and meta-analysis. Lancet Glob. Health *6*, e769–e776. https://doi.org/10.1016/S2214-109X(18)30223-7.
15. Shipton, D., Tappin, D.M., Vadiveloo, T., Crossley, J.A., Aitken, D.A., and Chalmers, J. (2009). Reliability of self reported smoking status by pregnant women for estimating smoking prevalence: a retrospective, cross sectional study. BMJ *339*, b4347. https://doi.org/10.1136/bmj.b4347.

16. Yang, Q., Millard, L.A.C., and Davey Smith, G. (2020). Proxy gene-by-environment Mendelian randomization study confirms a causal effect of maternal smoking on offspring birthweight, but little evidence of long-term influences on offspring health. Int. J. Epidemiol. *49*, 1207–1218. https://doi.org/10.1093/ije/dyz250.

17. Wang, X., Zuckerman, B., Pearson, C., Kaufman, G., Chen, C., Wang, G., Niu, T., Wise, P.H., Bauchner, H., and Xu, X. (2002). Maternal Cigarette Smoking, Metabolic Gene Polymorphism, and Infant Birth Weight. JAMA *287*, 195–202. https://doi.org/10.1001/jama.287.2.195.

18. Hackshaw, A., Rodeck, C., and Boniface, S. (2011). Maternal smoking in pregnancy and birth defects: a systematic review based on 173 687 malformed cases and 11.7 million controls. Hum. Reprod. Update *17*, 589–604. https://doi.org/10.1093/humupd/dmr022.

19. Jaitner, A., Vaudel, M., Tsaneva-Atanasova, K., Njølstad, P.R., Jacobsson, B., Bowden, J., Johansson, S., and Freathy, R.M. (2024). Smoking during pregnancy and its effect on placental weight: a Mendelian randomization study. BMC Pregnancy Childbirth *24*, 238. https://doi.org/10.1186/s12884-024-06431-0.

20. Jauniaux, E., and Burton, G.J. (2007). Morphological and biological effects of maternal exposure to tobacco smoke on the feto-placental unit. Early Hum. Dev. *83*, 699–706. https://doi.org/10.1016/j.earlhumdev.2007.07.016.

21. Ganer Herman, H., Miremberg, H., Nini, N., Feit, H., Schreiber, L., Bar, J., and Kovo, M. (2016). The effects of maternal smoking on pregnancy outcome and placental histopathology lesions. Reprod. Toxicol. *65*, 24–28. https://doi.org/10.1016/j.reprotox.2016.05.022.

22. Mayhew, T.M. (1996). Patterns of villous and intervillous space growth in human placentas from normal and abnormal pregnancies. Eur. J. Obstet. Gynecol. Reprod. Biol. *68*, 75–82. https://doi.org/10.1016/0301-2115(96)02486-4.

23. Pfarrer, C., Macara, L., Leiser, R., and Kingdom, J. (1999). Adaptive angiogenesis in placentas of heavy smokers. Lancet *354*, 303. https://doi.org/10.1016/S0140-6736(99)01676-1.

24. Pintican, D., Poienar, A.A., Strilciuc, S., and Mihu, D. (2019). Effects of maternal smoking on human placental vascularization: A systematic review. Taiwan. J. Obstet. Gynecol. *58*, 454–459. https://doi.org/10.1016/j.tjog.2019.05.004.

25. Walker, N., Filis, P., O'Shaughnessy, P.J., Bellingham, M., and Fowler, P.A. (2019). Nutrient transporter expression in both the placenta and fetal liver are affected by maternal smoking. Placenta *78*, 10–17. https://doi.org/10.1016/j.placenta.2019.02.010.

26. Piasek, M., Blanusa, M., Kostial, K., and Laskey, J.W. (2001). Placental cadmium and progesterone concentrations in cigarette smokers. Reprod. Toxicol. *15*, 673–681. https://doi.org/10.1016/s0890-6238(01)00174-5.

27. Zhu, B.T., Cai, M.X., Spink, D.C., Hussain, M.M., Busch, C.M., Ranzini, A.C., Lai, Y.-L., Lambert, G.H., Thomas, P.E., and Conney, A.H. (2002). Stimulatory effect of cigarette smoking on the 15 alpha-hydroxylation of estradiol by human term placenta. Clin. Pharmacol. Ther. *71*, 311–324. https://doi.org/10.1067/mcp.2002.122500.

28. Bruchova, H., Vasikova, A., Merkerova, M., Milcova, A., Topinka, J., Balascak, I., Pastorkova, A., Sram, R.J., and Brdicka, R. (2010). Effect of Maternal Tobacco Smoke Exposure on the Placental Transcriptome. Placenta *31*, 186–191. https://doi.org/10.1016/j.placenta.2009.12.016.

29. Votavova, H., Dostalova Merkerova, M., Fejglova, K., Vasikova, A., Krejcik, Z., Pastorkova, A., Tabashidze, N., Topinka, J., Veleminsky, M., Sram, R.J., et al. (2011). Transcriptome alterations in maternal and fetal cells induced by tobacco smoke. Placenta *32*, 763–770. https://doi.org/10.1016/j.placenta.2011.06.022.

30. Rothhammer, V., and Quintana, F.J. (2019). The aryl hydrocarbon receptor: an environmental sensor integrating immune responses in health and disease. Nat. Rev. Immunol. *19*, 184–197. https://doi.org/10.1038/s41577-019-0125-8.

31. Mund, A., Coscia, F., Kriston, A., Hollandi, R., Kovács, F., Brunner, A.-D., Migh, E., Schweizer, L., Santos, A., Bzorek, M., et al. (2022). Deep Visual Proteomics defines single-cell identity and heterogeneity. Nat. Biotechnol. *40*, 1231–1240. https://doi.org/10.1038/s41587-022-01302-5.

32. Benowitz, N.L., Bernert, J.T., Foulds, J., Hecht, S.S., Jacob, P., III, Jarvis, M.J., Joseph, A., Oncken, C., and Piper, M.E. (2020). Biochemical Verification of Tobacco Use and Abstinence: 2019 Update. Nicotine Tob. Res. *22*, 1086–1097. https://doi.org/10.1093/ntr/ntz132.

33. Wang, M., Liu, Y., Sun, R., Liu, F., Li, J., Yan, L., Zhang, J., Xie, X., Li, D., Wang, Y., et al. (2024). Single-nucleus multi-omic profiling of human placental syncytiotrophoblasts identifies cellular trajectories during pregnancy. Nat. Genet. *56*, 294–305. https://doi.org/10.1038/s41588-023-01647-w.

34. Thomas, J.R., Naidu, P., Appios, A., and McGovern, N. (2021). The Ontogeny and Function of Placental Macrophages. Front. Immunol. *12*, 771054. https://doi.org/10.3389/fimmu.2021.771054.

35. Gonzalez, T.L., Sun, T., Koeppel, A.F., Lee, B., Wang, E.T., Farber, C.R., Rich, S.S., Sundheimer, L.W., Buttle, R.A., Chen, Y.-D.I., et al. (2018). Sex differences in the late first trimester human placenta transcriptome. Biol. Sex Differ. *9*, 4. https://doi.org/10.1186/s13293-018-0165-y.

36. Olney, K.C., Plaisier, S.B., Phung, T.N., Silasi, M., Perley, L., O'Bryan, J., Ramirez, L., Kliman, H.J., and Wilson, M.A. (2022). Sex differences in early and term placenta are conserved in adult tissues. Biol. Sex Differ. *13*, 74. https://doi.org/10.1186/s13293-022-00470-y.

37. Skinnider, M.A., Squair, J.W., Kathe, C., Anderson, M.A., Gautier, M., Matson, K.J.E., Milano, M., Hutson, T.H., Barraud, Q., Phillips, A.A., et al. (2021). Cell type prioritization in single-cell data. Nat. Biotechnol. *39*, 30–34. https://doi.org/10.1038/s41587-020-0605-1.

38. Hakkola, J., Pasanen, M., Pelkonen, O., Hukkanen, J., Evisalmi, S., Anttila, S., Rane, A., Mäntylä, M., Purkunen, R., Saarikoski, S., et al. (1997). Expression of CYP1B1 in human adult and fetal tissues and differential inducibility of CYP1B1 and CYP1A1 by Ah receptor ligands in human placenta and cultured cells. Carcinogenesis *18*, 391–397. https://doi.org/10.1093/carcin/18.2.391.

39. Zhang, Q., Lee, C.-L., Yang, T., Li, J., Zeng, Q., Liu, X., Liu, Z., Ruan, D., Li, Z., Kan, A.S.Y., et al. (2023). Adrenomedullin has a pivotal role in trophoblast differentiation: A promising nanotechnology-based therapeutic target for early-onset preeclampsia. Sci. Adv. *9*, eadi4777. https://doi.org/10.1126/sciadv.adi4777.

40. Dietrich, B., Haider, S., Meinhardt, G., Pollheimer, J., and Knöfler, M. (2022). WNT and NOTCH signaling in human trophoblast development and differentiation. Cell. Mol. Life Sci. *79*, 292. https://doi.org/10.1007/s00018-022-04285-3.

41. Okae, H., Toh, H., Sato, T., Hiura, H., Takahashi, S., Shirane, K., Kabayama, Y., Suyama, M., Sasaki, H., and Arima, T. (2018). Derivation of Human Trophoblast Stem Cells. Cell Stem Cell *22*, 50–63.e6. https://doi.org/10.1016/j.stem.2017.11.004.

42. Latos, P.A., and Hemberger, M. (2016). From the stem of the placental tree: trophoblast stem cells and their progeny. Development *143*, 3650–3660. https://doi.org/10.1242/dev.133462.

43. Hori, T., Okae, H., Shibata, S., Kobayashi, N., Kobayashi, E.H., Oike, A., Sekiya, A., Arima, T., and Kaji, H. (2024). Trophoblast stem cell-based organoid models of the human placental barrier. Nat. Commun. *15*, 962. https://doi.org/10.1038/s41467-024-45279-y.

44. Turco, M.Y., Gardner, L., Kay, R.G., Hamilton, R.S., Prater, M., Hollinshead, M.S., McWhinnie, A., Esposito, L., Fernando, R., Skelton, H., et al. (2018). Trophoblast organoids as a model for maternal–fetal interactions during human placentation. Nature *564*, 263–267. https://doi.org/10.1038/s41586-018-0753-3.

45. Gellner, C.A., Reynaga, D.D., and Leslie, F.M. (2016). Cigarette smoke extract: A preclinical model of tobacco dependence. Curr. Protoc. Neurosci. *77*, 9.54.1–9.54.10. https://doi.org/10.1002/cpns.14.

46. Saha, S.P., Bhalla, D.K., Whayne, T.F., and Gairola, C. (2007). Cigarette smoke and adverse health effects: An overview of research trends and future needs. Int. J. Angiol. *16*, 77–83. https://doi.org/10.1055/s-0031-1278254.

47. Jaccard, G., Djoko, D.T., Korneliou, A., Stabbert, R., Belushkin, M., and Esposito, M. (2019). Mainstream smoke constituents and in vitro toxicity comparative analysis of 3R4F and 1R6F reference cigarettes. Toxicol. Rep. *6*, 222–231. https://doi.org/10.1016/j.toxrep.2019.02.009.

Please cite this article in press as: Valdes et al., Maternal smoking in early pregnancy disrupts placental function through syncytiotrophoblast and macrophage dysregulation, Cell Systems (2026), https://doi.org/10.1016/j.cels.2026.101785

48. Gellner, C.A., Reynaga, D.D., and Leslie, F.M. (2016). Cigarette Smoke Extract: A preclinical model of tobacco dependence. Curr. Protoc. Neurosci. *77*, 9.54.1–9.54.10. https://doi.org/10.1002/cpns.14.

49. Nimo, J., Fritzsche, S., Valdes, D.S., Trinh, M., Pentimalli, T., Klingeberg, M., Schallenberg, S., Klauschen, F., Herse, F., Florian, S., et al. (2026). OpenDVP: An experimental and computational framework for community-empowered deep visual proteomics. Nat. Meth. *23*, 2250–2262. https://doi.org/10.1038/s41592-026-03262-z.

50. Lee, H.-J., Jeong, S.-K., Na, K., Lee, M.J., Lee, S.H., Lim, J.-S., Cha, H.-J., Cho, J.-Y., Kwon, J.-Y., Kim, H., et al. (2013). Comprehensive genome-wide proteomic analysis of human placental tissue for the Chromosome-Centric Human Proteome Project. J. Proteome Res. *12*, 2458–2466. https://doi.org/10.1021/pr301040g.

51. Jin, S., Guerrero-Juarez, C.F., Zhang, L., Chang, I., Ramos, R., Kuan, C.-H., Myung, P., Plikus, M.V., and Nie, Q. (2021). Inference and analysis of cell-cell communication using CellChat. Nat. Commun. *12*, 1088. https://doi.org/10.1038/s41467-021-21246-9.

52. Robinson, N.J., Baker, P.N., Jones, C.J.P., and Aplin, J.D. (2007). A Role for Tissue Transglutaminase in Stabilization of Membrane-Cytoskeletal Particles Shed from the Human Placenta. Biol. Reprod. *77*, 648–657. https://doi.org/10.1095/biolreprod.107.061747.

53. Aplin, J.D., Jones, C.J.P., and Harris, L.K. (2009). Adhesion Molecules in Human Trophoblast – A Review. I. Villous Trophoblast. Placenta *30*, 293–298. https://doi.org/10.1016/j.placenta.2008.12.001.

54. Denhardt, D.T., Noda, M., O'Regan, A.W., Pavlin, D., and Berman, J.S. (2001). Osteopontin as a means to cope with environmental insults: regulation of inflammation, tissue remodeling, and cell survival. J. Clin. Investig. *107*, 1055–1061. https://doi.org/10.1172/JCI12980.

55. Moser, G., Guettler, J., Forstner, D., and Gauster, M. (2019). Maternal Platelets—Friend or Foe of the Human Placenta? Int. J. Mol. Sci. *20*, 5639. https://doi.org/10.3390/ijms20225639.

56. Burton, G.J., and Fowden, A.L. (2015). The placenta: a multifaceted, transient organ. Philos. Trans. R. Soc. Lond. B Biol. Sci. *370*, 20140066. https://doi.org/10.1098/rstb.2014.0066.

57. Thomas, J.R., Appios, A., Zhao, X., Dutkiewicz, R., Donde, M., Lee, C.Y.C., Naidu, P., Lee, C., Cerveira, J., Liu, B., et al. (2021). Phenotypic and functional characterization of first-trimester human placental macrophages, Hofbauer cells. J. Exp. Med. *218*, e20200891. https://doi.org/10.1084/jem.20200891.

58. Hoch, D., Majali-Martinez, A., Bankoglu, E.E., Stopper, H., Glasner, A., Desoye, G., Gauster, M., and Hiden, U. (2023). Maternal Smoking in the First Trimester and its Consequence on the Early Placenta. Lab. Invest. *103*, 100059. https://doi.org/10.1016/j.labinv.2022.100059.

59. Sbrana, E., Suter, M.A., Abramovici, A.R., Hawkins, H.K., Moss, J.E., Patterson, L., Shope, C., and Aagaard-Tillery, K. (2011). Maternal tobacco use is associated with increased markers of oxidative stress in the placenta. Am. J. Obstet. Gynecol. *205*, 246.e1–246.e7. https://doi.org/10.1016/j.ajog.2011.06.023.

60. Ben Amara, A., Gorvel, L., Baulan, K., Derain-Court, J., Buffat, C., Vérollet, C., Textoris, J., Ghigo, E., Bretelle, F., Maridonneau-Parini, I., et al. (2013). Placental Macrophages Are Impaired in Chorioamnionitis, an Infectious Pathology of the Placenta. J. Immunol. *191*, 5501–5514. https://doi.org/10.4049/jimmunol.1300988.

61. Brien, M.-E., Duval, C., Palacios, J., Boufaied, I., Hudon-Thibeault, A.-A., Nadeau-Vallée, M., Vaillancourt, C., Sibley, C.P., Abrahams, V.M., Jones, R.L., et al. (2017). Uric Acid Crystals Induce Placental Inflammation and Alter Trophoblast Function via an IL-1–Dependent Pathway: Implications for Fetal Growth Restriction. J. Immunol. *198*, 443–451. https://doi.org/10.4049/jimmunol.1601179.

62. Bezemer, R.E., Faas, M.M., van Goor, H., Gordijn, S.J., and Prins, J.R. (2024). Decidual macrophages and Hofbauer cells in fetal growth restriction. Front. Immunol. *15*, 1379537. https://doi.org/10.3389/fimmu.2024.1379537.

63. Cardenas, A., Lutz, S.M., Everson, T.M., Perron, P., Bouchard, L., and Hivert, M.-F. (2019). Mediation by Placental DNA Methylation of the Association of Prenatal Maternal Smoking and Birth Weight. Am. J. Epidemiol. *188*, 1878–1886. https://doi.org/10.1093/aje/kwz184.

64. Shen, J., Chen, X., Fang, R., Cai, R., Wang, Y., and Zheng, J. (2026). Causal relationship between 91 inflammatory factors and fetal growth restriction: a bidirectional Mendelian randomization study. J. Matern. Fetal Neonatal Med. *39*, 2630530. https://doi.org/10.1080/14767058.2026.2630530.

65. Sun, Y., Lin, H., Zhu, W., Niu, L., Li, Y., Huang, Y., and Chang, Q. (2026). A FOS/NFKB1-associated Hofbauer cell subset mediates placental niche dysregulation in early-onset fetal growth restriction. Front. Cell Dev. Biol. *14*, 1827600. https://doi.org/10.3389/fcell.2026.1827600.

66. Aycicek, A., Varma, M., Ahmet, K., Abdurrahim, K., and Erel, O. (2011). Maternal active or passive smoking causes oxidative stress in placental tissue. Eur. J. Pediatr. *170*, 645–651. https://doi.org/10.1007/s00431-010-1338-9.

67. Qanungo, S., Sen, A., and Mukherjea, M. (1999). Antioxidant status and lipid peroxidation in human feto-placental unit. Clin. Chim. Acta *285*, 1–12. https://doi.org/10.1016/S0009-8981(99)00051-0.

68. Suter, M., Abramovici, A., Showalter, L., Hu, M., Shope, C.D., Varner, M., and Aagaard-Tillery, K. (2010). In utero tobacco exposure epigenetically modifies placental CYP1A1 expression. Metabolism *59*, 1481–1490. https://doi.org/10.1016/j.metabol.2010.01.013.

69. Postal, B.G., Ghezzal, S., Aguanno, D., André, S., Garbin, K., Genser, L., Brot-Laroche, E., Poitou, C., Soula, H., Leturque, A., et al. (2020). AhR activation defends gut barrier integrity against damage occurring in obesity. Mol. Metab. *39*, 101007. https://doi.org/10.1016/j.molmet.2020.101007.

70. Qiao, J., Arthur, J.F., Gardiner, E.E., Andrews, R.K., Zeng, L., and Xu, K. (2018). Regulation of platelet activation and thrombus formation by reactive oxygen species. Redox Biol. *14*, 126–130. https://doi.org/10.1016/j.redox.2017.08.021.

71. Frank, H.-G. (2011). Placental Development. In Fetal and Neonatal Physiology, Fourth Edition, R.A. Polin, W.W. Fox, and S.H. Abman, eds. (W.B. Saunders), pp. 108–120. https://doi.org/10.1016/B978-1-4160-3479-7.10011-4.

72. Devisme, L., Chauvière, C., Franquet-Ansart, H., Chudzinski, A., Stichelbout, M., Houfflin-Debarge, V., and Subtil, D. (2017). Perinatal outcome of placental massive perivillous fibrin deposition: a case–control study. Prenat. Diagn. *37*, 323–328. https://doi.org/10.1002/pd.5013.

73. Uxa, R., Baczyk, D., Kingdom, J.C.P., Viero, S., Casper, R., and Keating, S. (2010). Genetic Polymorphisms in the Fibrinolytic System of Placentas with Massive Perivillous Fibrin Deposition. Placenta *31*, 499–505. https://doi.org/10.1016/j.placenta.2010.03.013.

74. Strauss, J.F., Kido, S., Sayegh, R., Sakuragi, N., and Gåfvels, M.E. (1992). The cAMP signalling system and human trophoblast function. Placenta *13*, 389–403. https://doi.org/10.1016/0143-4004(92)90047-w.

75. Shi, Q.J., Lei, Z.M., Rao, C.V., and Lin, J. (1993). Novel role of human chorionic gonadotropin in differentiation of human cytotrophoblasts. Endocrinology *132*, 1387–1395. https://doi.org/10.1210/endo.132.3.7679981.

76. Pidoux, G., Gerbaud, P., Tsatsaris, V., Marpeau, O., Ferreira, F., Meduri, G., Guibourdenche, J., Badet, J., Evain-Brion, D., and Frendo, J.-L. (2007). Biochemical characterization and modulation of LH/CG-receptor during human trophoblast differentiation. J. Cell. Physiol. *212*, 26–35. https://doi.org/10.1002/jcp.20995.

77. Pidoux, G., Gerbaud, P., Dompierre, J., Lygren, B., Solstad, T., Evain-Brion, D., and Taskén, K. (2014). A PKA–ezrin–Cx43 signaling complex controls gap junction communication and thereby trophoblast cell fusion. J. Cell Sci. *127*, 4172–4185. https://doi.org/10.1242/jcs.149609.

78. Sukhbaatar, U., Kanasaki, H., Mijiddorj, T., Oride, A., and Miyazaki, K. (2013). Kisspeptin induces expression of gonadotropin-releasing hormone receptor in GnRH-producing GT1–7 cells overexpressing G protein-coupled receptor 54. Gen. Comp. Endocrinol. *194*, 94–101. https://doi.org/10.1016/j.ygcen.2013.09.002.

79. Sassone-Corsi, P. (2012). The Cyclic AMP Pathway. Cold Spring Harb. Perspect. Biol. *4*, a011148. https://doi.org/10.1101/cshperspect.a011148.

Please cite this article in press as: Valdes et al., Maternal smoking in early pregnancy disrupts placental function through syncytiotrophoblast and macrophage dysregulation, Cell Systems (2026), https://doi.org/10.1016/j.cels.2026.101785

80. Dunaway, L.S., Loeb, S.A., Petrillo, S., Tolosano, E., and Isakson, B.E. (2024). Heme metabolism in nonerythroid cells. J. Biol. Chem. *300*, 107132. https://doi.org/10.1016/j.jbc.2024.107132.

81. Coburn, R.F., Blakemore, W.S., and Forster, R.E. (1963). Endogenous carbon monoxide production in man. J. Clin. Investig. *42*, 1172–1178. https://doi.org/10.1172/JCI104802.

82. Zenclussen, M.L., Linzke, N., Schumacher, A., Fest, S., Meyer, N., Casalis, P.A., and Zenclussen, A.C. (2015). Heme oxygenase-1 is critically involved in placentation, spiral artery remodeling, and blood pressure regulation during murine pregnancy. Front. Pharmacol. *5*, 291. https://doi.org/10.3389/fphar.2014.00291.

83. Dickson, M.A., Peterson, N., McRae, K.E., Pudwell, J., Tayade, C., and Smith, G.N. (2020). Carbon monoxide increases utero-placental angiogenesis without impacting pregnancy specific adaptations in mice. Reprod. Biol. Endocrinol. *18*, 49. https://doi.org/10.1186/s12958-020-00594-z.

84. Rashdan, N.A., Zhai, B., and Lovern, P.C. (2021). Fluid shear stress regulates placental growth factor expression via heme oxygenase 1 and iron. Sci. Rep. *11*, 14912. https://doi.org/10.1038/s41598-021-94559-w.

85. Wei, J., Liu, C.-X., Gong, T.-T., Wu, Q.-J., and Wu, L. (2015). Cigarette smoking during pregnancy and preeclampsia risk: a systematic review and meta-analysis of prospective studies. Oncotarget *6*, 43667–43678. https://doi.org/10.18632/oncotarget.6190.

86. Chau, K., Hennessy, A., and Makris, A. (2017). Placental growth factor and pre-eclampsia. J. Hum. Hypertens. *31*, 782–786. https://doi.org/10.1038/jhh.2017.61.

87. Farina, A., Sekizawa, A., De Sanctis, P., Purwosunu, Y., Okai, T., Cha, D.H., Kang, J.H., Vicenzi, C., Tempesta, A., Wibowo, N., et al. (2008). Gene expression in chorionic villous samples at 11 weeks' gestation from women destined to develop preeclampsia. Prenat. Diagn. *28*, 956–961. https://doi.org/10.1002/pd.2109.

88. Kreiser, D., Baum, M., Seidman, D.S., Fanaroff, A., Shah, D., Hendler, I., Stevenson, D.K., Schiff, E., and Druzin, M.L. (2004). End tidal carbon monoxide levels are lower in women with gestational hypertension and preeclampsia. J. Perinatol. *24*, 213–217. https://doi.org/10.1038/sj.jp.7211062.

89. Bainbridge, S.A., Farley, A.E., McLaughlin, B.E., Graham, C.H., Marks, G.S., Nakatsu, K., Brien, J.F., and Smith, G.N. (2002). Carbon Monoxide Decreases Perfusion Pressure in Isolated Human Placenta. Placenta *23*, 563–569. https://doi.org/10.1053/plac.2002.0845.

90. Armstrong, R.A., Reynolds, R.M., Leask, R., Shearing, C.H., Calder, A.A., and Riley, S.C. (2009). Decreased serum levels of kisspeptin in early pregnancy are associated with intra-uterine growth restriction and pre-eclampsia. Prenat. Diagn. *29*, 982–985. https://doi.org/10.1002/pd.2328.

91. Venkatesha, S., Toporsian, M., Lam, C., Hanai, J., Mammoto, T., Kim, Y.M., Bdolah, Y., Lim, K.-H., Yuan, H.-T., Libermann, T.A., et al. (2006). Soluble endoglin contributes to the pathogenesis of preeclampsia. Nat. Med. *12*, 642–649. https://doi.org/10.1038/nm1429.

92. Whigham, C.-A., MacDonald, T.M., Walker, S.P., Pritchard, N., Hannan, N.J., Hastie, R., Alwis, N.D., Cannon, P., Nguyen, T.V., Tong, S., et al. (2019). Circulating adrenomedullin mRNA is decreased in women destined to develop term preeclampsia. Pregnancy Hypertens. *16*, 16–25. https://doi.org/10.1016/j.preghy.2019.02.003.

93. Dai, X., Gil, G.F., Reitsma, M.B., Ahmad, N.S., Anderson, J.A., Bisignano, C., Carr, S., Feldman, R., Hay, S.I., He, J., et al. (2022). Health effects associated with smoking: a Burden of Proof study. Nat. Med. *28*, 2045–2055. https://doi.org/10.1038/s41591-022-01978-x.

94. Krishnaswami, S.R., Grindberg, R.V., Novotny, M., Venepally, P., Lacar, B., Bhutani, K., Linker, S.B., Pham, S., Erwin, J.A., Miller, J.A., et al. (2016). Using single nuclei for RNA-seq to capture the transcriptome of postmortem neurons. Nat. Protoc. *11*, 499–524. https://doi.org/10.1038/nprot.2016.015.

95. Haider, S., Meinhardt, G., Saleh, L., Kunihs, V., Gamperl, M., Kaindl, U., Ellinger, A., Burkard, T.R., Fiala, C., Pollheimer, J., et al. (2018). Self-renewing trophoblast organoids recapitulate the developmental program of the early human placenta. Stem Cell Rep. *11*, 537–551. https://doi.org/10.1016/j.stemcr.2018.07.004.

96. Murray, P.J., Allen, J.E., Biswas, S.K., Fisher, E.A., Gilroy, D.W., Goerdt, S., Gordon, S., Hamilton, J.A., Ivashkiv, L.B., Lawrence, T., et al. (2014). Macrophage Activation and Polarization: Nomenclature and Experimental Guidelines. Immunity *41*, 14–20. https://doi.org/10.1016/j.immuni.2014.06.008.

97. Shin, H.-S., Kim, J.-G., Shin, Y.-J., and Jee, S.H. (2002). Sensitive and simple method for the determination of nicotine and cotinine in human urine, plasma and saliva by gas chromatography–mass spectrometry. J. Chromatogr. B Analyt. Technol. Biomed. Life Sci. *769*, 177–183. https://doi.org/10.1016/S1570-0232(02)00007-7.

98. Meier, F., Brunner, A.-D., Frank, M., Ha, A., Bludau, I., Voytik, E., Kaspar-Schoenefeld, S., Lubeck, M., Raether, O., Bache, N., et al. (2020). diaPASEF: parallel accumulation–serial fragmentation combined with data-independent acquisition. Nat. Methods *17*, 1229–1236. https://doi.org/10.1038/s41592-020-00998-0.

99. Chen, H., Albergante, L., Hsu, J.Y., Lareau, C.A., Lo Bosco, G., Guan, J., Zhou, S., Gorban, A.N., Bauer, D.E., Aryee, M.J., et al. (2019). Single-cell trajectories reconstruction, exploration and mapping of omics data with STREAM. Nat. Commun. *10*, 1903. https://doi.org/10.1038/s41467-019-09670-4.

Please cite this article in press as: Valdes et al., Maternal smoking in early pregnancy disrupts placental function through syncytiotrophoblast and macrophage dysregulation, Cell Systems (2026), https://doi.org/10.1016/j.cels.2026.101785

STAR★METHODS

KEY RESOURCES TABLE

REAGENT or RESOURCE	SOURCE	IDENTIFIER
Antibodies		
Human anti-human CD163-PE (REA1309)	Miltenyi	130-127908
Mouse anti-human CD31 (JC70A)	Dako	M0823; RRID: AB_2114471
Rabbit anti-human E-cadherin / CDH1 (24E10)	Cell Signaling	3195; RRID: AB_2291471
Mouse anti-human E-cadherin / CDH1 (4A2)	Cell Signaling	14472; RRID: AB_2728770
Mouse anti-human HLA-G (MEM-G/1)	ExBio	11-291-C100; RRID: AB_10734353
Rabbit anti-human OGDH	Sigma	HPA020347; RRID: AB_1854773
Mouse anti-human Fibrin (59D7)	Merck	MABS2155; RRID: AB_2893306
Rabbit anti-human CD42b	Proteintech	12860-1-AP
Biological samples		
Primary human tissue and blood samples	Gauster Lab, Medical University of Vienna	N/A
Chemicals, peptides, and recombinant proteins		
2-Mercaptoethanol 50mM	Gibco	31350-010
50mL glass syringe	Socorex	155.0550
A83-01	StemCellTechnologies	72022
Acetonitril (ACN), LC/MS grade	VWR Chemicals	83640.290
Advanced DMEM/F12 with Glutamax	Gibco	31331-093
Benzonase nuclease	Merck	E1014-5KU
Bovine Serum Albumin (BSA) Fraction V	Carl Roth	1ETA.4
C18 Evotips (EV2013, Evotip Pure)	Evosep	EV2013
Cell banker 2, freezing medium	AMSBIO	11914
CHIR99021	Tocris	4423
Chloroacetamide (CAA) powder	Sigma-Aldrich	C0267
Collagen IV from human placenta	Sigma-Aldrich	C5533-5MG
DAPI (4′,6-Diamidin-2-phenylindol, Dihydrochlorid) nuclear stain	Invitrogen	D1306
Dimethyl sulfoxide (DMSO), sterile filtered	Sigma-Aldrich	D2438-50ML
Dithiothreitol (DTT) powder	Sigma-Aldrich	10197777001
DNAse I	Roche Diagnostics	10104159001
Dounce homogenizer 1mL	Wheaton	357538
Erythrocyte lysis buffer 1X	PAN-Biotech	P10-90500
Ethylenediaminetetraacetic acid (EDTA)	Sigma-Aldrich	E7889-100ML
Fast SYBR Green Master Mix	Thermo Fisher Scientific	4385614
Fetal Bovine Serum, sterile filtered	PAN-Biotech	P30-3306
Formic acid (FA)	Merck Millipore	1.00264.1000
Forskolin	Tocris	1099/50
Gentamycin 10mg/mL	Sigma-Aldrich	15710-049
Glucose solution 200g/L	Gibco	A2494001
Halt protease inhibitor cocktail 100X (incl. 0.5M EDTA solution)	Thermo Fisher Scientific	87786
Hanks balanced salt solution (HBSS)	Stemcell Technologies	37250
High-capacity cDNA reverse transcription kit	Applied Biosystems	4368814
Human epidermal growth factor (hEGF)	R&DSystems	236-EG
Insulin Transferring Selenium Ethanolamine (ITS-X)	Gibco	5150056
L-Glutamine LifeFactor	Lifeline Cell Technology	LS-1013

(*Continued on next page*)

Please cite this article in press as: Valdes et al., Maternal smoking in early pregnancy disrupts placental function through syncytiotrophoblast and macrophage dysregulation, Cell Systems (2026), https://doi.org/10.1016/j.cels.2026.101785

Continued

REAGENT or RESOURCE	SOURCE	IDENTIFIER
Lys-C, MS grade	Promega	VA1170
MS grade ultra-pure water	Chemlab	CL02.0240.2500
Normal goat serum	Thermo Fisher Scientific	16210064
Phosphatase inhibitor cocktail 100X	CellSignaling Technology	5870
Polyphenylene sulfide (PPS) membrane metal frame slides	Leica	11600294
Polypropylene large tubing 8mm ID x 11mm OD, 1.6mm wall thickhness	Cole-Parmer	GZ-50121-60
Polypropylene small tubing 3.2mm ID x 6.4mm OD, 1.6mm wall thickhness	Cole-Parmer	GZ-50106-26
Potassium chloride (KCl) 2M, 0.2µm filtered	Invitrogen	AM9640G
Propidium iodide solution	Sigma-Aldrich	P4864
Protector RNase inhibitor	Roche Diagnostics	03335402001
QIAzol lysis reagent	Qiagen	79306
Reference research cigarette	University of Kentucky	1R6F small batch
RNaseZap	Invitrogen	AM9780
RNeasy Mini Kit	Quiagen	74106
ROCKi (Y27632)	Selleckchem	S1049
Slow Fade Diamong Mounting Medium	Sigma-Aldrich	P5726
Sodium chloride (NaCl) 0.9% solution	Sigma-Aldrich	S8776-100ML
Sodium deoxycholate (SDC) powder	Thermo Fisher Scientific	89904
SpectroStar Nano	BMG Labtech	N/A
Sucrose powder	Carl Roth	4621.2
SUPERase-In RNase inhibitor 20 U/µL	Thermo Fischer Scientific	AM2694
Superfrost Plus adhesion microscope slides	Epredia	J1800AMNZ
TaqMan Fast Universal PCR Mastermix 2X	Thermo Fisher Scientific	4367848
Triethylammonium bicarbonate (TEAB)	Sigma-Aldrich	T7408
Trifluoroacetic acid (TFA)	Sigma-Aldrich	96924-250ML-F
TRIS-HCl (Tris(hydroxymethyl)aminomethan Hydrochlorid) buffer pH 8.5	Ambion	AM985-5G
TRIS-HCl buffer pH 8.0, 0.2µm filtered	Invitrogen	AM9855G
Triton X-100, for molecular biology	Sigma-Aldrich	T8787-250
Trypan blue solution 0.4%	Gibco	15250061
TrypLE Express dissociation reagent	Gibco	12604-021
Trypsin Gold, MS grade	Promega	V5280
Tween 20 – molecular grade	CalBiochem	655204
Ultra V Block	Thermo Fisher Scientific	TA-125-UB
UltraPure BSA, RNAse free	Invitrogen	AM2616
Valproic acid (VPA)	Sigma-Aldrich	P4543
VectaShield mounting medium	Vector-Laboratories	H-1000-10
Critical commercial assays		
Chromium single cell 3′ Kits v3.1	10X Genomics	PN-1000268
Cotinine ELISA	R&D Systems	DPG00
QuantStudio 3 Real-Time PCR System	Qiagen	N/A
Placenta growth factor ELISA	Abnova	KA0930
Deposited data		
Single nucleus RNA sequencing data	This paper	GEO: GSE304028
Tissue and cell culture pellet proteomics data	This paper	PRIDE: PXD066340

(*Continued on next page*)

Continued

REAGENT or RESOURCE	SOURCE	IDENTIFIER
Experimental models: Cell lines		
Primary human trophoblast stem cells	Knoefler Lab, Medical University of Vienna	N/A
Experimental models: Organisms/strains		
Primary bone marrow derived macrophages from C57BL/6J mice	Jackson Laboratories	000664
Oligonucleotides		
Primer: Human 18S; Forward: 5′ ACA TCC AAG GAA GGC AGC AG 3′; Reverse: 5′ TTT TCG TCA CTA CCT CCC CG 3′; Probe: 5′ FAM-CGC GCA AAT TAC CCA CTC CCG ACA-TAMRA 3′	Aokin Oligos	N/A
Primer: Human CYP1A1; Forward: 5′-TGG ATG AGA ACG CCA ATG TC 3′; Reverse: 5′-TGG GTT GAC CCA TAG CTT CT 3′; Probe: NA	Aokin Oligos	N/A
Primer: Human CYP1B1; Forward: 5′ TACCGGCCACTATCACTGAC 3′; Reverse: 5′ AAGGAAGGCCAGGACATAGG 3′; Probe: NA	Aokin Oligos	N/A
Primer: Human PGF; Forward: 5′ CCTACGTGGAGCTGACGTTCT 3′; Reverse: 5′ CCTTTCCGGCTTCATCTTCTC 3′ Probe: 5′FAM-TCGCTGCGAATGCCGGCC-TAMRA 3′	Aokin Oligos	N/A
Primer: Human ADM Forward: 5′ CTGATGTACCTGGGTTCGCT 3′ Reverse: 5′ CACGACTCAGAGCCCACTTA 3′ Probe: 5′FAM- AGGCGCTGACACCGCTCGGT-TAMRA 3′	Aokin Oligos	N/A
Primer: Human HMOX1; Forward: 5′ AACTTTCAGAAGGGCCAGGT 3′, Reverse: 5′ GAAGACTGGGCTCTCCTTGT 3′; Probe: 5′FAM- ACCCGAGACGGCTTCAAGCTGGT - TAMRA 3′	Aokin Oligos	N/A
Primer: Human IL-6; Forward: 5′ AGACAGCCACTCACCTCTTC 3′; Reverse: 5′ AGTGCCTCTTTGCTGCTTTC3′; Probe: NA	Aokin Oligos	N/A
Primer: Human ITGB5; Forward: 5′ AGTGCCACCTCATGTGAAGA 3′; Reverse: 5′ GTTTGCCCTCAGATCACACC 3′; Probe: NA	Aokin Oligos	N/A
Primer: Human ICAM1 Forward: 5′- GTGACCGTGAATGTGCTCTC-3′; Reverse: 5′- CCTGCAGTGCCCATTATGAC -3′; Probe: NA	Aokin Oligos	N/A
Primer: Human SPP1; Forward: 5′ GTTTCGCAGACCTGACATCC 3′; Reverse: 5′ CTCCTCGCTTTCCATGTGTG 3′; Probe: NA	Aokin Oligos	N/A
Software and algorithms		
CellRanger	10X Genomics	6.1.2
CellBender	10X Genomics	0.2.2
R	CRAN	4.1.2 and 4.4.3
Python	Python foundation	3.7.0
QuantStudio 3 Real-Time PCR System	Qiagen	N/A
All versions for packages used within R and Python are stated under the ‘Data analysis’	This paper	N/A
Code to reproduce analyses and visualisations	This paper	https://doi.org/10.5281/zenodo.23043199
Processed objects for snRNAseq and spatial proteomics	This paper	https://github.com/danielasofiavaldes-del/Maternal-smoking-in-pregnancy
Anonymized raw snRNAseq data	This paper	GEO under accession number GSE304028

(*Continued on next page*)

Please cite this article in press as: Valdes et al., Maternal smoking in early pregnancy disrupts placental function through syncytiotrophoblast and macrophage dysregulation, Cell Systems (2026), https://doi.org/10.1016/j.cels.2026.101785

Continued

REAGENT or RESOURCE	SOURCE	IDENTIFIER
Anonymized raw spatial and in-vitro proteomics data	This paper	PRIDE under accession number PXD066340
Other		
Agilent 2100 Bioanalyzer	Agilent Technologies	https://www.agilent.com/en/product/automated-electrophoresis/bioanalyzer-systems
BD FACSAria III Cell sorter	BD Biosciences	https://www.bdbiosciences.com/en-se/products/instruments/flow-cytometers/research-cell-sorters/bd-facsaria-iii
AxioScan slide scanner	Carl Zeiss AG	https://www.zeiss.com/microscopy/en/products/imaging-systems/axioscan-7.html
Illumina HiSeq-4000	Illumina	https://support.illumina.com/sequencing/sequencing_instruments/hiseq-4000.html
Leica Microdissector LMD7	Leica	https://www.leica-microsystems.com/products/light-microscopes/p/leica-lmd7/
Thermal cycler	Bio-Rad S1000	https://www.bio-rad.com/en-us/product/s1000-thermal-cycler
EASY-n-LC-1200 HPLC system	ThermoFisher Scientific	https://documents.thermofisher.com/TFS-Assets/CMD/Specification-Sheets/PS-64582-LC-EASY-nLC-1200-PS64582-EN.pdf
timsTOF SCP Mass spectrometer	Bruker Daltonik	https://www.bruker.com/de/products-and-solutions/mass-spectrometry/timstof.html

EXPERIMENTAL MODEL AND STUDY PARTICIPANT DETAILS

First trimester placenta tissue sourcing

Placental tissue was collected surgically from electively terminated pregnancies with informed consent from healthy individuals (gestational age 5 – 11 weeks). Exclusion criteria were maternal age under 18 years, maternal BMI >25 kg/m^2 and any existing maternal pathologies. Ethical approval was obtained from the Medical University of Graz Ethics Committee (31-019 ex 18/19). Immediately after surgical extraction, tissue was stored at 4°C in culture medium (DMEM/F12 1:1, 1 g/dL glucose) and processed in less than 4 hours. Villous tissue was rinsed twice in cold (4°C) 0.9% NaCl solution to remove blood, and either snap frozen in liquid nitrogen and stored at -70°C until processing; or fixed with 10% formalin, paraffin embedded and dehydrated according to standard protocols. Participant characteristics are presented per cohort below and per sample in Table S1. Values were tested for normality via Shapiro-Wilk and Anderson-Darling tests and compared without removing outliers using either two-tailed unpaired Welch's t-test (*) or two-tailed Mann-Whitney U test (§) and are presented as mean ± standard deviation. Cotinine enzyme-linked immunosorbent assay (ELISA) detection level was 1 ng/mL, n.d. not detected.

Characteristics of included study subjects

	Omics cohort			Independent validation cohortmRNAPlacental growth factor (PlGF) ELISA		
Parameter	Non-smokers	Smokers	p	Non-smokers	Smokers	p
Sample size (n)	11	5	-	15; 24	24; 36	-; -
Cotinine (ng/mL)	n.d.	147.2 ± 42.1	0.002*	n.d.; n.d.	147.4 ± 153.5; 105.2 ± 97.0	<0.0001*; <0.0001§
Self-reported cigarettes/day (n participants)	0	15-20 (n=3); 20-30 (n=2)	-	0	1-5 (n = 9); 5-10 (n = 16); 10-20 (n=8); Not specified (n=3)	-
Gestational age (days)	57.8 ± 16.4	60.0 ± 9.4	0.8*	61.8 ± 17.0; 68.7 ± 15.5	59.6 ± 15.4; 6.0 ± 14.5	0.6*; 0.5*
Placental volume (cm2)	1.6 ± 1.6	2.2 ± 1.2	0.5*	3.2 ± 2.4; 5.4 ± 8.9	2.6 ± 1.8; 4.9 ± 6.9	0.4*; 0.7§
Maternal age (years)	28.0 ± 5.3	25.4 ± 4.2	0.4*	34.7 ± 6.9; 32.1 ± 7.7	26.3 ± 6.0; 28.7 ± 6.9	0.002*; 0.09*
Maternal body mass index (BMI, kg/m2)	21.2 ± 2.7	22.4 ± 2.6	0.5*	25.3 ± 3.7; 25.2 ± 5.4	21.9 ± 2.8; 22.3 ± 3.6	0.03*; 0.03§

(*Continued on next page*)

Please cite this article in press as: Valdes et al., Maternal smoking in early pregnancy disrupts placental function through syncytiotrophoblast and macrophage dysregulation, Cell Systems (2026), https://doi.org/10.1016/j.cels.2026.101785

CellPress
OPEN ACCESS

Continued

	Omics cohort			Independent validation cohortmRNAPlacental growth factor (PlGF) ELISA		
Parameter	Non-smokers	Smokers	p	Non-smokers	Smokers	p
Maternal weight (kg)	60.0 ± 10.8	63.8 ± 4.1	0.5*	69.8 ± 10.4; 70.3 ± 15.9	60.8 ± 9.2; 61.7 ± 12.2	0.01*; 0.02§
Maternal height (m)	1.7 ± 0.05	1.7 ± 0.07	0.7*	1.7 ± 0.09; 1.7 ± 0.08	1.7 ± 0.06; 1.7 ± 0.07	0.9*; 0.7*

Data presented as mean ± standard deviation. n.d. not detected, ELISA detection level was 1 ng/mL. Significance between groups evaluated by two-tailed unpaired Welch's t-test (*) or two-tailed unpaired Mann Whitney test (§) depending on dataset normality and indicated with a symbol after the p-value. Additional samples were included in the validation cohort for PlGF ELISA measurement and characteristics noted. BMI, body mass index; PlGF, placental growth factor; ELISA, enzyme-linked immunosorbent assay.

METHOD DETAILS

Sample processing

snRNAseq

Approximately 100-200 mg frozen placental tissue was processed according to an optimised nuclei isolation protocol by Krishnaswami et al.[94] Briefly, frozen tissue was crushed in liquid nitrogen using a frozen mortar and pestle and disrupted with a pre-cooled glass Dounce homogenizer in homogenisation buffer (1X NIM2 [1X protease inhibitor, 1 μM DDT, 250 mM sucrose, 25 mM KCl, 5 mM MgCl2, 10 mM pH8.0 Tris], 0.4 U/μL RNAseInhibitor, 0.2 U/μL SUPERase-in, 0.1% v/v Triton X-100) and filtered through a FACS tube with a 35 μm sieve cap. Homogenate was incubated in the dark, on ice, for two minutes with DAPI (5 μg/μL) and centrifuged for eight minutes (1,000 RCF, 4°C). Pellets were resuspended with staining buffer (3% BSA RNase free + 1% SUPERase-in in DPBS), transferred to a FACS-tube with a 35 μm sieve cap and analysed using the BD FACSAria III cell sorter using the BD FACSDiva software (v6.1.3). After FACS sorting with a 90% viable single nuclei cut-off, nuclei in landing buffer (DPBS with 4% BSA RNAse free + 10% RNAseInhibitor + 10% SUPERase-in) were counted using a digital counting chamber to 400-500 nuclei/μl and loaded onto 10x Genomics Chromium chips. Single-index v3 libraries were prepared according to manufacturer's instructions (Chromium Single Cell 3' Kits v3.1 Dual Index User Guide – CG000315). Libraries were sequenced on an Illumina HiSeq-4000 (pair-ended) with a minimum coverage of 50,000 raw reads per nucleus.

Primary cell culture

Trophoblast stem cells. Villous cytotrophoblasts (vCTBs) were isolated from first trimester human villi according to published protocols.[95] Placental tissue (6th–8th week of gestation) was cut from chorionic membranes, minced into small pieces and digested thrice for 10 min, 15 min and 15min (HBSS, 0.25% Trypsin, 1.25 mg/mL DNAse I; 5mL solution per mL tissue). Each digestion was stopped using 10% FBS [v/v]. Cells were filtered through a 100-μm pore size cell strainer, and cells from the second and third digestions were pooled. Cells were loaded onto Percoll gradients (10 – 70 % [v/v]) and vCTBs were collected between 35 – 50 % of Percoll layers, pelleted, and washed twice with HBSS. Red blood cells were removed by incubating with erythrocyte lysis buffer (155 mM NH_4Cl, 10 mM $KHCO_3$, 0.2 mM EDTA, pH 7.3) at RT for 5 min. vCTBs were washed twice with HBSS and seeded at a density of 0.5 x 10^6 cells per well of a 6w plate pre-coated with 5 μg/mL collagen IV. Cells were cultured with 2mL/well of published trophoblast stem cell (TSC) media[41] at 37°C and 5% CO_2, media was replaced every second day.[14] When reaching 70-80% confluency cells were enzymatically dissociated with 1mL TrypLE for 10 minutes at 37°C and passaged at a 1:2 ratio. Following the 10th passage, only proliferative cells with a TSC phenotype remain, which were passaged as above at a 1:3 split ratio every three days and used for differentiation and stimulation experiments between passages 15 and 25. Cells were frozen in cell banker 2 (2 – 5 x 10^6 cells per mL) for cryogenic storage.

Following 24 hours attachment in TSC medium, TSCs were stimulated with CSE diluted 1:200 in supplemented medium for up to 24 hours. At the hour (h) timepoints 3 h, 6 h, 9 h, 12 h and 24 h, 700 μL QIAzol reagent was added directly to each well and frozen at -70°C prior to RNA isolation and cDNA synthesis. To differentiate towards the STB lineage, TSCs were harvested upon reaching ~80 % confluency with TrypLE for 10 minutes at 37°C and seeded at a density of 0.1 x 10^6 cells per well of 12w plate pre-coated with 2.5 μg/mL collagen IV. After attachment for 24 hours, cells were cultured in 1mL STB medium. Medium was replaced daily for the first four days. On day 6, cells were stimulated for 6 hours with CSE 1:200 in STB medium and 700 μL QIAzol reagent was added directly to the wells and frozen at -70°C prior to RNA isolation and cDNA synthesis. Methods for the STB differentiation and processing of pellets analyzed by LC-MS are outlined in the proteomics section below (section 3.2.6).

Mouse macrophages. Nomenclature and experimental design of *in vitro* differentiated and activated macrophages follows the guidelines described by Murray et al.[96]

Bone marrow derived macrophages (BMDM) were isolated from the femur and tibia of freshly euthanized C57BL/6J mice, by flushing with 40 ml of activation media: DMEM containing L-glutamine, 10% FCS, 10 mM HEPES, 50 μM β-ME plus 10 ml L929 conditioned media. Cells were then pelleted, and resuspended into monocyte differentiation media: DMEM (Gibco), 10 % (v/v) FCS, 5% (v/v) adult horse serum (Cell Concepts), 1:100 non-essential amino acids (Sigma), 50 μM β-ME (Sigma), with 20% (v/v) L929 conditioned DMEM media. For macrophage differentiation, 10 x 10^6 BMDM were cultivated in 50 ml of differentiation media for 10 d in sealed, hydrophobic Teflon® bags (FT FEP 100 C (DuPont), American Durafilm) at 37°C and 10% CO_2. The yield of BMD

M(-) macrophages (also known as M0) from one bag was consistently ~70-100 x 10^6 cells with a purity of >95% (determined as F4/80+ CD11b+ cells by flow cytometry, data not shown). For activation of M(-) into M(IL-4 and IL-13) (also known as M2), BMD M(-) cells were harvested from Teflon bags, pelleted and resuspended into activation media containing recombinant mouse IL-4 (10 ng/mL) and IL-13 (10 ng/ml) or LPS (100ng/ml). For analysis by real-time RT-PCR and MS, 1 x 10^6 BMD M(-) and BMD M(IL-13) cells were plated per well in 12-well plates. In all cases, the macrophages were first allowed to rest and adhere for 3 h. Unless otherwise noted, cells were activated for 24 h at 37°C and 5% CO_2.

Trophoblast culture medium recipes used for primary *in-vitro* culture work

Cell type	Culture medium
Trophoblast stem cell (TSC)	DMEM/F12 GlutamaX, supplemented with: 0.3 % bovine serum albumin (BSA), 5 ng/mL Gentamycin, 0.1mM beta Mercaptoethanol, 1 % insulin-transferrin-selenium-ethanolamine (ITS-X), 0.2 % fetal bovine serum (FBS), 5 uM rho-associated protein kinase inhibitor (ROCKi), 2 uM glycogen synthase kinase 3 (GSK-3) inhibitor (CHIR99021), 0.5 uM activin/NODAL/TGF-beta pathway inhibitor (A83-01), 0.8 mM valproic acid sodium salt (VPA) and 50 ng/mL human epidermal growth factor (hEGF).
Syncytiotrophoblast (STB)	DMEM/F12 GlutamaX, supplemented with: 0.3% BSA, 5 ng/mL Gentamycin, 0.1 mM beta Mercaptoethanol, 1 % ITS-X, 2 uM Forskolin and 2.5 uM ROCKi.

Cigarette smoke extract

Cigarette smoke extract (CSE) generation. The reproducible collection of nicotine, cotinine and aqueous constituents of cigarette smoke in the form of CSE was performed using an established protocol with some modifications.[48] The apparatus to collect aqueous components was built without modifications. In short, the cap of a 50 mL conical tube was cut twice, with a quick-connect coupler inserted to one hole and 1.5 cm of 40 cm of small tubing to the other. Epoxy resin was applied to the cap using a cotton tip and let to set overnight. The next morning, 25 cm of large tubing was attached to the coupler on one side, and a 1 mL pipette tip to the other side. The pipette tip was replaced with each batch whilst tubing remained untouched. The cap screwed onto the conical tube containing 35 mL of basal DMEM/F12 GlutamaX medium used for TSC and STB cultures (see table titled ''trophoblast culture medium recipes used for primary in-vitro culture work''). Inside a chemical hood, the apparatus was fastened to a ring stand with 2 three-prong clamps. A 50mL glass syringe was connected to the small tubing and a reference 1R4F cigarette to the large tubing. The cigarette was marked at 23 mm including the filter. The syringe was greased with a single layer of petroleum jelly. To produce CSE, short 'puffs' (syringe drawn to 35 mL in 2-4 sec) followed by a 30 sec delay were performed. During this delay, the syringe was disconnected from the apparatus and smoke 'exhaled' by depressing plunger onto a paper towel. Through this, mainstream cigarette smoke was bubbled through the cell culture medium and soluble components captured to model human smoking. This process was repeated until reaching the 23 mm mark and number of 'puffs' recorded per cigarette, denoting a technical batch replicate. Per bacth replicate, 13 cigarettes were used. Four 100% CSE batches with 10 pooled technical replicates in each were made. Pooled batches were adjusted to 7.4 pH by adding 1M NaOH, sterile filtered through a 0.2 μM mesh, aliquoted and frozen at -70°C for characterization and use in in-vitro stimulations.

Nicotine and cotinine quantification in CSE. Quantification of nicotine and cotinine was done as described in Shin et al.[97] In short, A 20-mL glass test tube was used to hold 5 mL of CSE. Approximately 300 mg of potassium carbonate (K_2CO_3) and 50 μL of diphenylamine as an internal standard were added to the solution, which was then extracted with 7 mL of ethyl ether through 10 minutes of mechanical shaking. The organic phase was transferred to another 20-mL test tube containing 20 μL of acetic acid and dried using a nitrogen stream to a volume of 50 μL. The solution was further dried with around 100 mg of sodium sulfate before a 2-μL sample was automatically injected into the gas chromatography system. Calibration curves for nicotine and cotinine were established by extraction after adding standard amounts ranging from 1.0 to 5000 ng and 0.5 μg of internal standard to 5 mL of CSE. The ratio of the peak area of the standard to that of the internal standard was used to quantify the analytes. Mass spectra were obtained using an Agilent 6890/5973 N instrument, with the ion source operating in electron ionization mode at 70 eV. Full-scan mass spectra (m/z 40–800) were recorded for analyte identification. Separation was achieved using an HP fused-silica capillary column with cross-linked methylsiloxane. Samples were injected in split mode with a splitting ratio of 1:8, and the helium flow rate was 1.0 mL/min. Operating parameters include: injector temperature, 280°C; transfer line temperature, 300°C; and oven temperature, programmed from 80°C at 20°C/min to 300 °C (held for 5 min). The ions selected were m/z 84, 133, and 161 for nicotine, and m/z 98 and 176 for cotinine, and m/z 168 and 169 for diphenylamine.

VOC Screening of CSE by means of GC-MS. Volatile organic compounds (VOCs) were automatically injected into the GC using an Agilent 7697A static headspace sampler (SHS, Agilent Technologies, Vienna, Austria). For this purpose, 3.5 mL of 100% pooled CSE stock medium was transferred to a 20 mL headspace vial and spiked with nicotine-d_4 and 2-fluorobiphenyl as internal standards to achieve a final concentration of 0.99 and 1.00 μg per vial, respectively. To facilitate evaporation of VOCs in the headspace of the vial, a pre-equilibration temperature of 95°C was applied for 15 min before the analytes were automatically transferred to the GC inlet operated at 250°C. A 1 mL SHS loop was selected and maintained at 140°C with a transfer line temperature of 155°C to prevent compound loss. Helium (purity > 99.999%) was selected as GC carrier gas at a flow rate of 1.8 mL/min with a split ratio of 1:5. The

Please cite this article in press as: Valdes et al., Maternal smoking in early pregnancy disrupts placental function through syncytiotrophoblast and macrophage dysregulation, Cell Systems (2026), https://doi.org/10.1016/j.cels.2026.101785

separation was performed on an Agilent 5977B gas chromatograph using a cross-linked Agilent DB-Wax column with 30 m x 250 μm I.D. x 0.50 μm film thickness. The GC oven was initially held at 45°C for 2 min, followed by a thermal increase of 15°C/min to 260°C, held for 2 min. Detection was performed on an Agilent 5977 single quadrupole mass spectrometer (Santa Clara, CA, USA) operated in EI mode at 70 eV and a source temperature of 230°C. The single quadrupole was operated at 150°C in SCAN mode with m/z range from 33-550. Different solvent polarities were selected for the isolation of semi-volatile organic compounds, whereby a total of 20 mL of pure CSE medium was extracted 5 times with 7 mL of methylene chloride, followed by extraction with tert-methyl butyl ether and hexane, respectively. In this way, a total extract volume of 35 mL was obtained for each solvent, which was concentrated to a final volume of 150 μL containing 9.14 μg/mL of 2-fluorobiphenyl as an internal standard. A total of 2 μL of the extract was injected directly into the above-mentioned GC-MS system with similar parameters except for an adapted Agilent DB-Wax column with 60 m length x 250 μm I.D. x 0.25 μm film thickness operated with an extended temperature programme set to 260 °C for up to 10 min. Medium controls were included in the sample preparation and analysis workflow for all samples subjected to SHS or direct injection GC-MS. Peak picking was performed on spectral data using Agilent Masshunter Unknown Analysis (v10.1) and manually controlled using Masshunter Quantitative Analysis (v10.1). The peaks obtained were identified based on an in-house reference library build from certified reference standards together with a Wiley-National Institute of Standards and Technology (NIST) library search, with subtraction of corresponding sample blanks and an area threshold of at least 5000 counts. The analytes were quantified from their peak areas relative to the area of the respective reference standard or the area obtained for the internal standard 2-fluorobiphenyl.

RNA isolation and RT-qPCR

Cells from experiments previously described or pulverized tissue were lysed in QIAzol lysis reagent. RNA was isolated using the Qiagen RNease mini kit according to the manufacturer's instructions. RNA quality was determined using an Agilent 2100 Bioanalyzer. Quality check was followed by reverse transcription of 1 μg total RNA per reaction using the Applied Biosystems High-Capacity cDNA Reverse Transcription Kit according to the manufacturer's manual. For qPCRs, the QuantStudio 3 Real-Time PCR System with either TaqMan Fast Universal PCR Master Mix or Fast SYBR Green Master Mix were used. Primer and probes were designed using Real-time PCR (TaqMan) Primer and Probes Design Tool (online tool) from GenScript and synthesized by the company BioTez GmbH, Germany. Primers were diluted to a final concentration of 10 mM and probes to a final concentration of 5 mM. The target mRNA expression was quantitatively analysed using the standard curve method in the QuantStudio Design and Analysis Software (v2.6.0). All expression values were normalized to the housekeeping gene *18S*. Resulting values were plotted, tested for normality via Shapiro-Wilk and Anderson-Darling tests and compared between groups without removing outliers using either two-tailed unpaired Welch t-tests or two-tailed Mann-Whitney U test in GraphPad Prism software (v10.2.0). For validation cohort comparisons (Figures 3D and 3E), a multiple linear regression model was fitted with marker expression as dependent variable, and smoking status, maternal age, maternal BMI, and gestational age (GA) as covariates.

Human oligonucleotide primer sequences used to evaluate mRNA expression in independent validation cohort and in in-vitro cultured trophoblast cells

Target	Forward sequence	Reverse sequence	Probe sequence
18s	5′ ACA TCC AAG GAA GGC AGC AG 3′	5′ TTT TCG TCA CTA CCT CCC CG 3′	5′ FAM-CGC GCA AAT TAC CCA CTC CCG ACA-TAMRA 3′
CYP1A1	5′-TGG ATG AGA ACG CCA ATG TC 3′	5′-TGG GTT GAC CCA TAG CTT CT 3′	-
CYP1B1	5′TACCGGCCACTATCACTGAC 3′	5′ AAGGAAGGCCAGGACATAGG 3′	-
PGF	5′ CCTACGTGGAGCTGACGTTCT3′	5′ CCTTTCCGGCTTCATCTTCTC 3′	5′FAM-TCGCTGCGAAT GCCGGCC-TAMRA 3′
ADM	5′ CTGATGTACCTGGGTTCGCT 3′	5′ CACGACTCAGAGCCCACTTA 3′	5′FAM- AGGCGCTGACA CCGCTCGGT-TAMRA 3′
HMOX1	5′ AACTTTCAGAAGGGCCAGGT 3′	5′ GAAGACTGGGCTCTCCTTGT 3′	5′FAM- ACCCGAGACGG CTTCAAGCTGGT -TAMRA 3′
IL-6	5′ AGACAGCCACTCACCTCTTC 3′	5′ AGTGCCTCTTTGCTGCTTTC3′	-
ITGB5	5′ AGTGCCACCTCATGTGAAGA 3′	5′ GTTTGCCCTCAGATCACACC 3‘	-
ICAM1	5′- GTGACCGTGAATGTGCTCTC-3′	5′- CCTGCAGTGCCCATTATGAC -3′	-
SPP1	5′ GTTTCGCAGACCTGACATCC 3′	5′ CTCCTCGCTTTCCATGTGTG 3′	-

Immunofluorescence staining

Formalin fixed paraffin embedded (FFPE) placenta tissue sections (5 μm) were mounted on Superfrost Plus slides and dried overnight. Standard deparaffinisation was followed by antigen retrieval in the incubator with Tris/EDTA pH9 solution for 20 min at 93°C, cooled for 20 min, transferred to warm distilled water for 5 min and cooled for 5 min. Thereafter, sections were washed with PBST (PBS + 0.1% Tween 20) and blocked by incubation with Ultra V Block for 10 min at RT. For OGDH & mouse E-cadherin double staining, primary antibodies were diluted in primary antibody solution: PBST + 1% normal goat serum (NGS) + primary antibodies (see table titled "primary antibodies used for FFPE tissue immunofluorescent staining") and incubated on

sections overnight at 4°C. The following morning, slides were washed three times with PBST, stained with secondary antibody solution: PBST + 1% NGS + mouse IgG-Cy3 and rabbit IgG-AF488 (see table titled "secondary antibodies used for FFPE tissue immunofluorescent staining") and incubated in the dark at RT for 1 hour. After secondary antibody staining, slides were washed three times with PBST and mounted with VectaShield medium with DAPI. Rabbit immunoglobulin fraction and negative control mouse IgG were used as described above and revealed no staining. Slides were imaged using the Zeiss Axioscan 7 slide scanner. Regions of interest representing STB areas from four villi per tissue sample were selected using the open-source software for digital pathology image analysis QuPath (v0.4.2) and intensity per pixel quantified in a blinded fashion.

Primary antibodies used for FFPE tissue immunofluorescent staining

Epitope	Species	Isotype	Dilution	Supplier, cat #	Clone
CD163-PE (phycoerythrin) conjugated	Human	IgG1	1:50	Miltenyi #130-127908	REA1309
CD31	Mouse	IgG1	1:40	Dako #M0823	JC70A
E-cadherin	Rabbit	IgG	1:200	Cell Signalling #3195	24E10
E-cadherin	Mouse	IgG1	1:100	Cell signalling #14472	4A2
HLA-G	Mouse	IgG1	1:200	ExBio #11-291-C100	MEM-G/1
OGDH	Rabbit	polyclonal	1:100	Sigma # HPA020347	-
Fibrin	Mouse	IgG1	1:500	Merck # MABS2155	59D8
CD42b	Rabbit	polyclonal	1:500	Proteintech #12860-1-AP	-

Secondary antibodies used for FFPE tissue immunofluorescent staining

Isotype specificity	Host	Fluorophore	Dilution	Supplier, cat #
Mouse IgG	Goat	AlexaFluor-647	1:1000	Invitrogen, A21235
Rabbit IgG	Goat	AlexaFluor-488	1:1000	Invitrogen, A11008
Mouse IgG	Goat	Cyanine 3 (Cy3)	1:1000	Jackson Laboratories, #715-165-151
Mouse IgG	Goat	AlexaFluor-555	1:200	Invitrogen, A32727
Rabbit IgG	Goat	AlexaFluor-633	1:200	Invitrogen, A21070

Proteomics

Deep visual proteomics (DVP). Formalin fixed, paraffin embedded (FFPE) placenta tissue sections (5 μm) were mounted on PPS FrameSlides (cat.no. 11600294) and dried overnight. Standard deparaffinisation was followed by antigen retrieval in the incubator with Tris/EDTA pH9 solution for 20 min at 93°C, cooled for 20 min, transferred to warm distilled water for 5 min and cooled for 5 min. Thereafter, sections were washed with PBST (PBS + 0.1% Tween 20) and blocked by incubation with Ultra V Block for 20 min at RT. For triple staining (CD163, CD31, E-cadherin), primary antibodies were mixed and diluted in primary antibody solution: PBST + 1% normal goat serum (NGS) + primary antibodies and incubated on sections overnight at 4°C. The following morning, slides were washed three times with PBST, stained with secondary antibody solution: PBST + 1% NGS + mouse IgG-AF647 & rabbit IgG-AF488 and incubated in the dark at RT for 1 hour. After secondary antibody staining, slides were washed three times with PBST and mounted with Slow Fade Diamond Mounting Medium (cat.no. 36964) with DAPI. Serial tissue sections were stained with HLA-G to exclude the selection of cell column trophoblasts as regions of interest. Rabbit immunoglobulin fraction and negative control mouse IgG were used as described above and revealed no staining. Slides were imaged using the Zeiss Axioscan 7 slide scanner using a 10X objective and 2x2 binning. Regions of interest representing cell phenotypes were manually labelled using the open-source software for digital pathology image analysis QuPath (v0.4.2). Regions of interest were collected by laser microdissection (LMD) on a Leica LMD7 microscope using a 63x objective operated in brightfield mode. An area of approximately 50,000 μm^2 was collected in quadruplicate technical replicates per phenotype per biological sample into individual wells of a 384-well plate.

Collected cells were processed for bottom-up LC-MS based proteomics as recently described,[31] with small adjustments. Briefly, acetonitrile (2x10uL) was pipetted to each well to drag samples to the bottom of their wells, and later evaporated with rotovap. For cell lysis, 4 μl of 60 mM triethylammonium bicarbonate (TEAB) was added to each well, shortly centrifuged (2,000 RCF, 1 min) and the plate heated at 95°C for 60 min in a thermal cycler (Bio-Rad, 384-well reaction module) at a constant lid temperature of 110°C. 1 μl of acetonitrile (ACN) was then added to each well (20% final concentration) and heated again at 75°C for 60 min in the thermal cycler. Samples were shortly cooled to room temperature and 2 μl LysC added pre-diluted in ultra-pure water to 2 ng/μl and digested for 4 h at 37°C in the thermal cycler. Subsequently, 2 μl trypsin (Promega Trypsin Gold) was added pre-diluted in ultra-pure water to 2 ng/μl and incubated overnight at 37°C in the thermal cycler. The next day, digestion was stopped by adding trifluoroacetic acid (TFA, final concentration 1% v/v) and samples vacuum-dried (approx. 60min at 60°C). Samples were stored at -20°C until LC-MS

Please cite this article in press as: Valdes et al., Maternal smoking in early pregnancy disrupts placental function through syncytiotrophoblast and macrophage dysregulation, Cell Systems (2026), https://doi.org/10.1016/j.cels.2026.101785

availability. Finally, 4 μl MS loading buffer (3% ACN in 0.2% TFA) was added, the plate vortexed for 10s and centrifuged for 5 min at 2,000 RCF.

Cell culture pellet proteomics sample preparation. Primary human trophoblast stem cells (TSCs) cultured in TSC medium were harvested upon reaching ~80% confluency with TryplE for 10 minutes at 37°C and seeded at a density of 0.1 x 10^6 cells per well of a 12w plate pre-coated with 2.5 μg/mL collagen IV. After attachment for 24 hours, cells were cultured in STB medium to direct differentiate them towards the STB lineage.[41] Medium was replaced daily for the first four days. Between days 5 and 7 media was replaced every 12 hours in the presence or absence of cigarette smoke extract (CSE) diluted 1:200 in STB medium. At days 0, 5, 6 and 7 cells were harvested with TryplE for 12 minutes at 37°C and centrifuged for 6 min at 300 RCF to collect pellets. Pellets were transferred to 1.5 mL reaction tubes, washed thrice with PBS for 5 min at 300 RFC, air dried and frozen at -70°C. M2-phentoype differentiated macrophages stimulated for 24 hours with osteopontin [1 ng/uL] were pelleted and washed in the same way. Cell pellets were lysed with 50uL of sodium deoxycholate lysis buffer (1% (w/v) SDC, 150 mM NaCl, 100 mM Tris pH 8, 1 mM EDTA, 10 mM DTT, 40 mM CAA, 1:100 phosphatase inhibitor cocktail), each tube was vortexed, spinned down, and transferred to a 96 well plate. The samples were incubated for 10min at 95°C, then 25 U of benzonase were added to each sample. Peptide digestion took place by adding 1uL of 10 ng/uL trypsin/LysC mixture (1:50 ratio), then incubating samples at 37°C overnight. 5uL of 10 % formic acid (FA) was added to stop lysis, and precipitate the SDC salts, then the supernatant for each well was transferred to a new plate, if needed 1 % FA was added to dilute samples to a suitable volume. Samples were then washed by stage-tipping using EVOSEP Evotip Pure tips with Agilents's AssayMAP Bravo. Protein concentration was measured by nanodrop, and each sample was diluted in a new plate to 100 ng/uL.

Liquid chromatography mass spectrometry (LC-MS) analysis. For both DVP and cell pellet proteomics, LC-MS analysis was performed with an EASY-nLC-1200 system (Thermo Fisher Scientific) connected to a trapped ion mobility spectrometry quadrupole time-of-flight mass spectrometer (timsTOF SCP, Bruker Daltonik GmbH, Germany) with a nano-electrospray ion source (Captive spray, Bruker Daltonik GmbH). Peptides were loaded on a 20 cm in-house packed HPLC-column (75 μm inner diameter packed with 1.9 μm ReproSilPur C18-AQ silica beads, Dr. Maisch GmbH, Germany). Peptides separation followed a gradient with a flow rate of 250 nL with increasing concentration of buffer B (0.1% formic acid, 90% ACN in LC-MS grade H_2O) to 60%. Buffer A (3% ACN, 0.1% formic acid in LC-MS grade H_2O). The total gradient length was 21 min and 44 min, for DVP and STB pellet samples, respectively. Column temperature was controlled by a column oven and kept constant at 40°C. Mass spectrometric aquisition was performed in data-independent (diaPASEF) mode[98] using the default method for long gradients with a cycle time of 1.8 s. Ion accumulation and ramp time in the dual TIMS analyser was set to 100 ms each and we analysed the ion mobility range from 1/K0 = 1.6 Vs cm-2 to 0.6 Vs cm-2. The total m/z range was set to 100-1,700 m/z. The collision energy was lowered linearly as a function of increasing mobility starting from 59 eV at 1/K0 = 1.6 VS cm-2 to 20 eV at 1/K0 = 0.6 Vs cm-2. Singly charged precursor ions were excluded with a polygon filter (timsControl software, Bruker Daltonik GmbH).

Enzyme-linked immunosorbent assays

The blood samples from women in the first trimester of pregnancy used were taken prior to the surgical elective termination procedure, and serum isolated by routine centrifugation protocols. Samples were analyzed for cotinine (Abnova #KA0930) and placental growth factor (R&D Systems #DPG00) concentrations according to manufacturer's instructions. Absorbance was read at 450 nm (with 540nm wavelength correction) using the spectrometer SPECTROstar Nano. For the cotinine ELISA, assay sensitivity is 1 ng/mL, the cut-off for smokers was set at 3 ng/mL cotinine and cross reactivities include nicotine <1 %, nicotinamide <1 % and nicotinic acid <1 %. For the PlGF ELISA, assay sensitivity is 7 pg/mL, no cut-offs were used and no reported significant cross-reactivities are present.

Mitochondria toxicity assay. This cell-based assay is specifically designed to predict mitochondrial dysfunction as a result of xenobiotic exposure using multiplexed chemistry (Promega, G8000). The assay was conducted on STB differentiated cells with dilutions of CSE exposure of 1:100, 1:150 and 1:200 for 2h according to manufacturer's instructions.

Villous fibrin and platelet analysis. Images of double-stained for fibrin and the platelet marker CD42b tissue were obtained using an Evident Olympus VS200 Slide Scanner and afterwards subjected to Visiopharm (Version 2021.09) and CellProfiler (Version 3.1.9) for a software-based quantification. Villous regions were detected within each sample by applying a threshold on a feature combining a polynomial gradient filter of FITC and a mean filter feature of the DAPI channel. Fibrin regions were detected by a FITC channel threshold. Adherent platelets were detected by measuring CD42b positive signals using the Cy3 channel. Fibrin area (μm^2) and platelet area (μm^2) was normalized to total villi area (μm^2) for comparisons.

QUANTIFICATION AND STATISTICAL ANALYSIS

snRNAseq

Data processing and quality control

The demultiplexing, processing, identification of Unique Molecular Identifiers (UMI) and barcode filtering of raw 3′ snRNAseq data was performed using Cell Ranger software (v 6.1.2) from 10x Genomics. The transcripts were aligned against the pre-built human reference genome GRCh38 premRNA version 3.0.0, which was built from the GRCh38 precompiled reference, and modified for use with snRNAseq data by extracting "transcripts" features from the gene model GTF and instead annotating these as "exon", as described in the protocol defined by 10x Genomics (https://support.10xgenomics.com/single-cell-gene-expression/software/release-notes/build#grch38_3.0.0). Technical systematic background noise including ambient RNA molecules, random barcode

Please cite this article in press as: Valdes et al., Maternal smoking in early pregnancy disrupts placental function through syncytiotrophoblast and macrophage dysregulation, Cell Systems (2026), https://doi.org/10.1016/j.cels.2026.101785

swapping from raw (UMI) matrices and empty droplets were optimised per sample and eliminated using the CellBender package (v0.2.2) in python (v3.7.0) with 18,000 total number of droplets, 150 epochs, 0.01 fpr using a combined ambient and swapping model. Technical doublets were modelled per sample using DoubletFinder (v2.0.3). Subsequently, pre-processed matrices were loaded into R (v4.1.2) and further processed using Seurat (v4.1.0). Genes expressed in fewer than 10 nuclei per sample were removed from the count matrices. Within-sample nuclei having fewer than 200 expressed genes, a log10 ratio of genes per UMI <. 0.80, more than 0.5% expression belonging to mitochondrial genes or having a single-gene expression spanning > 30% of counts were filtered out and excluded. Distributions of the abovementioned metrics were evaluated and recorded. Three sequenced tissue samples did not pass quality control expectations and were excluded from the study which included two smokers and one control samples. 88,808 nuclei were included with an overall capture of 28,269 genes and a mean of approximately 4,000 genes mapped to any given nucleus. Fetal sex was inferred based on gene expression patterns of female-associated (*XIST, PCDH11X, ZFX*) and male-associated (*PCDH11Y, USP9Y, DDX3Y, TTTY14*, *EIF1AY*).

Data integration and cell type and state annotation

Dataset integration was performed to model and correct for gene expression heterogeneity in samples attributable to differences in biological (sample ID, fetal sex) and technical (batch, sequencing depth) variation using the 'sctransform' package (v0.3.3). A zero-inflated negative binomial distribution was used to model gene expression. Anchor features across datasets were computed with the 'FindIntegrationAnchors' function using the 4,000 most variable genes computed with the 'SelectIntegrationFeatures' function. With integration anchors as foundation, datasets were integrated after normalization and variance stabilization with the 'SCTransform' function without regressing mitochondrial counts or sequencing depths. Cell cycle state was annotated using cell cycle scores with the 'CellCycleScoring' function that predicts S, G2M and G1 phases based on expression correlation of canonical marker sets.

Gene expression counts from the integrated dataset was used for cell type and state annotation. Gene expression counts from non-integrated data were used for downstream analyses.

Linear dimensionality reduction was performed on the 4,000 most variable genes of the integrated dataset and 50 principal components (PCs) were calculated. The K-nearest neighbour graph was computed using the first 30 PCs. Uniform Manifold Approximation and Projection (UMAP) visualisation was used to further reduce the high dimensional latent spaces to 2D using the first 50 PCs. In this visualisation, dots correspond to specific nuclei with unique x,y coordinates. Louvain clusters were computed in an unsupervised manner based on the k-nearest neighbour graph at resolutions between 0.1 and 2 in 0.1 step increments using the Louvain algorithm with modularity optimizer version 1.3.0 by Ludo Waltman and Nees Jan van Eck, including a random seed for reproducibility. The most appropriate resolution (1.0 yielding 36 clusters) to use for annotation was selected based on a cluster tree relationship visualisation at all resolutions using the clustree package (v0.5.1). Differentially expressed and conserved genes between clusters was calculated using the logistic regression based 'FindAllMarkers' and 'FindConservedMarkers' functions in Seurat package, respectively. This information was used for annotation in combination with the cluster-specific expression of literature-based canonical markers. One contaminating cluster (n = 474 nuclei) negative for all placental canonical markers and uniquely expressing maternal decidua epithelial cell markers *PAX8, PAEP* and *CP* was removed. Ultimately, clusters with unique transcriptomic fingerprints in relation to the rest of the dataset were annotated as their own cell type or state, whilst clusters with conserved transcriptomic fingerprints were merged to belong to the same type or state.

Differential gene expression analysis

Differential expression was performed on raw RNA counts from all annotated cell types and states excluding proliferating erythroblasts (EBp) and fibroblasts (FBp) due to their low abundances. Counts and associated metadata from Seurat were used to create a SingleCellExperiment object (v.1.22.0). Pseudo-bulk gene expression profiles were generated by aggregating counts for nuclei of the same cell phenotype and tissue sample ID using the 'aggregateAcrossCells' function in the scuttle package (v1.4.0).

Differentially expressed genes (DEGs) per cell phenotype were empirically calculated using the edgeR package (v3.36.0). First, a DGEList object from the pseudo-bulk profiles was created and genes that were not expressed above a log-CPM threshold in a minimum of five samples (the size of the smallest group in our experimental design) were filtered out. Nuclei with fewer than ten counts were also removed. Normalization factors were calculated using the trimmed mean of M-values (TMM) method to account for composition biases in the data. A design matrix was constructed and included batch and fetal sex to model the effects of these variables on gene expression. Robust dispersion estimates were obtained using the 'estimateGLMRobustDisp' function, which accommodates for potential outliers. A negative binomial generalized linear model was fitted genewise using the 'glmFit' function with robust parameter settings to compute the maximum likelihood estimates of coefficients for the distribution, accomodating for variability across samples. Finally, DEG testing was performed using a likelihood ratio test in the 'glmLRT' function with a contrast matrix defined by the 'makeContrasts' function to compare between smoker and non-smokers. Analysis results were FDR-corrected by Benjamini-Hochberg method using the 'topTags' function. These results were compiled for each cell phenotype and the final output exported to a .csv file. To complement the prior analysis, cell phenotypes most perturbed to smoking status were investigated using the Augur package (v1.0.3). Scaled and normalized RNA counts were used to calculate areas under the curve per phenotype with the 'calculate_auc' function, with higher numbers representing higher biological perturbations within a high-dimensional space quantified using a machine learning classifier framework.

Trophoblast trajectory modelling

To model the differentiation trajectory of the trophoblast, subsetting of the 67,618 nuclei annotated as trophoblast cell types or states (CTBp, CTB, CTBpf, STBim, STB, CCT) was performed. To ensure a most adequate inference, gene expression counts were further filtered to include nuclei with a minimum count of 600 genes, resulting in 63,077 nuclei included for this analysis. First, the non-

Please cite this article in press as: Valdes et al., Maternal smoking in early pregnancy disrupts placental function through syncytiotrophoblast and macrophage dysregulation, Cell Systems (2026), https://doi.org/10.1016/j.cels.2026.101785

integrated gene expression count matrix was split into a test and training matrices of counts using the 'countsplit' function of the countsplit package (epsilon 0.5, v1.0.0). These matrices are independent under specific modelling assumptions and are therefore robust for use in cross validations. The trajectory modelling was performed on the training matrix and the leaf and transition gene analysis on the test matrix. Linear dimensionality reduction was performed on the 4,000 most variable genes of the integrated dataset and 30 PCs were calculated. The K-nearest neighbour graph was computed using the first 30 PCs. UMAP visualisation was used to further reduce the high dimensional latent spaces to 2D using the first 30 PCs. Louvain clusters were computed in an unsupervised manner based on the k-nearest neighbour graph at resolutions between 0.1 and 1 in 0.1 step increments using the Louvain algorithm with modularity optimizer version 1.3.0 by Ludo Waltman and Nees Jan van Eck, including a random seed for reproducibility. The most appropriate resolution to use for annotation was selected based on cluster relationship visualisation at all resolutions by building a cluster tree using the clustree package (v0.5.1). The resolution of 0.3 yielding 10 clusters was used. Counts and associated metadata from Seurat were used to create a SingleCellExperiment object (v.1.22.0). To evaluate if a shared or separate trajectory should be fit depending on maternal smoking staus, an imbalance score was calculated using the 'imbalance_score' function (k = 20, smooth = 40) from the condiments package (v1.2.0). Given that no score was greater than 3.5, a common trajectory was fitted. The trajectory was modelled on the subsetted UMAP graph using the 'slinghot' function in the slingshot package (v2.2.1) with the starting cluster set to cluster 2 based on its expression of proliferating markers TOP2A and MKI67. The function identifies global structure with a cluster-based minimum spanning tree and fits simultaneous principal curves to describe each lineage. A pseudotime is allocated to each nucleus for a maximum of two possible trajectories, with an associated weight indicating the predicted certainty of each assignment. Modelled trajectories included three distinct lineages going towards the STB fate, the CTB fate and the CCT fate. Differences between pseudotime densities for each lineage were assessed in consideration of the curve weights, by a permutation test (10,000 replicates) and Kolmogorow-Smirnov per lineage using the 'progressionTest' function of the slingshot package. Differential differentiation between smoking status along pseudotime per lineage was assessed by a quasibinomial generalised linear model using the 'glm' function in the stats package (v4.1.2).

Transition and leaf gene inference was performed on non-smokers nuclei only (n = 36,022 nuclei). Transition genes along each inferred lineage trajectory were calculated as described in Chen etal.[99] First, genes with a $\log_2$FC lower than ± 0.25 between the first 20% and last 20% of nuclei in the inferred pseudotime were filtered out. For transition genes, expression values per modelled lineage were scaled between 0 and 1, and a spearman correlation between gene expression and pseudotime values was fitted gene-wise using the 'cor.test' function of the stats package (v4.1.2). Genes with a Spearman's correlation coefficient of ± 0.4 were identified and reported as transition genes. For the leaf gene calculation, DEGs per lineage were empirically calculated using the edgeR package (v3.36.0). A DGEList object from the count matrix was created and genes that were not expressed above a log-CPM threshold in a minimum of five samples were filtered out. Normalization factors were calculated using the trimmed mean of M-values (TMM) method to account for composition biases in the data. A design matrix was constructed and included batch and fetal sex to model the effects of these variables on gene expression. Robust dispersion estimates were obtained using the 'estimateGLMRobustDisp' function, which accommodates for potential outliers. A negative binomial generalized linear model was fitted genewise using the 'glmFit' function with robust parameter settings to compute the maximum likelihood estimates of coefficients for the distribution, accomodating for variability across samples[151]. Finally, DEG testing was performed using a likelihood ratio test with the 'glmLRT' function with a contrast matrix defined by the 'makeContrasts' function to compare between smoker and non-smokers. The results of the analysis were FDR-corrected by Benjamini-Hochberg method using the 'topTags' function.

Network hub genes inference, TF-prediction and pathway enrichment analyses

The list of DEGs based on cut-off values (logFC +/-0.25 and FDR < 0.1) were used as background for networks. Genes were used as input in the stringDB for protein-protein interaction (PPI) networks (confidence level = 0.4, no added proteins in shells). Networks were then further analysed in Cytoscape (v3.10.1). Hub genes, defined as genes with high connectivity across DEGs, were identified from the PPI network calculating top 10 genes for all CytoHubba plug-in topological analysis methods (DMNC; MNC, MCC, ecCentricity, Bottleneck, Degree, EPC and Closeness). The candidate hub genes were merged into one network and decomposed into communities using the cytoscape plug-ins clustermaker and GLay, based on Newman and Girvan's edge-betweenness algorithm. The original background $\log_2$FC was used for continuous mapping colours. The hub gene network was used to calculate transcription factors via the plug-in iRegulon (standard threshold: enrichment score threshold 3.0, ROC threshold for AUC calc 0.03, Rank threshold 5000, minimum identity between orthologous genes: 0.0, max FDR on motif similarity: 0.001). Predicted transcription factors were visualised as PPI (confidence level 0.15, no added proteins in shells) via stringDB.

Pathway enrichment analysis was performed using the 1D annotation enrichment method in Perseus software (v1.5.15.0). Enrichment was done based on ranked log fold changes without thresholding spanning the gene set enrichment analysis (GSEA), reactome and the WikiPathways databases.

Cell-cell communication analysis

Ligand receptor pair communication was systematically inferred per omics modality (snRNAseq and DVP) as well as per condition separately using CellChat v2 R package with the human CellChatDB ligand–receptor database.[51] For each smoking-status group separately, we subsetted the expression matrix to genes included in CellChatDB "secreted," "cell-cell contact" or "ECM-receptor" categories and identified over-expressed ligands and receptors in each cell group using a one-sided Wilcoxon rank-sum test with default parameters. Communication probabilities for all ligand–receptor pairs between cell groups were then computed using the mass-action model implemented in 'computeCommunProb', with expression aggregation for multi-subunit complexes and cofactors as defined in CellChatDB. Interactions were filtered to retain only those supported by a minimum of 10 expressing cells and

Please cite this article in press as: Valdes et al., Maternal smoking in early pregnancy disrupts placental function through syncytiotrophoblast and macrophage dysregulation, Cell Systems (2026), https://doi.org/10.1016/j.cels.2026.101785

with non-negligible communication probability according to default thresholds. Statistical significance of each interaction was assessed by permutation testing (n=1000), in which cell-group labels were randomly shuffled and communication probabilities recomputed, followed by multiple-testing correction. Ligand–receptor interactions were subsequently aggregated to the signaling pathway level using 'computeCommunProbPathway', which summarizes interactions annotated to the same pathway. Smoker- and non-smoker-specific communication networks were compared to identify pathways with altered outgoing or incoming signaling strength for the syncytiotrophoblast (STB) and placental macrophage (HBC) cell types. Network-level metrics (e.g., overall information flow, sender/receiver roles) and pathway-level differences were visualized using CellChat's built-in functions, including 'netVisual_aggregate' and 'netVisual_heatmap'. Results were manually curated into an integrated figure.

Proteomics

Proteomics measurements were analysed using the timsControl software (Bruker Daltonik GmbH, v. 3.1). Raw files were analysed with DIA-NN (v. 1.8.1 and 1.8.2 beta 25; for DVP and cell pellet samples, respectively)[163] in library-free mode based on a predicted human spectral library (Uniprot 2021 release). Default settings were used with small adjustments. The mass range was set to 100–1,700 m/z, precursor charge state was 2 - 4 and the maximum number of allowed miscleavages was 2. MS1 and MS2 mass accuracies were set to 15 ppm and the match-between-runs option was enabled. Quantification strategy was set to 'Robust LC'. For downstream data analysis, we used the protein FDR filtered pg_matrix.tsv and unique_genes_matrix.tsv DIA-NN output tables were analysed with Perseus (v. 1.6.15.0) and the Protigy interactive web app (v. 1.0.2,). Missing values were imputed based on a shifted normal distribution of $\log_2$ transformed sample values (width = 0.3; downshift = -1.8) after stringent data filtering (minimum of 70% quantified values across samples). In the case of microdissected cells for DVP, prior to principal component analysis (PCA), batch effects were corrected with the proBatch R package (v. 1.10.0) based on the ComBat method. Differential abundance was evaluated using the limma package (v 3.56.2) by fitting a linear model (lmFit) on a design matrix of protein abundance data adjusted by a contrast matrix representing smoking status. Empirical Bayes moderation (eBayes) was used on the standard errors to produce moderated t-statistics. False discovery rate was controlled using a Benjamini-Hochberg correction. Pathway enrichment analysis was performed using the 1D annotation enrichment method in Perseus software. Enrichment was done based on ranked log fold changes spanning the gene ontology (GO), gene set enrichment analysis (GSEA), reactome and the Kyoto encyclopedia of genes and genomes (KEGG) databases.

HubGene inference and transcription factor prediction

The list of differentially abundant proteins based on cut-off values (logFC +/-0.25 and FDR < 0.1) were used as background for networks. Proteins were used as input in the stringDB for protein-protein interaction (PPI) networks (confidence level = 0.4, no added proteins in shells). Networks were then further analysed in Cytoscape (v3.10.1). Hub genes, defined as genes with high connectivity across differentially abundant proteins, were identified from the PPI network calculating top 10 genes for all CytoHubba plug-in topological analysis methods (DMNC; MNC, MCC, ecCentricity, Bottleneck, Degree, EPC and Closeness). The candidate hub genes were merged into one network and decomposed into communities using the cytoscape plug-ins clustermaker and GLay, based on Newman and Girvan's edge-betweenness algorithm. The original background $\log_2$FC was used for continuous mapping colours. The hub gene network was used to calculate transcription factors via the plug-in iRegulon (enrichment score threshold 3.0, ROC threshold for AUC calc 0.03, Rank threshold 5000, minimum identity between orthologous genes: 0.0, max FDR on motif similarity: 0.001). Predicted transcription factors were visualised as PPI (confidence level 0.15, no added proteins in shells) via stringDB.

Pathway enrichment analysis was performed using the 1D annotation enrichment method in Perseus software (v1.5.15.0). Enrichment was done based on ranked log fold changes without thresholding spanning the gene set enrichment analysis (GSEA), reactome and the WikiPathways databases.

For in-vitro and validations, groups were compared between smoking and non-smoking groups using two-tailed Mann-Whitney U test in GraphPad Prism software (v10.2.0).

Visualizations

The following packages were used to compile the computational analyses visualisations: tidyr (v1.2.0), ggplot2 (v3.3.6), patchwork (v1.1.1), cowplot (v1.1.1), enhancedVolcano (v1.18.0), viridis (v1.6.4), ComplexHeatmap (v2.16.0), RColorBrewer (1.1.3), Seurat (v4.1.0), RVenn (1.1.0), slingshot (v.2.2.1), clustree (v.0.5.1), pheatmap (v1.0.12). Baseline characteristics, qPCR and ELISA results were plotted using GraphPad Prism (v10.2.0). Results from network analyses (hub gene and pTF inference) were visualised using cytoscape (v3.10.1).

Figure panels were arranged using Adobe Illustrator (v27.5).

Cell Systems, Volume *17*

Supplemental information

Maternal smoking in early pregnancy disrupts placental function through syncytiotrophoblast and macrophage dysregulation

Daniela S. Valdes, Jose Nimo, Olivia Nonn, Juliane Ulrich, Désirée Forstner, Sandra Haider, Miriam Ressler, Marc Pignitter, Barbara Obermayer-Pietsch, Dominik N. Müller, Ralf Dechend, Martin Gauster, Fabian Coscia, and Florian Herse

SUPPLEMENTARY INFORMATION
Valdes et al. Maternal smoking in early pregnancy disrupts placental function through syncytiotrophoblast and macrophage dysregulation. 2026

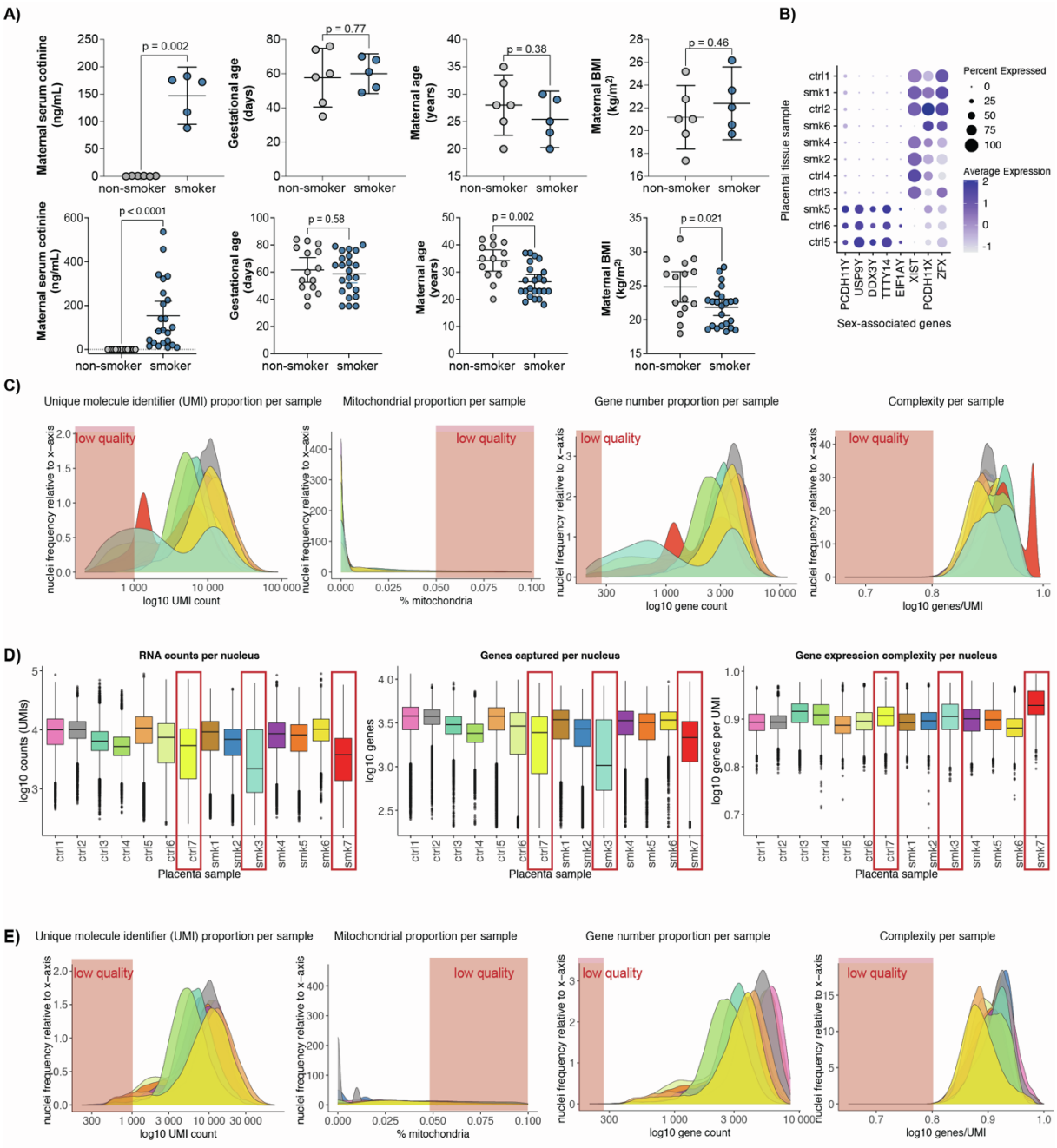

Supplementary Figure 1. Baseline characteristics of included tissue cohorts and quality control of snRNAseq placental samples.
(A) Top: Baseline characteristics of cohort used for RNA sequencing and spatial proteomics. Participants were matched for gestational age, maternal age and maternal body mass index (BMI) (*n* = 5 smokers, *n* = 6 non-smokers). Bottom: Baseline characteristics of validation cohort. Participants were matched for gestational age, whilst maternal age and maternal body mass index (BMI) were lower in smokers, consistent with epidemiological data (*n* = 23 smokers, *n* = 14 non-smokers). Differences between groups assessed via two-tailed unpaired t-tests with Welch's correction.
(B) Dotplot with expression values of sex-associated genes per placental tissue used to infer fetal sex in the dataset. Expression plotted is scaled gene-wise. Samples with expression of male-associated gene *PCDH11Y, USP9Y, DDX3Y, TTTY14* and *EIF1AY* were classified as

male, whilst those expressing female-associated genes *XIST, PCDH11X* and *ZFX* were classified as female.
(C) Density plots of key quality control metrics for snRNAseq samples used. These include UMI counts per samples as an indicator of transcriptional activity captured; percentage of mitochondrial reads per sample as indicator of sample integrity; gene number per sample as insight into transcriptional diversity; the ratio between genes captured per UMI as measure for transcriptional complexity. Low quality thresholds are indicated by red boxes.
(D) Boxplots summarizing key metrics across individual samples. Samples falling outside of the expected range that did not pass quality control thresholds are highlighted in red boxes and excluded from further analyses.
(E) Density plots of consistent and reliable quality control metrics from included high-quality samples, ensuring dataset robustness for downstream analyses. Thresholds set excluded nuclei from high-quality samples that had less than 1000 UMI count, more than 0.5% percentage mitochondrial counts, less than 200 gene counts and a ratio of less than 0.8 log10 genes per UMI.

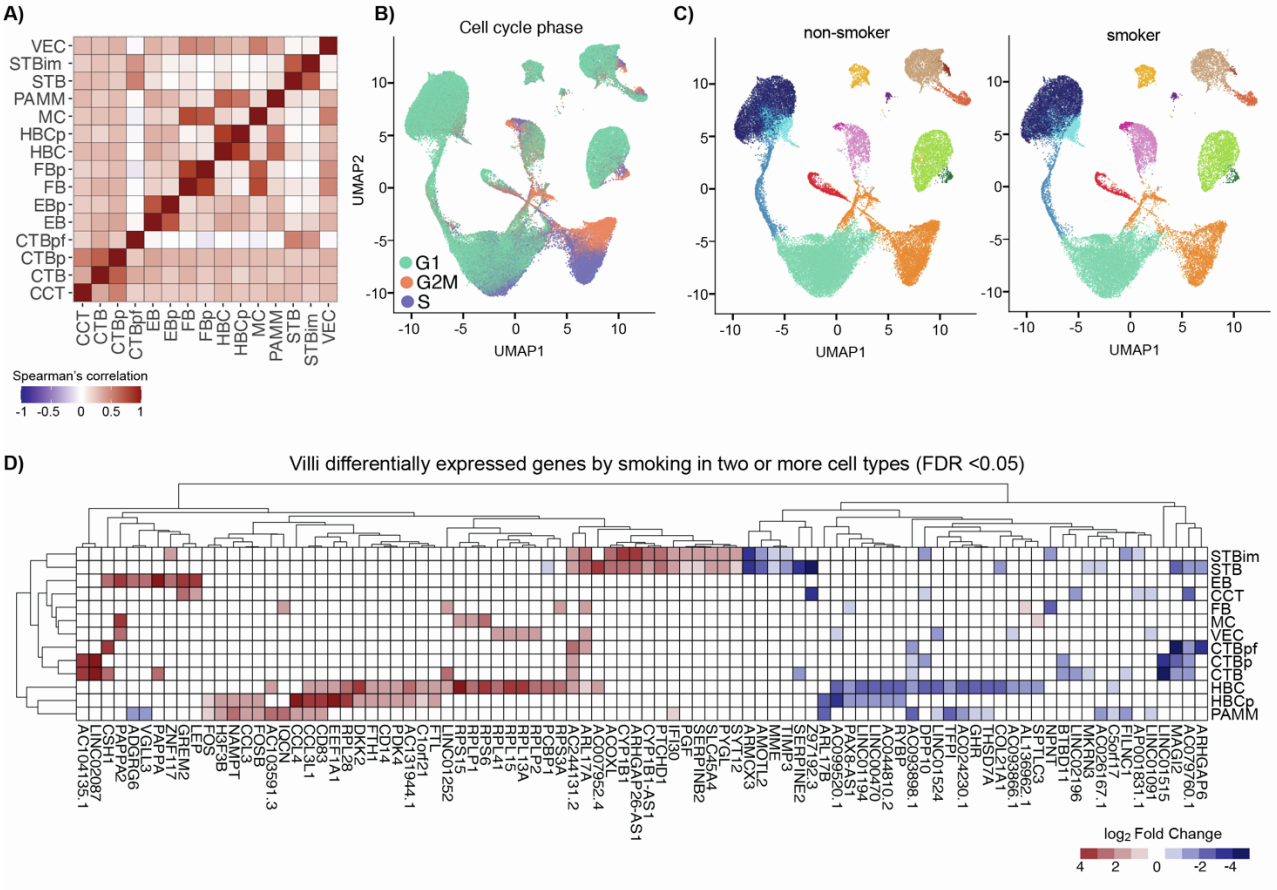

Supplementary Figure 2. Dysregulated cell types and states in the early human placenta display minimal global dysregulation patterns.

(A) Spearman correlation heatmap of whole-transcriptome correlations between maternal smokers and non-smokers.

(B) Uniform manifold approximation projection (UMAP) embedding of calculated cell cycle phase scores per nucleus. As expected, proliferating states map to the G2M and S phases, while non-proliferating states primarily map to the G1 cell cycle phase.

(C) UMAP of harmonized dataset colored by annotated cell types and states separated by maternal smoking status (left, non-smoker; right, smoker). Colors map to annotated cell types in Figure 1. n = 50,052 non-smoker nuclei, n = 38,756 smoker nuclei.

(D) Heatmap of dysregulated genes (log2FC) by maternal smoking present in two or more annotated cell type or state groups at a 5% FDR.

CTB, cytotrophoblast; STB syncytiotrophoblast; CCT, cell column trophoblast; HBC, Hofbauer cell; PAMM, placental-associated maternal macrophage; EB, erythroblast; FB, fibroblast; MC, myocyte; VEC, vascular endothelial cell; p, proliferating; pf, pre-fusion; im, immature.

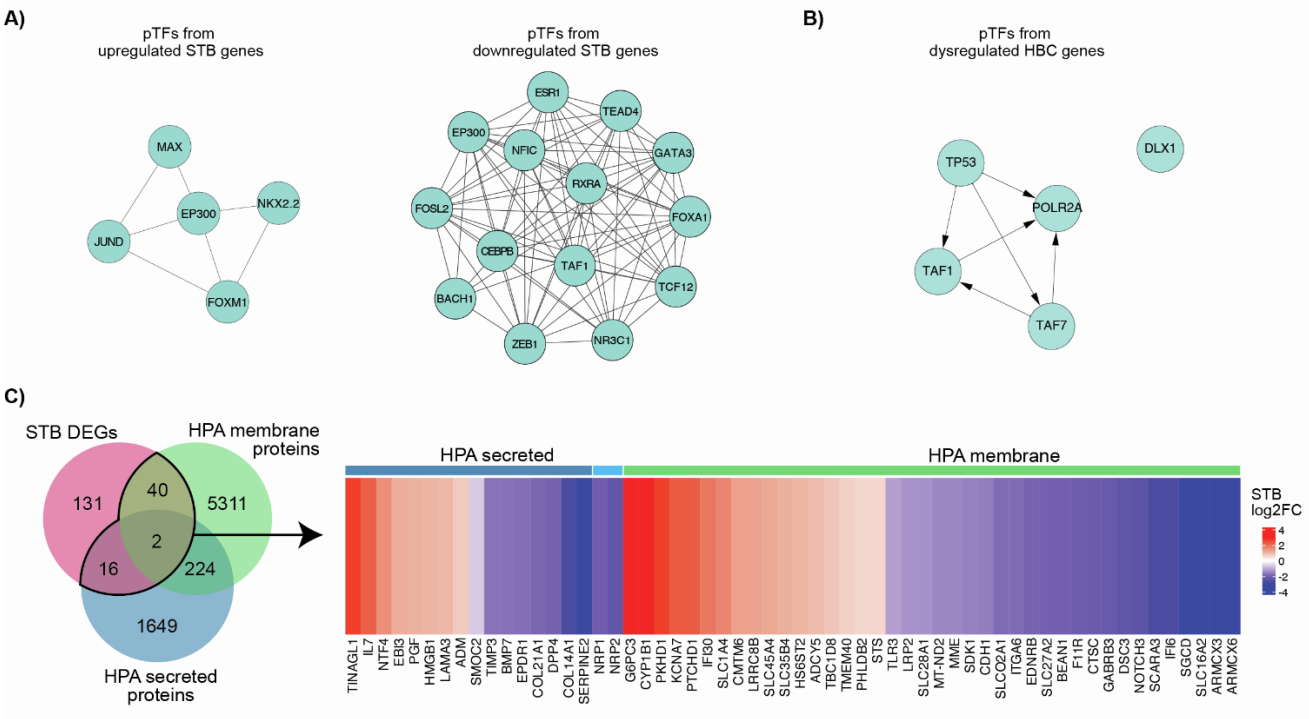

Supplementary Figure 3. Predicted transcription factors modulating orchestrated dysregulation by smoking.

(A) Predicted STB transcription factors (pTFs) modulating up (left) and down (right) hub gene networks calculated using the iRegulon cytoscape plugin. pTFs are visualized as a protein-protein interaction network (confidence level 0.15, no added proteins) using stringDB.

(B) Predicted HBC transcription factors (pTFs) modulating dysregulated hub gene networks calculated using the iRegulon cytoscape plugin. pTFs are visualized as a protein-protein interaction network (confidence level 0.15, no added proteins) using stringDB.

(C) Left: Venn diagram of STB DEGs (absolute $log_2FC > 0.25$, FDR < 0.1) overlapping with human membrane and secreted proteins as annotated by the human protein atlas (HPA) database. Right: Heatmap of overlapping STB dysregulated proteins as highlighted in (B) ordered by their HPA annotation membership. Heatmap color represents measured log_2FC between groups. Dark blue top legend represents HPA secreted annotated genes, light blue represents genes annotated as both secreted and membrane, green represents HPA membrane annotated genes.

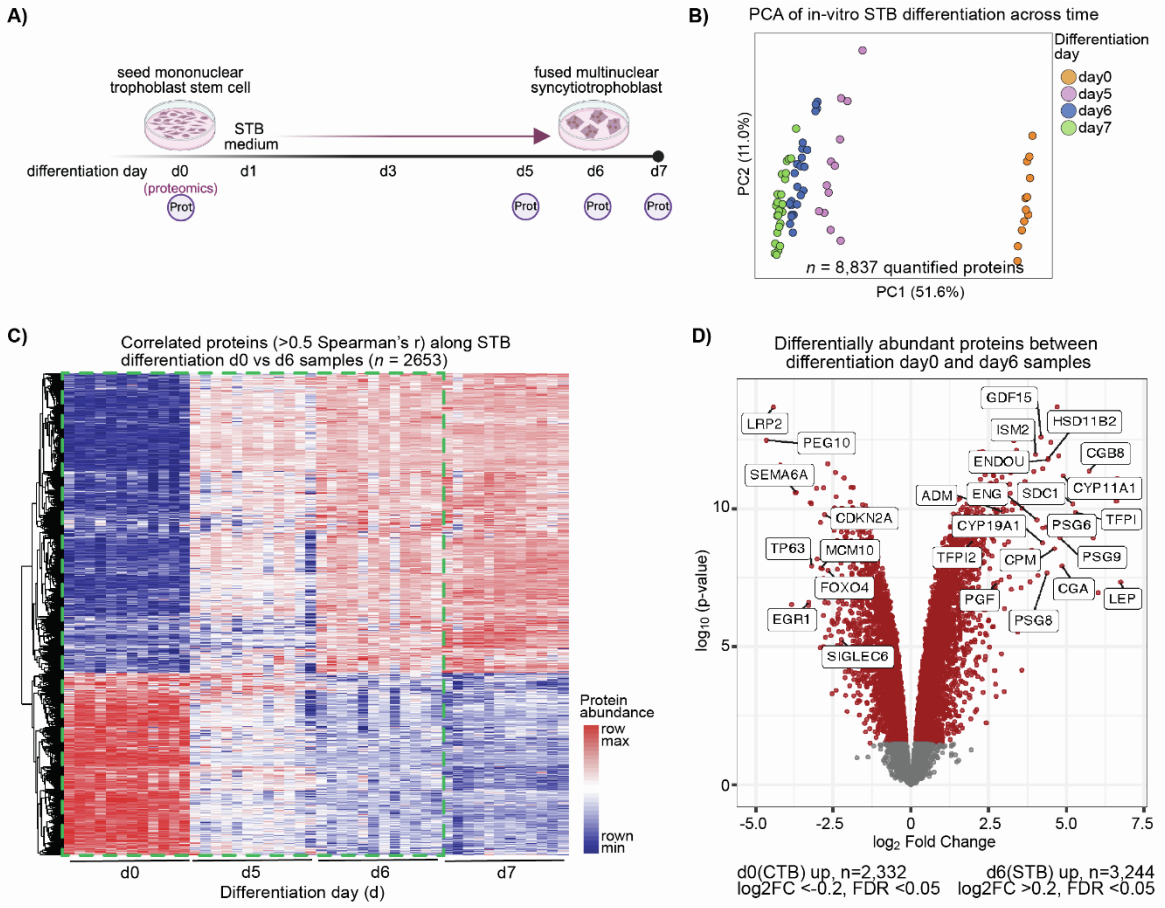

Supplementary Figure 4. Proteomics characterizes in-vitro primary human trophoblast progenitor and differentiated states.

(A) Schematic representation of published protocol for the six day (d) directed differentiation of TSCs towards the STB phenotype *in-vitro*[16]. High-sensitivity mass-spectrometry based proteomics was used to evaluate proteomic profiles of undifferentiated cells (d0), incompletely fused (d5) and fused (d6, d7). (*n* = 3 independent experiments with technical quadruplicates per timepoint). Schematic created with BioRender.com.

(B) Principal component graph of quantified relative protein abundances across all timepoints in the experiment (*n* = 8,837 proteins after quality control). There is clear separation of proteomic profiles across time with no considerable batch effects. (*n* = 3 independent experiments with technical quadruplicates per timepoint).

(C) Heatmap of Spearman correlated proteins above an absolute r value of 0.5 between day 0 (TSC) and day 6 (STB) of differentiation as marked by the dotted green line (*n* = 4,363 proteins). Protein abundances are scaled row-wise.

(D) Volcano plot of differentially abundant proteins between d0 and d6 of differentiation, illustrating the deep and successful phenotypic shift across time, where each dot represents a protein. Dots in red represent proteins under a 5% FDR threshold and an absolute log_2FC threshold > 0.2. Labelled proteins are canonical to each phenotype. Differential abundance was calculated on bulk abundances per cell type or state using a generalized linear model in the edgeR package.

TSC, trophoblast stem cell; STB, syncytiotrophoblast; CTB, cytotrophoblast.

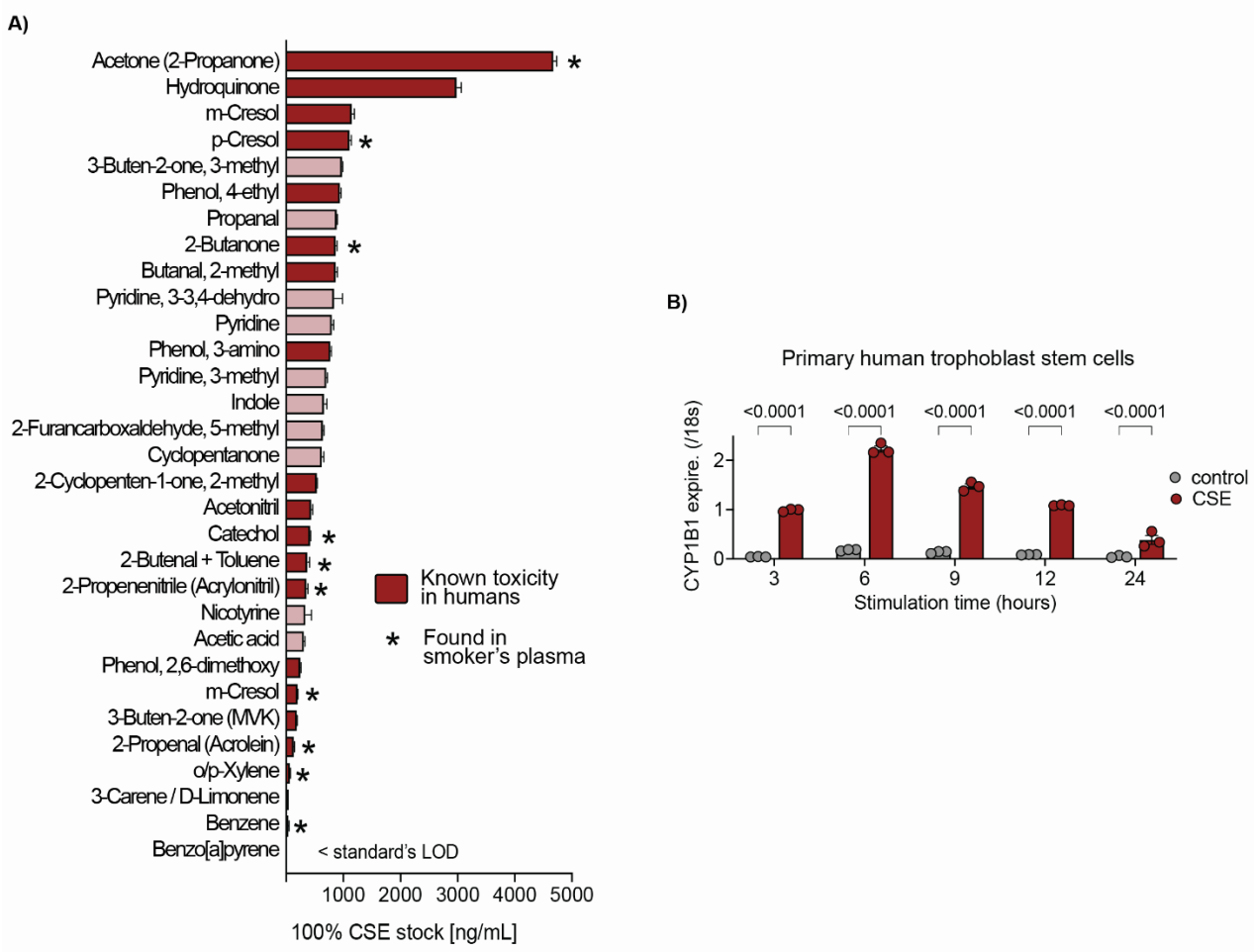

Supplementary Figure 5. Validation of cigarette smoke extract for in-vitro assessment of smoke component effects on cellular function.

(A) Bar plot of mean concentration of volatile and semi-volatile organic compounds present in a pooling of all 4x 100% cigarette smoke extract (CSE) batch stocks quantified by high-sensitivity gas-chromatography mass-spectrometry. Whiskers represent standard deviation. Red color indicates components known to have toxic cellular effects in humans, stars indicate components that have been measured in the saliva and circulation of adult smokers [179–182]. (*n* = 3 independent measurements in triplicate).

(B) Gene expression of markers associated with smoking by quantitative PCR on primary derived human trophoblast stem cells (bottom). (*n* = 3 independent experiments with pooled expression of 3 technical replicates per timepoint). Significance tested via 2-way ANOVA with Tukey's multiple comparisons.

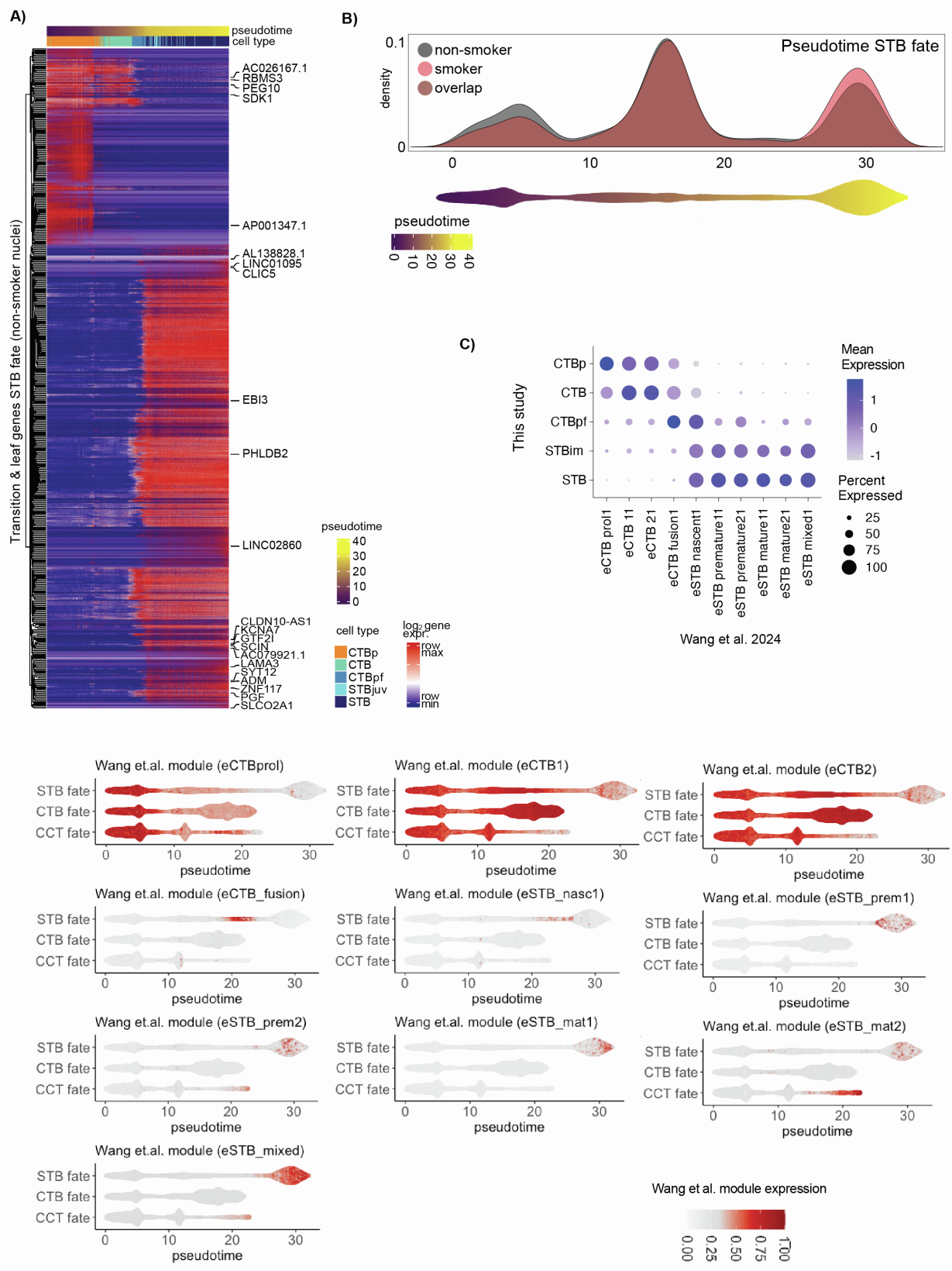

Supplementary Figure 6. Preferential differentiation towards the syncytiotrophoblast lineage by smoking.

(A) Heatmap of genes demarcating terminally differentiated cell states (leaf) and dynamic across pseudotime (transition) in non-smokers (n = 36,022 nuclei). Leaf genes were calculated as differential expression between nuclei corresponding to the first 20% and the last 20% values of pseudotime, with a concomitant absolute $\log_2$FC > 0.25 between timepoints. Pseudo-

bulk counts per cell type or state using a generalized linear model in the edgeR package that corrected for effects of sequencing batch and fetal sex were used. Transition genes were calculated based on scaled expression counts for genes with an absolute $log_2FC > 0.25$ between start and end of the trajectory and having an absolute Spearman correlation coefficient greater than 0.4.
(B) Density plot highlighting pseudotime distribution in smokers and non-smokers for the STB lineage. The progression colored by pseudotime modelled is shown as reference.
(C) Dotplot with mean expression of module scores calculated using the top 20 most differential genes per group for trophoblast subgroups as recently described by Wang et al.[33]
(D) Scatter plot of modelled pseudotime values separated by inferred lineage. Each dot represents a nucleus, colored by its scaled module score expression as described in (C).

CTB, cytotrophoblast; STB syncytiotrophoblast; CCT, cell column trophoblast; p, proliferating; pf, pre-fusion; im, immature.

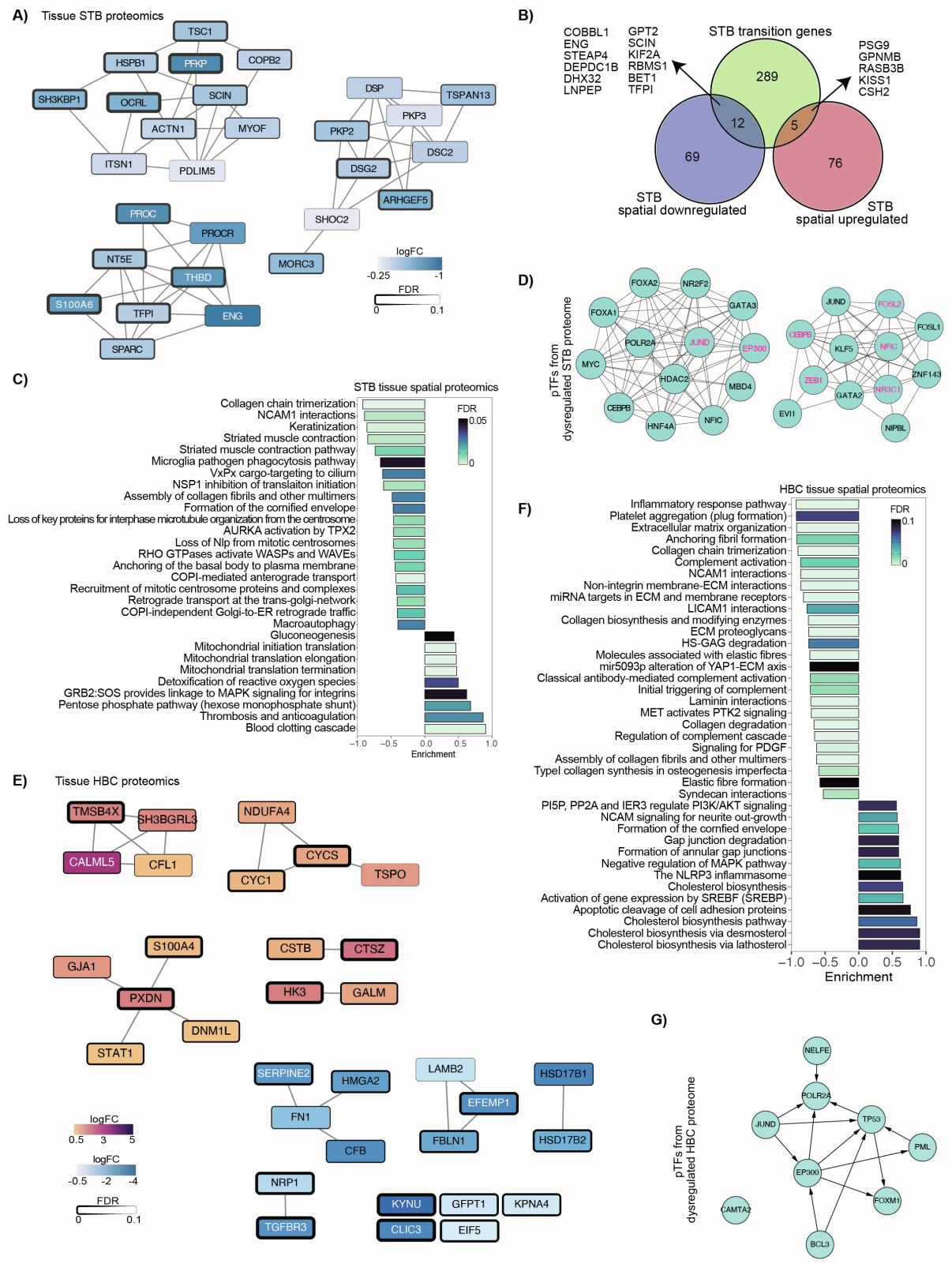

Supplementary Figure 7. Master regulators of placental macrophage and barrier dysregulation in maternal smoking at the proteo-transcriptomic level.
(A) Hub genes of upregulated (upper panel, $log_2FC > 0.25$, FDR < 0.1) tissue placental STB proteins with maternal smoking in early pregnancy, based on protein-protein interaction background stringDB network followed by topological analysis of ten different methods, clustered into communities based on Newman and Girvan's algorithm. Network analysis was

performed in the cytoscape software. Color represents log_2FC, node border thickness corresponds to differential abundance analysis' FDR.
(B) Venn diagram of STB tissue dysregulated proteins (logFC ± 0.25, FDR < 0.1) overlapping with transition genes from the trophoblast trajectory modelling (logFC ± 0.25, Spearman's r ± 0.4).
(C) Pathway enrichment analysis of dysregulated tissue STB proteins (absolute FC > 0.25, FDR < 0.1). Enrichment was done based on ranked log fold changes spanning the gene set enrichment analysis (GSEA), reactome and the WikiPathways databases. Positive enrichment values represent pathways enriched in smokers; negative values represent those enriched in non-smokers. Bar color is mapped to dysregulation FDR.
(D) Predicted tissue proteomics STB transcription factors (pTFs) calculated based on up- and down- regulated hub gene networks in (E) using the iRegulon cytoscape plugin. pTFs are visualized as a protein-protein interaction network (confidence level 0.15, no added proteins) using stringDB.
(E) Hub genes of upregulated (upper panel, $log_2FC > 0.25$, FDR < 0.1) and downregulated (lower panel, $log_2FC < -0.25$, FDR < 0.1) placental HBC tissue proteins with maternal smoking in early pregnancy, based on protein-protein interaction background stringDB network followed by topological analysis of ten different methods, clustered into communities based on Newman and Girvan's algorithm. Network analysis was performed in the cytoscape software. Color represents log_2FC, node border thickness corresponds to differential abundance analysis' FDR.
(F) Pathway enrichment analysis of dysregulated tissue HBC proteins (absolute FC > 0.25, FDR < 0.1). Enrichment was done based on ranked log fold changes spanning the gene set enrichment analysis (GSEA), reactome and the WikiPathways databases. Positive enrichment values represent pathways enriched in smokers; negative values represent those enriched in non-smokers. Bar color is mapped to dysregulation FDR.
(G) Predicted tissue proteomics HBC transcription factors (pTFs) calculated based on up- and down- regulated hub gene networks in (E) using the iRegulon cytoscape plugin. pTFs are visualized as a protein-protein interaction network (confidence level 0.15, no added proteins) using stringDB.

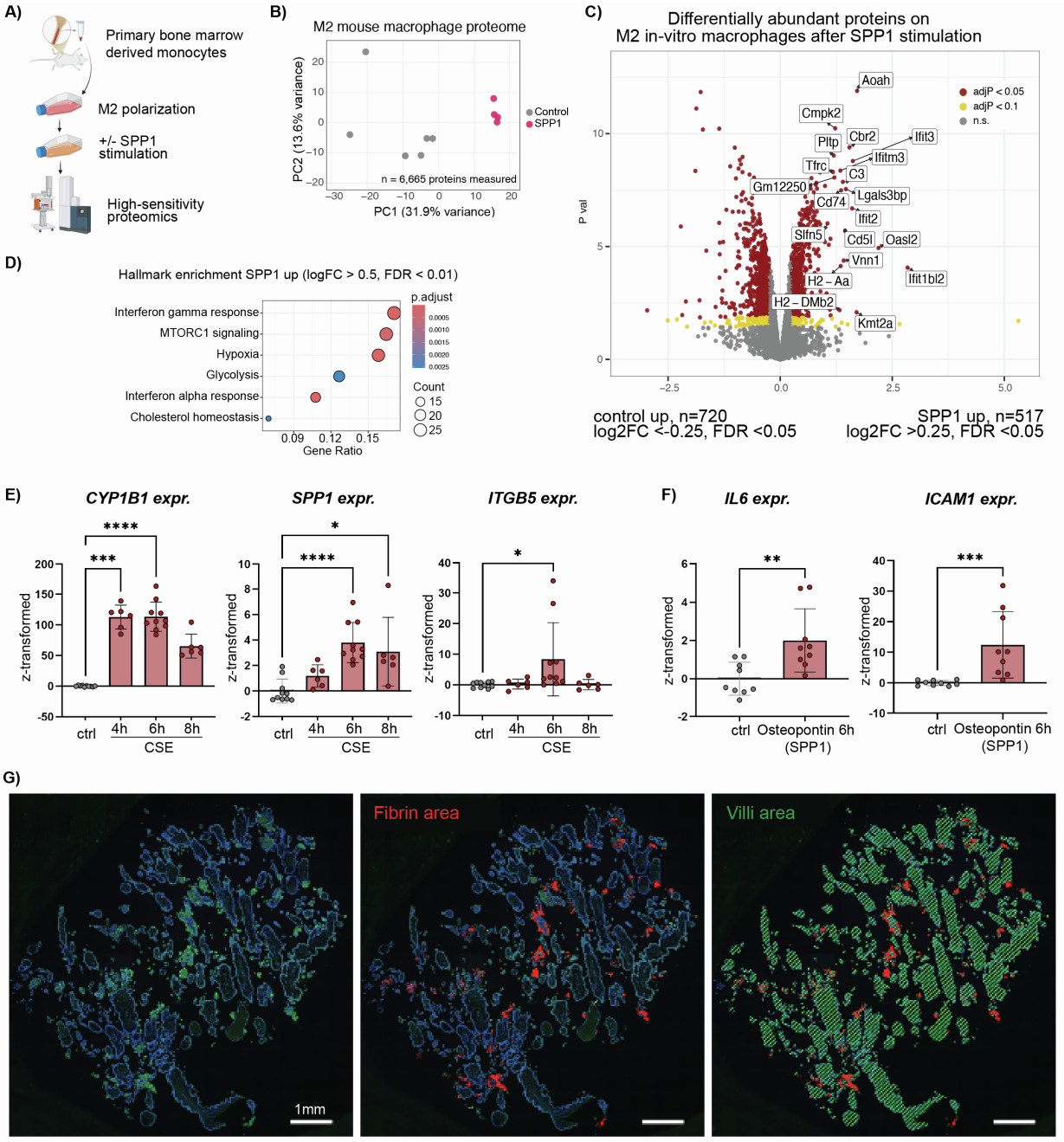

Supplementary Figure 8. In-vitro stimulation with SPP1 upregulates immune response markers in macrophages and trophoblast cells

A) Schematic experimental design. Mouse bone marrow derived monocytes were differentiated to M0 macrophages (BMDM) and polarized towards the M2-phenotype by IL-4 (10 ng/mL) and IL-13 (10 ng/ml) for 24h. Macrophages were stimulated with osteopontin (1ng/ul) for 24hours before being analysed at the proteomic level by mass-spectrometry based proteomics. Created with Biorender.com.
B) Principal component analysis of the proteome of M2-phenotype mouse bone marrow derived macrophages (n = 665 proteins measured).
C) Volcano plot of differentially abundant proteins in M2-phenotype mouse bone marrow derived macrophages following in-vitro SPP1 stimulation. The top 20 most dysregulated proteins are shown. Differentially abundant proteins were calculated by linear regression and Benjamini-Hochberg correction in the limma package.
D) Summary of pathway enrichment analysis of in-vitro upregulated proteins by SPP1 stimulation of mouse macrophages (absolute log2FC > 0.5, FDR < 0.05). Enrichment was

done based on ranked log2fold changes spanning the gene set enrichment analysis (GSEA) and Hallmark databases.
E, F) Gene expression of selected markers as measured via quantitative PCR of primary derived cytotrophoblast (CTB) cells following exposure to cigarette smoking extract (CSE [1:200 of 100%], E) and osteopontin (SPP1 [2.5ug/ul], F) in-vitro for variable timepoints as indicated. Differences calculated by ...
G) Placental perivillous fibrin deposition and platelet adhesion software-based analysis. Images of double-stained placenta tissue (Fibrin, CD42b) were obtained using an Evident Olympus VS200 Slide Scanner and images were afterwards subjected to Visiopharm (Version 2021.09) for a software-based quantification of fibrin. Villous regions were detected within each sample by applying a threshold on a feature combining a polynomial gradient filter of FITC (Fibrin) and a mean filter feature of the DAPI channel. Fibrin within the villous regions was detected by a threshold within the FITC channel. Adherent platelets were detected by measuring CD42b positive signals using the Cy3 channel. Fibrin area (μm^2) and platelet area (μm^2) was normalized to total villi area (μm^2). Scale bars represent 1mm.

Supplementary Tables

Supplementary Table 1. Participant characteristics. Demographic and clinical characteristics of the snRNA-seq/DVP omics cohort and the independent validation cohort (used for qPCR and PlGF ELISA), stratified by smoking status.

Supplementary Table 2. snRNA-seq differentially expressed genes for all cell types. Differential expression results (log2FC, FDR) between smokers and non-smokers for every annotated placental cell type/state in the single-nucleus RNA-seq data, computed from pseudobulk profiles with edgeR.

Supplementary Table 3. Trajectory leaf genes. Genes marking the terminal, differentiated end-points (leaves) of the three modelled trophoblast lineages (STB-, CTB-, and CCT-fate), calculated by pseudobulk edgeR DEG testing within each lineage using non-smoker nuclei only, capturing genes that define each terminal cell identity (FDR<0.05).

Supplementary Table 4. Trajectory transition genes. Genes whose expression correlates with pseudotime along each trophoblast differentiation trajectory (Spearman's $|r| \geq 0.4$, non-smoker nuclei), representing putative regulators of the progressive shift between progenitor and differentiated states.

Supplementary Table 5. DVP dysregulated proteins. Differential abundant protein results (log2FC, FDR) identified by deep visual proteomics in laser-microdissected STB, CTB, and HBC regions of interest, comparing smokers to non-smokers.

Supplementary Table 6. In-vitro proteomic comparison. Proteomic comparison of in-vitro differentiated primary trophoblast (STB) pellets harvested at differentiation day 7, contrasting 48-hour cigarette smoke extract (CSE) exposure versus untreated controls.

Supplementary Table 7. Cell-type resolved receptor-ligand interaction. Results inferred with CellChat, calculated separately per omics modality (snRNA-seq and DVP) and per smoking condition, then compared across the STB-CTB, CTB-HBC, and within-cell-type (autocrine) interaction sets, reporting communication probability and significance for each ligand-receptor pair.